

Field Line Resonance in Two and a Half Dimensions

DRAFT VERSION CREATED ON APRIL 10, 2016

1

© Charles A. McEachern 2016

2



3

The text of this work is licensed under a Creative Commons

Attribution-ShareAlike 4.0 International license.

4

⁵ Acknowledgements

⁶ Acknowledgement placeholder.

⁷ Dedication

⁸ Dedication placeholder.

Abstract

¹⁰ Abstract placeholder.

Contents

¹¹	Acknowledgements	i
¹³	Dedication	ii
¹⁴	Abstract	iii
¹⁵	List of Tables	vii
¹⁶	List of Figures	viii
¹⁷	1 Introduction	1
¹⁸	1.1 Structure of the Present Work	2
¹⁹	2 The Near-Earth Environment	4
²⁰	2.1 The Outer Magnetosphere	5
²¹	2.2 The Inner Magnetosphere	6
²²	2.3 The Ionosphere	8
²³	2.4 Geomagnetic Storms and Substorms	9
²⁴	3 Field Line Resonance	12
²⁵	3.1 Harmonic Structure	16
²⁶	3.2 Azimuthal Modenumber	18
²⁷	3.3 Poloidal and Toroidal Polarizations	20
²⁸	3.4 Giant Pulsations	22
²⁹	3.5 Motivations for the Present Work	23

30	4 Waves in Cold Resistive Plasma	25
31	4.1 Guided Propagation	27
32	4.2 Compressional Propagation	28
33	4.3 High Altitude Limit	30
34	4.4 Implications to the Present Work	31
35	5 “Tuna Half” Dimensional Model	33
36	5.1 Coordinate System	34
37	5.2 Physical Parameter Profiles	38
38	5.3 Driving	41
39	5.4 Maxwell’s Equations	44
40	5.5 Boundary Conditions	48
41	6 Electron Inertial Effects	53
42	6.1 The Boris Factor	54
43	6.2 Parallel Currents and Electric Fields	56
44	6.3 Inertial Length Scales	62
45	6.4 Discussion	63
46	7 Numerical Results	65
47	7.1 Modenumber and Compression	65
48	7.2 Resonance and Rotation on the Dayside	71
49	7.3 Resonance and Rotation on the Nightside	78
50	7.4 Ground Signatures and Giant Pulsations	82
51	7.5 Discussion	86
52	8 Van Allen Probe Observations	88
53	8.1 Sampling Bias and Event Selection	89
54	8.2 Events by Mode	92
55	8.3 Events by Amplitude	96
56	8.4 Events by Frequency	101
57	8.5 Events by Phase	105
58	8.6 Discussion	110

59	9 Conclusion	111
60	9.1 Summary of Results	111
61	9.2 Future Work	111
62	References	113

⁶³ List of Tables

⁶⁴	3.1 IAGA Magnetic Pulsation Frequency Bands	14
⁶⁵	5.1 Typical Parameters for the Tuna Density Profile	39
⁶⁶	5.2 Integrated Atmospheric Conductivity	49

⁶⁷ **List of Figures**

68	2.1 Outer Magnetosphere Cutaway	5
69	2.2 Inner Magnetosphere Cutaway	7
70	3.1 Alfvén Bounce Frequencies	15
71	3.2 First and Second Harmonic Resonances	17
72	3.3 Large and Small Azimuthal Modenumbers	19
73	3.4 Poloidal Mode Structure	21
74	3.5 Toroidal Mode Structure	22
75	4.1 Compressional Alfvén Wave Cutoff Frequencies	32
76	5.1 Nonorthogonal Dipole Grid	38
77	5.2 Alfvén Speed Profiles	40
78	5.3 Ionospheric Conductivity Profiles	41
79	5.4 Decreasing Penetration with Increasing Modenumber	43
80	5.5 Sym-H for June 2013 Storm	44
81	6.1 Plasma Frequency Profile	55
82	6.2 Electric Field Snapshots	57
83	6.3 Current and Poynting Flux at 100 km	58
84	6.4 Current and Poynting Flux at 1000 km	60
85	6.5 Power Density at the Ionosphere	61
86	6.6 Parallel Electric Fields by Perpendicular Grid Resolution	63
87	7.1 Magnetic Field Snapshots from a Small- m Run	68
88	7.2 Magnetic Field Snapshots from a Large- m Run	69
89	7.3 Compressional Coupling to the Poloidal Mode	70
90	7.4 Dayside Poloidal and Toroidal Energy	75

91	7.5 Dayside Poloidal Energy Distribution	76
92	7.6 Dayside Toroidal Energy Distribution	77
93	7.7 Nightside Poloidal and Toroidal Energy	79
94	7.8 Nightside Poloidal Energy Distribution	80
95	7.9 Nightside Toroidal Energy Distribution	81
96	7.10 Dayside Ground Magnetic Fields	84
97	7.11 Nightside Ground Magnetic Fields	85
98	8.1 Distribution of Usable Van Allen Probe Data	90
99	8.2 Observation Rate of Pc4 Events	93
100	8.3 Observation Rate of Pc4 Events by Mode	94
101	8.4 Amplitude Distribution of Pc4 Events by Mode	97
102	8.5 Waveforms and Spectra for a Strong Pc4 Event	99
103	8.6 Observation Rate of Pc4 Events by Mode and Amplitude	100
104	8.7 Observation Rate of Pc4 Events by Mode and Frequency	103
105	8.8 Frequency Distribution of Pc4 Events by Mode	104
106	8.9 Waveforms and Spectra for a Pc4 Event	107
107	8.10 Phase Distribution of Pc4 Events by Mode	108
108	8.11 Observation Rate of Pc4 Events by Mode and Phase	109

¹⁰⁹ **Chapter 1**

¹¹⁰ **Introduction**

¹¹¹ 1859 was a pivotal year in human history. The United States moved steadily toward
¹¹² the American Civil War, which would abolish slavery and consolidate the power of
¹¹³ the federal government. A slew of conflicts in Southern Europe, such as the Austro-
¹¹⁴ Sardinian War, set the stage for the unification of Italy. The Taiping Civil War — one
¹¹⁵ of the bloodiest conflicts of all time — is considered by many to mark the beginning
¹¹⁶ of modern Chinese history. *Origin of Species* was published. The first transatlantic
¹¹⁷ telegraph cable was laid.

¹¹⁸ Meanwhile, ambivalent to humanity, the Sun belched an intense burst of charged parti-
¹¹⁹ cles and magnetic energy directly at Earth. The resulting geomagnetic storm¹ caused
¹²⁰ telegraph systems to fail across the Western hemisphere, electrocuting operators and
¹²¹ starting fires[35, 96]. Displays of the northern lights were visible as far south as Cuba.

¹²² The Solar Storm of 1859 was perhaps the most powerful in recorded history, but by no
¹²³ means was it a one-time event. The Sun discharges hundreds of coronal mass ejections
¹²⁴ (CMEs) per year, of all sizes, in all directions. In fact, a comparably large CME narrowly
¹²⁵ missed Earth in 2012[72]. Had it not, it's estimated it would have caused widespread,
¹²⁶ long-term electrical outages, with a damage toll on the order of 10^{12} dollars[66].

¹The Solar Storm of 1859 is also called the Carrington Event, after English astronomer Richard Carrington. He drew a connection between the storm's geomagnetic activity and the sunspots he had observed the day before.

127 The Sun’s extreme — and temperamental — effect on Earth’s magnetic environment
128 makes a compelling case for the ongoing study of space weather. Such research has
129 evolved over the past century from sunspot counts and compass readings to multi-
130 satellite missions and supercomputer simulations. Modern methods have dramatically
131 increased humanity’s understanding of the relationship between the Sun and the Earth;
132 however, significant uncertainty continues to surround geomagnetic storms, substorms,
133 and the various energy transport mechanisms that make them up.

134 The present work focuses in particular on the phenomenon of field line resonance: Alfvén
135 waves bouncing between the northern and southern hemispheres. Such waves play an
136 important part in the energization of magnetospheric particles, the transport of energy
137 from high to low altitude, and the driving of currents at the top of the atmosphere.

138 **TODO:** More is needed before we can jump into a description of the present work.
139 Introduce what we’re working on a bit ore specifically. Talk about how space is a
140 laboratory that teaches us about plasma in a way that’s relevant to both astrophysics
141 and fusion reactors, which are hard to measure. Fishbone instability.

142 1.1 Structure of the Present Work

143 Chapter 2 surveys the near-Earth environment. Prominent features of the magneto-
144 sphere are defined. The response of the magnetosphere to transient solar wind events
145 is summarized.

146 Chapter 3 introduces the field line resonance phenomenon, in terms of both the under-
147 lying physics and notable work on the topic. Jargon is introduced to clarify important
148 elements of wave structure. Several open questions about field line resonances (FLRs)
149 are offered as motivations for the present work.

150 Chapter 4 lays the groundwork for a numerical model by exploring the fundamental
151 equations of waves in a cold, resistive plasma — such as Earth’s magnetosphere. Char-
152 acteristic scales are gleaned from the resulting dispersion relations.

153 Chapter 5 presents Tuna, a new two and a half dimensional simulation designed specifically
154 for the realistic modeling of FLRs. Tuna’s non-orthogonal geometry, height-resolved ionosphere,
155 novel driving mechanism, and coupling to the atmosphere are explained.
156

157 Chapter 6 considers the addition of electron inertial effects to Tuna, touches on what
158 can be learned from them, and shows that they incur an unreasonable computational
159 cost. (Electron inertia is neglected in the results presented in other chapters.) **TODO:**
160 **Previous work has looked at inertial effects for localized models. The exciting part is**
161 **that we’re looking at a global model.**

162 Chapter 7 describes the core numerical results of the work, unifying several of the
163 questions posed in Chapter 3. Significant depth is added to past work on finite poloidal
164 lifetimes[64, 78]. Interplay between poloidal-toroidal coupling, shear-compressional coupling,
165 and Joule dissipation is considered from several angles.

166 Chapter 8 puts the numerical results in physical context through the analysis of data
167 from the Van Allen Probes mission. FLR occurrence rates are considered in terms of
168 location, mode structure, and polarization – parameters which have been only partially
169 addressed by other recent FLR surveys[18, 70].

170 Chapter 9 briefly summarizes the results shown in the above chapters — the code
171 development, analysis of numerical results, and satellite observation — and suggests
172 further directions.

¹⁷³ **Chapter 2**

¹⁷⁴ **The Near-Earth Environment**

¹⁷⁵ From Earth’s surface to a height of a hundred kilometers or so, the atmosphere is a
¹⁷⁶ well-behaved fluid: a collisional ensemble of neutral atoms. Higher up, its behavior
¹⁷⁷ changes dramatically. As altitude increases, solar ultraviolet radiation becomes more
¹⁷⁸ intense, which ionizes atmospheric atoms and molecules. Density also decreases, slow-
¹⁷⁹ ing collisional recombination. Whereas the neutral atmosphere is held against Earth’s
¹⁸⁰ surface by gravity, the motion of charged particles is dominated by Earth’s geomagnetic
¹⁸¹ field, as well as the electromagnetic disturbances created as that field is hammered by
¹⁸² the solar wind.

¹⁸³ Before discussing specific interactions, it’s appropriate to introduce the so-called “frozen-
¹⁸⁴ in condition.” In a collisionless plasma, magnetic field lines are equipotential contours.
¹⁸⁵ Charged particles move freely along the contours, but cannot move across them. Com-
¹⁸⁶ pression of the magnetic field is synonymous with compression of the ambient plasma,
¹⁸⁷ and any magnetic field lines that thread a moving plasma are dragged along with it.
¹⁸⁸ This assumption is valid throughout most of the magnetosphere — that is, the region of
¹⁸⁹ space primarily governed by Earth’s magnetic field — and provides an invaluable tool
¹⁹⁰ for understanding the large-scale motions of plasmas and fields.

₁₉₁ **2.1 The Outer Magnetosphere**

₁₉₂ Plasma behavior within Earth's magnetosphere is ultimately driven by the solar wind:
₁₉₃ a hot (~ 100 eV), fast-moving (~ 100 km/s) plasma threaded by the interplanetary mag-
₁₉₄ netic field (~ 10 nT)¹. The density of the solar wind is on the order of 10^6 /cm³; in a
₁₉₅ laboratory setting, this would constitute an ultra-high vacuum (atmospheric density at
₁₉₆ sea level is $\sim 10^{19}$ /cm³), but compared to much of the magnetopause it's quite dense.



Figure 2.1: TODO: The outer magnetosphere...

₁₉₇ The magnetosphere's outer boundary represents a balance between the solar wind dy-
₁₉₈ namic pressure and the magnetic pressure of Earth's dipole field. On the dayside, the
₁₉₉ dipole is compressed, pushing this boundary to within about $10 R_E$ of Earth². The
₂₀₀ nightside magnetosphere is stretched into a long tail which may exceed $50 R_E$ in width
₂₀₁ and $100 R_E$ in length.

¹Listed values correspond to the solar wind at Earth's orbit.

²Distances in the magnetosphere are typically measured in units of Earth radii: $1 R_E \equiv 6378$ km.

202 When the interplanetary magnetic field opposes the geomagnetic field at the nose of
203 the magnetosphere, magnetic reconnection occurs. Closed magnetospheric field lines
204 “break,” opening up to the interplanetary magnetic field³. They then move tailward
205 across the poles, dragging their frozen-in plasma with them. Reconnection in the tail
206 allows magnetic field lines to convect back to the day side, across the flanks. This
207 process is called the Dungey cycle[23].

208 Viewed from the north, the Dungey cycle involves a clockwise flow of flux and plasma on
209 the dusk side and a counterclockwise flow on the dawn side. The motion is accompanied
210 by a convection electric field, per Ohm’s law⁴.

211 **TODO: Jets from magnetic reconnection... release of magnetic tension!**

212 Consistent with Ampère’s law, the interplanetary magnetic field is separated from the
213 magnetosphere by a current sheet: the magnetopause. On the dayside, the magne-
214 topause current flows duskward; on the nightside, it flows downward around the mag-
215 netail.

216 Earth’s dipole is significantly deformed in the magnetotail; field lines in the northern
217 lobe of the tail points more or less Earthward, and vice versa. Plasma within the lobes
218 is cool ($\sim 100 \text{ eV}$) and rarefied ($\sim 10^{-2} / \text{cm}^3$). The two lobes are divided by the plasma
219 sheet, which is comparably hot ($\sim 10^3 \text{ eV}$) and dense ($\sim 1 / \text{cm}^3$). The plasma sheet
220 carries a duskward current which connects to the magnetopause current.

221 **2.2 The Inner Magnetosphere**

222 Within about $L \sim 8$ (where L is the McIlwain parameter⁵), the dipole magnetic field
223 is not appreciably deformed by the solar wind. As a result, the structures in the inner

³Closed field lines

Closed field lines are more or less dipolar; one end connects to the north pole of Earth’s magnetic core, and the other end to the south pole. Open field lines are tethered to Earth at one end. In principle, the other end eventually doubles back to Earth, but in practice the field line is lost to the solar wind. The distinction is important because charged particle motion is guided by magnetic field lines, as discussed in Chapter 3.

⁴In the case of an ideal plasma, Ohm’s law takes the form $\underline{E} + \underline{U} \times \underline{B} = 0$.

⁵The McIlwain parameter L is used to index field lines in Earth’s dipole geometry: $L \equiv \frac{r}{\sin^2 \theta}$ for colatitude θ and radius r in Earth radii. For example, the $L = 5$ field line passes through the equatorial

224 magnetosphere follow closely from the motion of charged particles in an ideal dipole
225 field.



Figure 2.2: TODO: The inner magnetosphere...

226 The plasmasphere — a cold (~ 1 eV), dense ($10^2 / \text{cm}^3$ to $10^4 / \text{cm}^3$) torus of corotating
227 plasma — is formed by the outward drift of atmospheric ions along magnetic closed
228 field lines. Its outer boundary is thought to represent a balance between the corotation
229 electric field (per the rotation of Earth's magnetic dipole) and the convection electric
230 field (associated with the convection of magnetic flux during the Dungey cycle). Particle
231 density drops sharply at the edge of the plasmasphere; the boundary is called the
232 plasmapause. The plasmapause typically falls around $L = 4$, though during prolonged
233 quiet times it can extend to $L = 6$ or larger.

plane at a geocentric radius of $5 R_E$, then meets the Earth at a colatitude of $\arcsin \sqrt{\frac{1}{5}} \sim 27^\circ$ (equally, a latitude of $\arccos \sqrt{\frac{1}{5}} \sim 63^\circ$).

234 Energetic particles trapped within the inner magnetosphere are divided into two popu-
235 lations.

236 The Van Allen radiation belts are made up of particles with energy above 10^5 eV or
237 so. The inner belt ($L \lesssim 2$) is primarily composed of protons, the decay remnants of
238 neutrons freed from the atmosphere by cosmic rays. The outer belt ($L \gtrsim 4$) is primarily
239 composed of high-energy electrons. The density of radiation belt particles is significantly
240 affected by geomagnetic storms and substorms; a typical value is $10 / \text{cm}^3$.

241 Particles with energies of 10^3 eV to 10^5 eV make up the ring current, which extends
242 from $L \sim 3$ to $L \sim 5$. Gradient-curvature drift carries ions and electrons in opposite
243 directions; the net result is a westward current. During quiet times, the ring current
244 causes magnetic a southward magnetic field on the order of 1 nT at Earth's equator,
245 while during geomagnetically active times (discussed in Section 2.4) the effect may
246 100 nT or more⁶.

247 2.3 The Ionosphere

248 Earth's neutral atmosphere is an excellent insulator. Collisions are so frequent that
249 charged particles quickly thermalize and recombine. The breakdown of air molecules
250 into a conductive plasma (as happens during a lightning strike, for example) requires
251 electric fields on the order of 10^9 mV/m.

252 Cold particles in the magnetosphere are likewise not conducive to currents. In the
253 absence of collisions, electrons and ions drift alongside one another in response to an
254 electric field, creating no net current perpendicular to the magnetic field⁷.

255 The ionosphere is a sweet spot between the two regimes. Collisions are frequent enough
256 to disrupt the drift of ions, but not frequent enough to immobilize the electrons. The
257 result is nonzero Pedersen and Hall conductivity, corresponding to current along the
258 electric field and in the $\underline{B} \times \underline{E}$ direction respectively. It is these currents — particularly

⁶For comparison, Earth's dipole field points north at the equator with a magnitude over 10^4 nT.

⁷The so-called E -cross- B drift is associated with a velocity of $\underline{U} = \frac{1}{B^2} \underline{E} \times \underline{B}$, independent of a charged particle's mass or sign.

259 the Hall current — which give rise to magnetic fields at the ground. Collisions in the
260 ionosphere also give rise to a finite parallel conductivity, allowing for the formation of
261 potential structures along the magnetic field line.

262 The convection electric field (associated with the Dungey cycle, Section 2.1) drives
263 Pedersen currents in the ionosphere. Pedersen currents flow downward on the flanks
264 and duskward across the poles. The currents remain divergence-free by connecting
265 to field-aligned currents at the edges of the polar cap. The field-aligned currents, in
266 turn, connect to the magnetopause current, the cross-tail current, and the (partial) ring
267 current.

268 When electron density is low, thermal velocities may be unable to carry enough current
269 to satisfy $\nabla \cdot \underline{J} = 0$. This leads to the formation of potential structures along geomagnetic
270 field lines in the ionosphere. Such structures accelerate particles along magnetic field
271 lines, leading to the precipitation of energetic particles into the atmosphere. As the
272 particles thermalize, they excite atmospheric atoms. The resulting spontaneous emission
273 is often in the visible spectrum, giving rise to the aurora.

274 2.4 Geomagnetic Storms and Substorms

275 The quiet geomagnetic behavior described above is periodically disturbed by transient
276 solar phenomena such as corotating interaction regions (CIRs) and coronal mass ejec-
277 tions (CMEs). CMEs, as noted in Chapter 1, are bursts of unusually dense solar wind
278 which are ejected from regions of high magnetic activity on the Sun; they are most
279 common at the height of the eleven-year solar cycle. CIRs, on the other hand, occur
280 when a relatively fast region of the solar wind catches up to an earlier and slower-moving
281 pocket of solar wind, resulting in a pair of shockwaves.

282 During a storm, increased solar wind intensity results in enhanced magnetic reconnection
283 on the dayside. As the newly-opened field lines are swept tailward, the convection
284 electric field is strengthened. The plasmasphere — the outer boundary of which is
285 set by a balance between the convection electric field and the (more or less constant)

286 corotation electric field — sheds its outer layers. A large number of energetic particles
287 are also injected into the ring current[68].

288 The strength of the storm is gauged by the size of the magnetic perturbation created
289 by the ring current⁸. A small storm has a magnitude of 50 nT to 100 nT. Large storms
290 may reach 250 nT to 500 nT. The Carrington Event, mentioned in Chapter 1, is thought
291 to have exceeded 1700 nT[96].

292 The main phase of a storm typically lasts for several hours. Storm recovery — the
293 gradual return of the storm index to zero, and the refilling of the plasmasphere —
294 typically lasts several days. Geomagnetic storms occur tens of times per year at the
295 height of the solar cycle, and just a few times per year otherwise.

296 Whereas storms are prompted by large solar wind events on the dayside, geomagnetic
297 substorms are primarily a nightside occurrence. As flux accumulates in the tail, mag-
298 netic tension builds in the stretched field lines. A substorm is an impulsive release of
299 that tension.

300 **TODO: Phases of a substorm. Definition of a substorm comes from [1]. Revised by [69].**

301

302 At substorm onset, a burst of reconnection occurs in the tail. A jet of plasma is launched
303 Earthward from the reconnection site (and another is launched tailward, and lost to the
304 solar wind). The Earthward plasma injection injects particles into the ring current.
305 The outer radiation belt is depleted, then repopulated. Energetic particles precipitate
306 into the atmosphere, giving rise to a distinctive sequence of auroral signatures over the
307 course of about an hour.

308 Concurrent with substorm onset, impulsive Alfvén waves are observed with periods of
309 a minute or two. The precise ordering of events — whether reconnection causes the
310 waves, or vice versa, or if they share a common cause — remains controversial.

311 Each substorm lasts several hours, including the time it takes for the ring current to
312 return to pre-substorm levels. Several substorms may occur per day during quiet times.

⁸The most commonly used storm index is DST, which is computed hourly using measurements from several ground magnetometers near the equator. The Sym-H index, used in Section 5.3, is computed once per minute.

³¹³ During a storm, substorms become far more frequent; by the time one has ended,
³¹⁴ another may have already begun.

³¹⁵ **Chapter 3**

³¹⁶ **Field Line Resonance**

- ³¹⁷ The motion of a charged particle in a dipole field can be described in terms of three
³¹⁸ fundamental motions. The first is cyclotron motion. Given a uniform magnetic field
³¹⁹ line, a particle follows a helical path. It moves in a circular path in a plane normal to
³²⁰ the magnetic field line, and keeps a constant velocity along the direction of the field.
- ³²¹ The second fundamental motion is bounce motion. As it moves along the magnetic field
³²² line like a bead on a wire, the particle experiences a change in magnetic field magnitude.
³²³ In order to conserve its magnetic moment (also called the first adiabatic invariant), the
³²⁴ particle's perpendicular kinetic energy increases in proportion with the magnetic field.
³²⁵ When the perpendicular kinetic energy can no longer increase — that is, when all of the
³²⁶ particle's kinetic energy is perpendicular — the particle bounces back. (If the particle's
³²⁷ parallel kinetic energy is sufficiently large, it doesn't bounce, and instead precipitates
³²⁸ into the atmosphere.) Particles undergoing bounce motion continuously move back and
³²⁹ forth between the northern and southern hemispheres.
- ³³⁰ The third fundamental motion is drift motion. Over the course of a particle's cyclotron
³³¹ motion, the Earthward half of the orbit experiences a slightly stronger magnetic field
³³² (and thus a slightly smaller orbit radius). The net effect, called the gradient-curvature
³³³ drift, is an azimuthal motion around Earth.

334 Characteristic timescales for each of the above motions depend on particle energy. Elec-
335 tron cyclotron motion is on the order of **TODO: ...** in the ionosphere, and closer to
336 **TODO: ...** in the tail; ions gyrate slower by three orders of magnitude due to their
337 larger mass. **TODO: Bounce... Drift...**

338 Wave-particle resonance arises when a particle's periodic motion matches with the fre-
339 quency of a coincident electromagnetic wave[25, 63, 74, 85]. In the particle's rest frame,
340 the wave then appears as a net electric field. This allows a net movement of energy
341 between the wave and the particle. The interaction is analogous to a surfer moving
342 along with — and being accelerated by — a wave in the ocean. Such resonance can
343 arise for any of the three fundamental motions, or even for a combination of them.

344 In the present work, the waves in question are field line resonances (FLRs). An FLR
345 is a standing harmonic on a geomagnetic field line. It can also be envisioned as a
346 superposition of traveling waves, reflecting back and forth between its northern and
347 southern foot points at the conducting ionosphere.

These waves travel at the Alfvén speed, v_A , defined per

$$v_A^2 \equiv \frac{B^2}{\mu_0 \rho} \quad \text{or, equally,} \quad v_A^2 \equiv \frac{1}{\mu_0 \epsilon_{\perp}} \quad (3.1)$$

348 Where B is the magnetic field magnitude, ρ is the mass density, and μ_0 is the magnetic
349 constant. The perpendicular electric constant ϵ_{\perp} is analogous to the electric constant
350 ϵ_0 , and arises in cases (such as the magnetosphere) where a dielectric medium exhibits
351 a preferred direction. In the magnetosphere, mass density and magnetic field strength
352 depend strongly on position. As a result, the Alfvén speed may vary by several orders
353 of magnitude over the length of a field line.

354 The fundamental equations of field line resonance were presented by Dungey in 1954[22];
355 since then, they have remained a topic of active study.

356 **TODO: ...in no small part because they are not just relevant to space!** Alfvén waves
357 also show up in laboratory plasmas, which are hard to measure directly, and in all sorts
358 of astrophysical contexts.

359 So-called ultra low frequency waves — of which FLRs are a subset — are categorized
 360 by morphology. Continuous (long-lived) pulsations are termed Pc, while irregular pul-
 361 sations are called Pi. Within each are a number of frequency bands; see Table 3.1[45].

Table 3.1: IAGA Magnetic Pulsation Frequency Bands

	Pc1	Pc2	Pc3	Pc4	Pc5	Pi1	Pi2
Period (s)	0.2–5	5–10	10–45	45–150	150–600	1–40	40–150
Frequency (mHz)	200–5000	100–200	22–100	7–22	2–7	25–1000	7–25

362 TODO: Boundaries between wave bands are, in practice, not strict. They are sometimes
 363 fudged to better match phenomenological boundaries.

364 FLRs fall into the Pc3, Pc4, and Pc5 ranges. The present work focuses specifically
 365 on the Pc4 band: waves with periods of a minute or two. Frequencies in the Pc4
 366 range typically coincide with Alfvén bounce times¹ near the plasmapause: $L \sim 4$ to
 367 $L \sim 6$ [3, 18, 26, 56]². In fact, the large radial gradients in the Alfvén speed near the
 368 plasmapause act as an effective potential well, trapping FLRs[17, 50, 53, 54, 62, 88].

369 In addition to being radially localized, FLRs in the Pc4 frequency band (also called Pc4
 370 pulsations, or just Pc4s) are localized in magnetic local time (MLT³). They have also
 371 been shown to occur preferentially on the dayside, during storms or storm recovery[3,
 372 18, 26, 52, 56, 97].

373 In the inner magnetosphere, the Alfvén frequency — and thus the frequency of FLRs
 374 — often coincides with integer or half-integer⁴ multiples of particle drift frequencies[19].
 375 The resulting wave-particle interactions can give rise to significant energization and
 376 radial diffusion of the particles. In some cases, the waves also include an electric field

¹The Alfvén frequency is the inverse of the Alfvén bounce time: $\frac{2\pi}{\omega_A} \equiv \oint \frac{dz}{v_A}$.

²Not coincidentally, these are the same L -shells where the Van Allen Probes spend most of their time; see Chapter 8.

³Noon points toward the Sun and midnight away from it, with 06:00 and 18:00 at the respective dawn and dusk flanks.

⁴See Section 3.1.

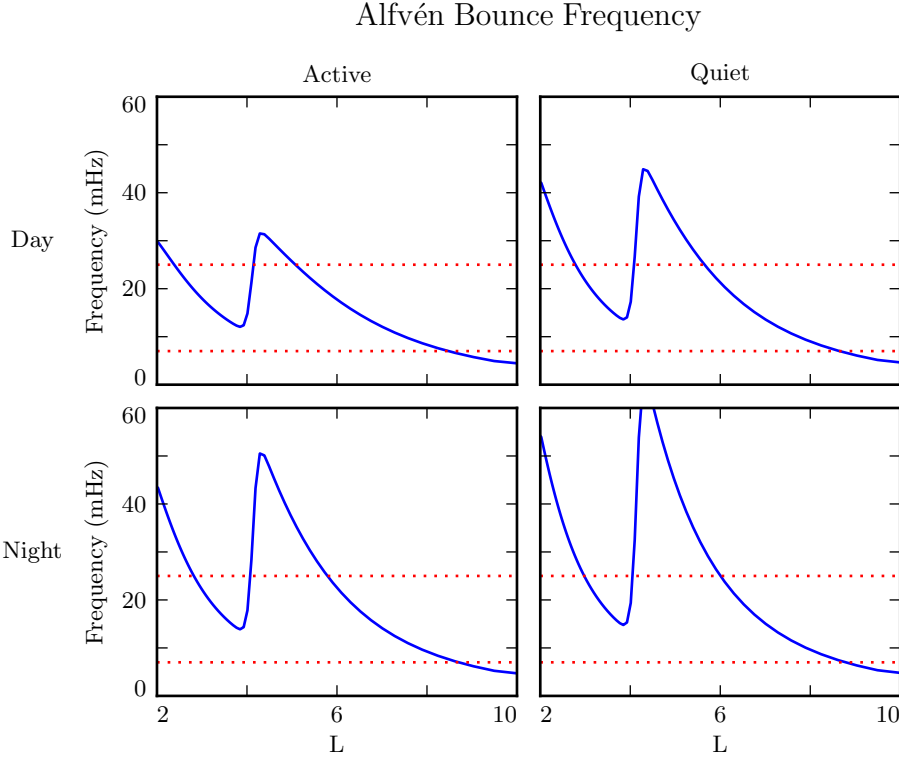


Figure 3.1: The above are bounce frequencies for an Alfvén wave moving back and forth along a geomagnetic field line. Alfvén speeds are computed based on profiles from Kelley[48], as discussed in Section 5.2. Notably, the bounce frequency depends significantly on the position of the plasmasphere, taken here to be at $L = 4$. Dotted lines indicate the P_{c4} frequency range: 7 mHz to 25 mHz.

- 377 parallel to the background magnetic field, contributing to the precipitation of energetic
 378 particles into the neutral atmosphere[32, 33, 94, 104].
- 379 The present chapter introduces the structural characteristics of FLRs, how those charac-
 380 teristics affect wave behavior, and several unresolved questions related to that behavior.
- 381 **TODO:** The polarization of long-period Alfvén waves is rotated by $\sim 90^\circ$ when passing
 382 through the ionosphere[41]. A wave that is azimuthally polarized in space is polarized
 383 north-south on the ground, and vice versa. It has been noted specifically that Pgs
 384 exhibit east-west polarized ground signatures[93].

385 **3.1 Harmonic Structure**

386 Wave structure along a geomagnetic field line is indicated by harmonic number. The
387 first (or fundamental) harmonic has a wavelength twice as long as the field line. The
388 electric field perturbation is zero at the ionospheric foot points of the field line, due
389 to the conductivity of the ionosphere. For the first harmonic, this puts an electric
390 field antinode at the equator, along with a node in the perpendicular⁵ perturbation
391 to the magnetic field. For the second harmonic, the electric field has a third node at
392 the equator, which is accompanied by an antinode in the perpendicular magnetic field
393 perturbation. Figure 3.2 shows a qualitative sketch of the first and second harmonics:
394 a series of snapshots in time, in the rest frame of the wave. Perpendicular electric and
395 magnetic field perturbations are shown in blue and red respectively.

396 A first-harmonic FLR that is periodic or localized in the azimuthal direction is conducive
397 to drift-resonant wave-particle interactions[19, 75]. The particle is like a child on a swing:
398 whenever the path of the particle (or child) gets close to the wave (parent), it gets a
399 push, and always in the same direction. The wave fields spend half its time pointing
400 the other direction, just as the parent must shift their weight backward to get ready for
401 the next push, but at that point the particle (child) is far away.

402 Second-harmonic FLRs interact with particles through the drift-bounce resonance, which
403 is slightly more complicated. As the particle drifts azimuthally, it also zig-zags north-
404 south. The combination of those two periodic motions must align with the phase of
405 the wave electric field. An example path is shown by the purple line in Figure 3.2: the
406 particle experiences a rightward electric field throughout the wave's oscillation.

The drift and drift-bounce resonance conditions is written, respectively[89]:

$$\omega - m\omega_D = 0 \quad \text{and} \quad \omega - m\omega_D = \omega_B \quad (3.2)$$

⁵The parallel, or compressional, magnetic field exhibits the same nodes and antinodes as the perpendicular electric field[78].

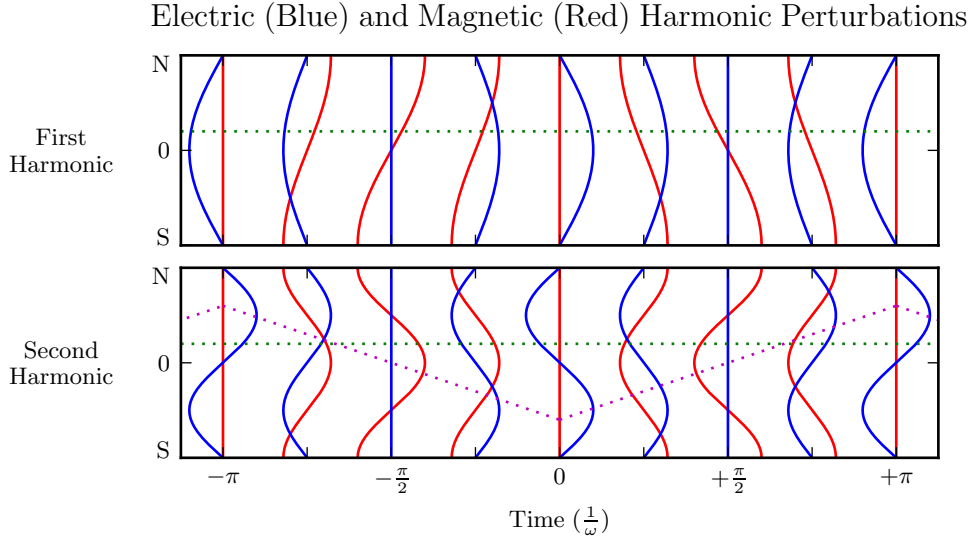


Figure 3.2: The first (or fundamental) harmonic has an antinode in its perpendicular electric field (blue) at the equator, along with a node in its perpendicular magnetic field perturbation (red). A single satellite can identify the first harmonic by the relative phase of the electric and magnetic field perturbations: an observer north of the equator (green) will see the magnetic field perturbation lead the electric field by $\pm 90^\circ$. The second harmonic is the opposite: it has an electric field node at the equator, and an observer north of the equator will see the magnetic field perturbation lag the electric field by $\mp 90^\circ$. Top and bottom signs correspond to the poloidal (shown) and toroidal polarizations respectively. The purple line sketches the path of a particle in drift-bounce resonance; in the particle’s rest frame, the electric field is always to the right.

- 407 Where ω is the frequency of the wave, ω_D and ω_B are the particle’s drift and bounce
- 408 frequencies respectively, and m is the wave’s azimuthal modenumber, as discussed in
- 409 Section 3.2.
- 410 In principle, the first and second harmonics can be distinguished by their frequencies,
- 411 even from a single-point observation[16, 34]. In practice, however, this is not a reliable
- 412 approach[90]. There are significant uncertainties surrounding the mass density profile
- 413 — and thus the Alfvén speed profile — along a geomagnetic field line.
- 414 Harmonic structure can also be deduced by noting the phase offset between the wave
- 415 magnetic field and its electric field (or the plasma velocity)[18, 93]. In Figure 3.2, the
- 416 green line indicates an observer just north of the magnetic equator. For a wave polarized

417 in the poloidal direction (see Section 3.3), the observer sees the electric field waveform
418 offset from the magnetic field by a phase of $\pm 90^\circ$, where the top sign is for odd modes
419 and the bottom sign is for even modes. The signs are flipped for toroidally-polarized
420 waves, and again for waves observed south of the equator.

421 **TODO:** Talk about imaginary Poynting flux? Standing waves don't move energy. Traveling waves do. In practice, everything is a superposition of the two.

423 Notably, the measurement of wave phase has only become viable with the advent of
424 satellites carrying both electric and magnetic field instrumentation, such as THEMIS
425 in 2007[4] and the Van Allen Probes⁶ in 2012[86].

426 Strictly speaking, the the phase offset of the electric and magnetic fields does not provide
427 the harmonic number — only its parity. It's reasonably safe to assume that an even mode
428 is the second harmonic; the second harmonic is by far the most commonly observed[44,
429 83, 91], due in part to its excitement by the antisymmetric balloon instability[10, 12,
430 14, 85]. However, the distinction between the first and third harmonics is not always
431 clear[15, 34]; this issue is discussed further in Chapter 8. Higher harmonics than that
432 are not expected in the Pc4 frequency band.

433 **TODO:** Second-harmonic FLRs are unlikely to cause ground signatures[93].

434 3.2 Azimuthal Modenumber

435 The wavelength of an FLR in the azimuthal direction is indicated by its azimuthal
436 modenumber. A wave with modenumber m has an azimuthal wavelength that spans $\frac{24}{m}$
437 hours in MLT.

438 Waves with small azimuthal modenumbers ($0 < m < 10$) are typically driven by broad-
439 band energy sources at the magnetosphere's boundary, such as variations in the so-
440 lar wind pressure[20, 38, 49, 107, 108], sporadic magnetic reconnection[42], or Kelvin-
441 Helmholtz waves on the magnetopause[11, 57, 84]. In the low- m regime, the shear and
442 compressional Alfvén waves are coupled, which allows energy to move across field lines

⁶The Van Allen Probes were previously called RBSP, for Radiation Belt Storm Probes.

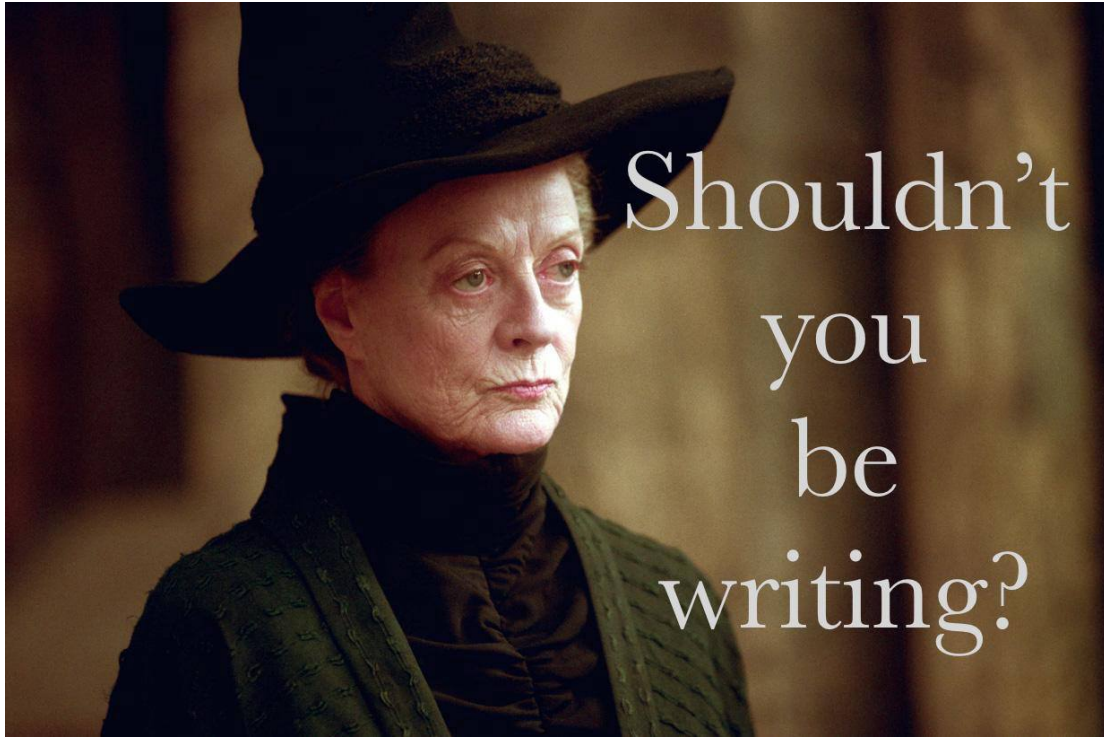


Figure 3.3: TODO: Large and small azimuthal modenumbers.

443 until the driving frequency lines up with the local Alfvén frequency[59]. Because of their
444 broadband energy source, low- m FLRs often have a mishmash of frequencies present in
445 their spectra[18], though the spectra are coherent in terms of harmonic[?].

446 When the azimuthal modenumber is large (or, equally, when the azimuthal wavelength
447 is small), compressional propagation of Alfvén waves becomes evanescent, so the move-
448 ment of energy is guided by magnetic field lines[16, 78]⁷. As a result, FLRs must be
449 driven from within the magnetosphere. Proposed energy sources include phase space
450 gradients near the plasmapause[19], particularly as the plasmasphere refills after a storm
451 or substorm[26, 55].

452 The atmosphere is known to attenuate waves with small spatial extent in the perpendic-
453 ular direction[43, 102, 106]. As a result, FLRs may create no signature on the ground if

⁷Equally, the strength of a wave's parallel component hint at its modenumber, a point which is revisited in Chapter 8.

454 their azimuthal modenumber is large. For example, a recent paper by Takahashi shows
455 a strong (2 nT at $L \sim 10$), clear resonance with $|m| \gtrsim 70$ and no corresponding ground
456 signature[90].

Southwood[85] and Glassmeier[30] show that a low frequency wave passing through the ionosphere on its way to Earth will be attenuated per

$$\frac{B_E}{B_I} = \frac{\Sigma_H}{\Sigma_P} \exp\left(-m \frac{R_I - R_E}{R_E \sin \theta}\right) \quad (3.3)$$

457 Where B_E and B_I are the magnetic field strengths at R_E (Earth's surface, 6783 km
458 geocentric) and R_I (the ionosphere, $\sim 6900 \text{ km}$ geocentric) respectively. The integrated
459 ionospheric Pedersen and Hall conductivities, Σ_P and Σ_H , are typically within a factor
460 of two of one another. Field lines near the plasmapause can be traced to Earth at
461 $\sin \theta \sim 0.4$. That is, by the time it reaches the ground, the magnetic field from an FLR
462 with $m = 10$ is weaker by a factor of two; at $m = 100$, the factor is closer to 100.

463 3.3 Poloidal and Toroidal Polarizations

464 Based on polarization, each FLR can be classified as either poloidal or toroidal. The
465 poloidal mode is a field line displacement in the meridional plane, as shown in Figure 3.4,
466 with an accompanying electric field in the azimuthal direction. The toroidal mode's
467 magnetic displacement is azimuthal, per Figure 3.5; the associated electric field is in the
468 meridional plane.

469 Both poloidal and toroidal waves are noted for their ability to contribute to the energiza-
470 tion and radial diffusion of trapped particles. The poloidal mode interacts more strongly,
471 since its electric field is aligned with the trapped particles' drift motion. Poloidally-
472 polarized waves are also more prone to creating magnetic signatures on the ground, due
473 to ducting in the ionosphere[28, 36].

474 Toroidal modes have been shown to far outnumber poloidal modes[3]. Perhaps not
475 coincidentally, poloidally-polarized waves rotate asymptotically to the toroidal mode[64,
476 65, 78]. Poloidal waves with low azimuthal modenumber — such as those driven by

Poloidal Resonance Structure

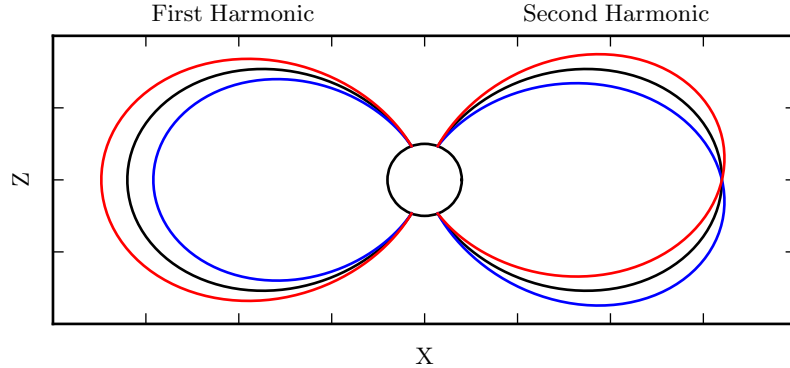


Figure 3.4: The poloidal resonance is a magnetic field in the meridional plane. The displacement is radial near the equator, and can be accompanied by enhancement in the parallel magnetic field near the ionosphere. The first harmonic is shown on the left, and the second harmonic on the right. Lines are colored red and blue only to contrast with the unperturbed black field line.

477 broadband sources at the magnetopause — rotate on timescales comparable to their
478 oscillation periods.

479 TODO: Fishbone instability[13, 67]. Like the poloidal mode, but for lab plasmas.

480 TODO: Poloidal and toroidal modes are coupled by the ionospheric Hall conductivity[47].
481 The Hall conductivity also increases the “ringtime” of these resonances, allowing them
482 to oscillate through the inductive process rather than be dissipated as Joule heating[100].

483

484 TODO: Toroidal modes show a clear frequency dependence with L . Poloidal modes less
485 so. Citation... [?]

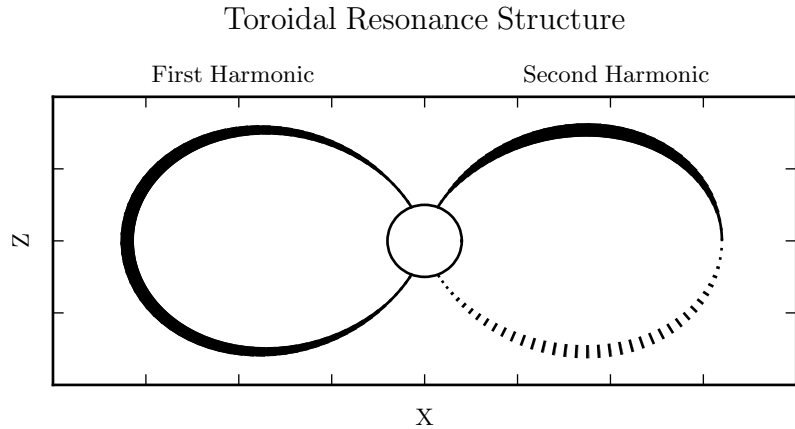


Figure 3.5: A toroidally-polarized FLR has a magnetic perturbation in the azimuthal direction, as shown. Bold lines are taken to be above the page, and dotted lines below the page, with the displacement indicated by the line’s width. The first harmonic — where the entire field line oscillates in and out of the page — is shown on the left. The second harmonic is on the right, with northern and southern halves perturbed in opposite directions.

486 3.4 Giant Pulsations

487 The study of geomagnetic pulsations long predates satellites, sounding rockets, or even
488 the word “magnetohydrodynamics”⁸. Large, regular oscillations in the magnetic field
489 were noted as early as 1901[6]. Eventually, the term “giant pulsation,” or Pg, arose to
490 describe such pulsations.

491 On the ground, Pgs are notable for their strikingly sinusoidal waveforms, their eastward
492 drifts, and their specific occurrence pattern: Pgs are typically seen pre-dawn, at latitudes
493 of 60° to 70°. Pgs generally fall into the Pc4 frequency band⁹. Their harmonic structure
494 was a source of controversy for decades, but recent multisatellite observations seem to be
495 in agreement that they are odd harmonics, probably fundamental[31, 40, 51, 52, 89, 93].
496 They are poloidally polarized, with modenumbers $10 \lesssim m \lesssim 40$ [29, 40, 75, 81, 93].

⁸The term was first used by Alfvén in the 1940s[2].

⁹The Pc4 range is periods of 45 s to 140 s, while Pgs are often said to range from 60 s to 200 s[8].

497 Whereas FLRs are waves in space which may produce ground signatures, “giant pulsation” refers to the ground signature specifically¹⁰. That is, Takahashi’s satellite observation of a sinusoidal, morningside, high- m , fundamental poloidal resonance was not
498
499
500 classified as a Pg because it did not produce a signal on the ground[90].

501 **TODO:** Pgs are localized to within 2° to 5° in latitude[70, 89, 98].

502 Due to their remarkably clear waveforms, Pgs are typically found by “visual inspection
503 of magnetometer data”[70]. Over the course of the past century, a number of multi-year
504 (sometimes multi-decade[8]) surveys have totaled nearly one thousand Pg events. On
505 average, a ground magnetometer near 66° magnetic latitude observes \sim 10 Pg events per
506 year[8, 39, 80, 87]. Observations are not distributed uniformly; rather, giant pulsations
507 become more common near the equinox and during times of low solar activity.

508 Unlike Pc4 pulsations in general, Pgs show no particular correlation with storm phase[70].
509 However, they do often occur as the magnetosphere recovers from a substorn[70, 81].

510 3.5 Motivations for the Present Work

511 A great deal has been learned — and continues to be learned — through observations of
512 field line resonance. However, the cost-to-benefit ratio is climbing. As summarized in the
513 sections above, FLR behavior depends significantly on harmonic structure, azimuthal
514 modenumber, and polarization — not to mention frequency, spectral width, and so
515 on. With each degree of freedom comes the necessity for an additional simultaneous
516 observation.

517 Similarly, as FLRs have been shown to depend on ever-more-specific magnetospheric
518 conditions, analytical techniques have fallen out of favor. The height-resolved iono-
519 sphere, the multidimensional Alfvén speed profile, and the inconvenient geometry com-
520 bine to create a problem beyond the reasonable purview of pencil and paper.

521 That is, the topic of field line resonance is ripe for numerical modeling.

¹⁰Historically, the wave designations shown in Table 3.1 all referred to ground phenomena. Over time, they have come to describe satellite observations as well, including those without corresponding signatures on the ground.

522 Past models of the magnetosphere have been limited in their consideration of FLRs.
523 Reasons include overly-simplified treatment of the ionospheric boundary, no consider-
524 ation of the plasmapause, limited range in m , and the inability to compute ground
525 signatures. Chapter 5 presents a model which addresses these issues, allowing the com-
526 putation of field line resonance with unparalleled attention to realism.

527 The model allows a bird's-eye view of the structure and evolution of FLRs. As such,
528 not only can several open questions be addressed, but their answers serve to unify a
529 number of seemingly-disparate properties described in the sections above.

530 The rotation of poloidally-polarized waves to the toroidal mode is investigated. Par-
531 ticular attention is paid to the importance of azimuthal modenumber and ionospheric
532 conductivity. The interplay between said rotation and the transport of energy across
533 field lines — which also depends on azimuthal modenumber — is considered as well.

534 By their nature, drifting particles have the potential to spur wave-particle interactions
535 at all MLT. However, Pc4 observations are strongly peaked on the dayside. In a 2015
536 paper, Dai notes, “It is not clear why noncompressional [high- m] Pc4 poloidal waves,
537 which are presumably driven by instability within the magnetosphere, preferentially
538 occur on the dayside”[18]. Motoba, later that year, echoes, “It is unclear whether other
539 generation mechanisms of fundamental standing waves ... can explain the localization
540 of Pgs in local time”[70]. This, too, is considered numerically: to what degree is field
541 line resonance affected by the (day-night asymmetric) conditions of the ionosphere?

542 **TODO: Transition... With the above in mind, what data would be super helpful?**

543 It's been shown that a ground magnetometer 66° north of the magnetic equator observes
544 ~ 10 Pg events per year. It's also been shown that poloidal Pc4s are rare compared to
545 toroidal ones, and that most poloidal Pc4s are even harmonics. However, little attention
546 has been paid to how these rates line up with one another. Given the relative occurrence
547 rate of poloidal and toroidal waves, of odd and even harmonics, and of diffuse and sharp
548 spectral peaks, just how unusual are giant pulsations?

549 **Chapter 4**

550 **Waves in Cold Resistive Plasma**

551 Before delving into the implementation of the numerical model, it's instructive to con-
552 sider the fundamental equations of waves in a cold, resistive plasma. Specifically, the
553 present chapter is concerned with waves much slower than the electron cyclotron fre-
554 quency. High-frequency waves such as the L and R modes are beyond the scope of the
555 present work — and, in fact, beyond the limits of the model described in Chapter 5.

The evolution of electric and magnetic fields is governed by Ampère's law and Faraday's law. Notably, the present work takes the linearized versions of Maxwell's equations; the vectors \underline{E} and \underline{B} indicate perturbations above the zeroth-order magnetic field.

$$\underline{\epsilon} \cdot \frac{\partial}{\partial t} \underline{E} = \frac{1}{\mu_0} \nabla \times \underline{B} - \underline{J} \quad \frac{\partial}{\partial t} \underline{B} = -\nabla \times \underline{E} \quad (4.1)$$

Current follows Ohm's law. For currents perpendicular to the background magnetic field, Kirchhoff's formulation is sufficient. Conductivity is much higher along the magnetic field lines¹, so it's appropriate to also include the electron inertial term².

$$0 = \underline{\sigma}_{\perp} \cdot \underline{E}_{\perp} - \underline{J}_{\perp} \quad \frac{1}{\nu} \frac{\partial}{\partial t} J_z = \sigma_0 E_z - J_z \quad (4.2)$$

¹The dipole coordinate system is defined rigorously in Section 5.1; at present, it's sufficient to take \hat{z} parallel to the zeroth-order magnetic field, and \hat{x} and \hat{y} perpendicular to \hat{z} (and to each other).

²Electron inertial effects are not included in the model described in Chapter 5, or in the results in Chapter 7; however, their implementation and impact are explored in Chapter 6.

Derivatives in Equations (4.1) and (4.2) can be evaluated by performing a Fourier transform. They can then be combined, eliminating the magnetic field and current terms.

$$\begin{aligned} 0 &= \underline{\underline{E}}_{\perp} + \frac{v_A^2}{\omega^2} (\underline{k} \times \underline{k} \times \underline{E})_{\perp} + \frac{i}{\epsilon_{\perp}\omega} \underline{\sigma}_{\perp} \cdot \underline{\underline{E}}_{\perp} \\ 0 &= E_z + \frac{c^2}{\omega^2} (\underline{k} \times \underline{k} \times \underline{E})_z + \frac{i\omega_P^2}{\omega(\nu - i\omega)} E_z \end{aligned} \quad (4.3)$$

The speed of light, Alfvén speed (including the displacement current correction), plasma frequency, and parallel conductivity are defined in the usual way:

$$c^2 \equiv \frac{1}{\mu_0\epsilon_0} \quad v_A^2 \equiv \frac{1}{\mu_0\epsilon_{\perp}} \quad \omega_P^2 \equiv \frac{ne^2}{m_e\epsilon_0} \quad \sigma_0 \equiv \frac{ne^2}{m_e\nu} \quad (4.4)$$

Where the perpendicular dielectric constant ϵ_{\perp} is analogous to the electric constant ϵ_0 , but for electric fields which are perpendicular to the preferred direction of the dielectric medium. As noted in Equation (3.1), $\epsilon_{\perp} \equiv \frac{\rho}{B^2}$ where ρ is the mass density and B is the magnitude of the (zeroth-order) magnetic field.

Using the vector identity $\underline{k} \times \underline{k} \times \underline{E} = \underline{k} \underline{k} \cdot \underline{E} - k^2 \underline{E}$, Equation (4.3) can be reassembled into a single expression,

$$0 = \left(\underline{\underline{\mathbb{I}}} + \frac{1}{\omega^2} \underline{\underline{V}}^2 \cdot \underline{k} \underline{k} - \frac{k^2}{\omega^2} \underline{\underline{V}}^2 + \frac{i}{\omega} \underline{\underline{\Omega}} \right) \cdot \underline{\underline{E}} \quad (4.5)$$

Where $\underline{\underline{\mathbb{I}}}$ is the identity tensor and in x - y - z coordinates,

$$\underline{\underline{V}}^2 \equiv \begin{bmatrix} v_A^2 & 0 & 0 \\ 0 & v_A^2 & 0 \\ 0 & 0 & c^2 \end{bmatrix} \quad \text{and} \quad \underline{\underline{\Omega}} \equiv \begin{bmatrix} \frac{\sigma_P}{\epsilon_{\perp}} & \frac{-\sigma_H}{\epsilon_{\perp}} & 0 \\ \frac{\sigma_H}{\epsilon_{\perp}} & \frac{\sigma_P}{\epsilon_{\perp}} & 0 \\ 0 & 0 & \frac{\omega_P^2}{(\nu - i\omega)} \end{bmatrix} \quad (4.6)$$

In Equation (4.5), the expression in parentheses is the dispersion tensor. Nontrivial solutions exist only when its determinant is zero. This gives rise to a seventh-order polynomial in ω , so rather than a direct solution it's necessary to consider limits of specific interest.

564 Without loss of generality, the wave vector \underline{k} may be taken to lie in the x - z plane — that
 565 is, with $k_y = 0$. The distinction between the two perpendicular directions is discussed
 566 in Section 4.4.

567 4.1 Guided Propagation

568 The wave vector of a field line resonance aligns closely to the background magnetic
 569 field. By supposing that the two align exactly (that is, taking $k_x = 0$), the parallel and
 570 perpendicular components of the dispersion relation are decoupled.

The parallel-polarized component — that is, the solution when $E_x = E_y = 0$ — is quadratic, and thus can be solved directly.

$$0 = \omega^2 + i\nu\omega - \omega_P^2 \quad \text{so} \quad \omega = -\frac{i\nu}{2} \pm \sqrt{\omega_P^2 - \frac{\nu^2}{4}} \quad (4.7)$$

571 It bears noting that the plasma frequency is large — not just compared to Pc4 frequencies,
 572 but even compared to the collision frequencies in the ionosphere³.

Expanding Equation (4.7) with respect to large ω_P , the dispersion relation becomes

$$\omega^2 = \omega_P^2 \pm i\nu\omega_P + \dots \quad (4.8)$$

573 Equation (4.8) can hardly be called a wave, as it does not depend on the wave vector
 574 \underline{k} . Rather, it is the plasma oscillation⁴: electrons vibrating in response to a charge
 575 separation along the background magnetic field.

576 The plasma oscillation is not specifically relevant to the study of field line resonance.
 577 The two phenomena are separated by six orders of magnitude in frequency. The topic

³The collision frequency may match or exceed the plasma frequency for a thin slice at the bottom of the ionosphere, where the density of neutral atoms is large; however, it falls off quickly. Above an altitude of 200 km, conservatively[73], the plasma frequency exceeds the collision frequency by an order of magnitude or more.

⁴The plasma oscillation is also called the Langmuir wave, after Irving Langmuir.

578 is revisited in Chapter 6 insomuch as it is inseparable from the electron inertial effects
579 in Ohm's law.

The perpendicular ($E_z = 0$) components of the dispersion relation give an expression quartic in ω .

$$0 = \omega^4 + 2i\frac{\sigma_P}{\epsilon_\perp}\omega^3 - \left(2k_z^2v_A^2 + \frac{\sigma_P^2 + \sigma_H^2}{\epsilon_\perp^2}\right)\omega^2 - 2ik_z^2v_A^2\frac{\sigma_P}{\epsilon_\perp}\omega + k_z^4v_A^4 \quad (4.9)$$

Like the parallel-polarized component above, Equation (4.9) can be solved directly. Noting that \pm and \oplus are independent,

$$\omega = \left(\frac{\pm\sigma_H - i\sigma_P}{2\epsilon_\perp}\right) \oplus \sqrt{k_z^2v_A^2 + \left(\frac{\pm\sigma_H - i\sigma_P}{2\epsilon_\perp}\right)^2} \quad (4.10)$$

Also like the parallel-polarized component, the exact solution is less useful than its Taylor expansion. The Pedersen and Hall conductivities are large near the ionospheric boundary, but fall off quickly; for the vast majority of the field line, the ratios $\frac{\sigma_P}{\epsilon_\perp}$ and $\frac{\sigma_H}{\epsilon_\perp}$ are small compared to field line resonance frequencies. Expanding with respect to small conductivity gives

$$\omega^2 = k_z^2v_A^2 \oplus k_zv_A\frac{\sigma_H \pm i\sigma_P}{\epsilon_\perp} + \dots \quad (4.11)$$

580 This is the shear Alfvén wave, with a shift to its frequency due to the conductivity of
581 the ionosphere. It travels along the background magnetic field like a bead on a string,
582 with electric and magnetic field perturbations perpendicular to the magnetic field line
583 (and to one another).

584 4.2 Compressional Propagation

585 The partner to guided motion is compressional motion; in order for energy to move
586 across field lines, the wave vector must have a component perpendicular to \hat{z} . If the

587 wave vector is completely perpendicular to the magnetic field line ($k_z = 0$), the parallel
588 and perpendicular components of the dispersion relation decouple, as in Section 4.1.

The parallel-polarized ($E_x = E_y = 0$) component of the dispersion relation is

$$0 = \omega^3 + i\nu\omega^2 - (k_x^2 c^2 + \omega_P^2) \omega - ik_x^2 c^2 \nu \quad (4.12)$$

Equation (4.12) can be solved directly, though its solution (as a cubic) is far too long to be useful. Expanding with respect to the large plasma frequency, gives

$$\omega^2 = k^2 c^2 + \omega_P^2 - i\nu\omega_P + \dots \quad (4.13)$$

589 This is the O mode, a compressional wave with an electric field perturbation along
590 the background magnetic field. Like the plasma oscillation discussed in Section 4.1, its
591 frequency is very large compared to that of a field line resonance.

The perpendicular-polarized ($E_z = 0$) component of the compressional dispersion relation is also cubic.

$$0 = \omega^3 + 2i\frac{\sigma_P}{\epsilon_\perp}\omega^2 - \left(2k_x^2 v_A^2 + \frac{\sigma_P^2 + \sigma_H^2}{\epsilon_\perp^2}\right) \omega - ik_x^2 v_A^2 \frac{\sigma_P}{\epsilon_\perp} \quad (4.14)$$

A wave moving across magnetic field lines near the ionospheric boundary will encounter large $\frac{\sigma_P}{\epsilon_\perp}$ and $\frac{\sigma_H}{\epsilon_\perp}$, while at moderate to high altitudes those ratios will be small. Solving Equation (4.14) in those two limits respectively gives:

$$\omega^2 = k_x^2 v_A^2 \pm ik_x v_A \frac{\sigma_P}{\epsilon_\perp} + \dots \quad \text{and} \quad \omega^2 = k_x^2 v_A^2 + \left(\frac{\sigma_H \pm i\sigma_P}{\epsilon_\perp}\right)^2 + \dots \quad (4.15)$$

592 At first glance, both limits of Equation (4.15) appear to describe a compressional Alfvén
593 wave. The magnetic perturbation is along the background magnetic field — indicating
594 compression of the frozen-in plasma — while the electric field perturbation is perpen-
595 dicular to both the magnetic field and the wave vector.

596 However, in the high-conductivity limit, the parenthetical term actually dominates the
 597 Alfvén term, taking values as large as $\sim 10^6$ Hz. Waves at such frequencies are beyond
 598 the scope of the present work. As a matter of curiosity, however, it bears noting that
 599 (as long as $\nu \ll 10^6$ Hz) $\frac{\sigma_H}{\epsilon_{\perp}}$ reduces to the electron cyclotron frequency, $\frac{eB}{m_e}$.

600 4.3 High Altitude Limit

601 In the limit of large radial distance, it's reasonable to take the collision frequency to
 602 zero; doing so also neglects the Pedersen and Hall conductivities.

Whereas in Sections 4.1 and 4.2 it was the parallel-polarized component of the dispersion relation that factored out from the other two, the high altitude limit decouples the component polarized out of the x - z plane. The y -polarized dispersion ($E_x = E_z = 0$) is simply:

$$\omega^2 = k^2 v_A^2 \quad (4.16)$$

603 Equation (4.16) describes an Alfvén wave with an arbitrary angle of propagation. De-
 604 pending on the angle between the wave vector and the background magnetic field, it
 605 could be guided, compressional, or somewhere in between. Regardless of propagation
 606 angle, the electric field perturbation is perpendicular to both the direction of propaga-
 607 tion and the magnetic field perturbation.

The other two components (from $E_y = 0$) of the high altitude dispersion tensor give an expression quadratic in ω^2 :

$$0 = \omega^4 - (k_x^2 c^2 + k_z^2 v_A^2 + \omega_P^2) \omega^2 + k_z^2 v_A^2 \omega_P^2 \quad (4.17)$$

Which can be solved for

$$\omega^2 = \frac{1}{2} (k_x^2 c^2 + k_z^2 v_A^2 + \omega_P^2) \pm \sqrt{\frac{1}{4} (k_x^2 c^2 + k_z^2 v_A^2 + \omega_P^2)^2 - k_z^2 v_A^2 \omega_P^2} \quad (4.18)$$

Noting again that ω_P is very large, the two roots can be expanded to

$$\omega^2 = k_z^2 v_A^2 \left(1 - \frac{k_x^2 c^2 + k_z^2 v_A^2}{\omega_P^2} \right) + \dots \quad \text{and} \quad \omega^2 = k_x^2 c^2 + k_z^2 v_A^2 + \omega_P^2 + \dots \quad (4.19)$$

- 608 The first solution of Equation (4.19) is a shear Alfvén wave, as in Equation (4.11).
- 609 Notably, this form arises only when the parenthetical quantity is close to unity — as it
- 610 is for FLRs. The inertial limit, where frequencies are close to the plasma frequency, is
- 611 beyond the scope of the present work. For that same reason, the second solution (which
- 612 describes an oscillation faster than the plasma frequency) is not further considered.

613 4.4 Implications to the Present Work

- 614 The present section's findings carry three significant implications for the present work.
- 615 First — with the exception of the plasma oscillation and similar modes, which are
- 616 revisited in Chapter 6 — waves propagate at the Alfvén speed. This, in combination
- 617 with the grid configuration, will constrain the time step that can be used to model them
- 618 numerically. The time step must be sufficiently small that information traveling at the
- 619 Alfvén speed cannot “skip over” entire grid cells⁵.

Second, the results of the present section allow an estimate of the magnitude of parallel electric field that might be expected from a field line resonance compared to its perpendicular electric field. Between the full dispersion tenfor form in Equation (4.5) and the Alfvén wave described by Equation (4.19),

$$\left| \frac{E_z}{E_x} \right| = \frac{k_x k_z c^2}{\omega^2 - k_x^2 c^2 - \omega_P^2} \sim \frac{k^2 c^2}{\omega_P^2} \quad (4.20)$$

- 620 In essence, the relative magnitudes of the parallel and perpendicular electric fields should
- 621 be in proportion to the square of the relative magnitudes of the electron inertial length

⁵As is the convention, the time step is scaled down from the smallest Alfvén zone crossing time by a Courant factor, typically 0.1, meaning that it takes at least ten time steps to cross a grid cell.

622 (1 km to 100 km) and the wavelength ($\sim 10^5$ km). That is, parallel electric fields should
623 be smaller than the perpendicular electric fields by six or more orders of magnitude.

624 Finally, the dispersion relations shown above indicate how the behavior of a field line
625 resonance should behave as the azimuthal modenumber becomes large.

626 Whereas the shear Alfvén wave's dispersion relation depends only on the parallel com-
627 ponent of the wave vector, the compressional Alfvén wave depends on its magnitude:
628 $\omega^2 = k^2 v_A^2$. If the frequency is smaller than $k v_A$, the wave will become evanescent. The
629 wave vector's magnitude can be no smaller than its smallest component, however, and
630 the azimuthal component scales with the azimuthal modenumber: $k_y \sim \frac{m}{2\pi r}$.

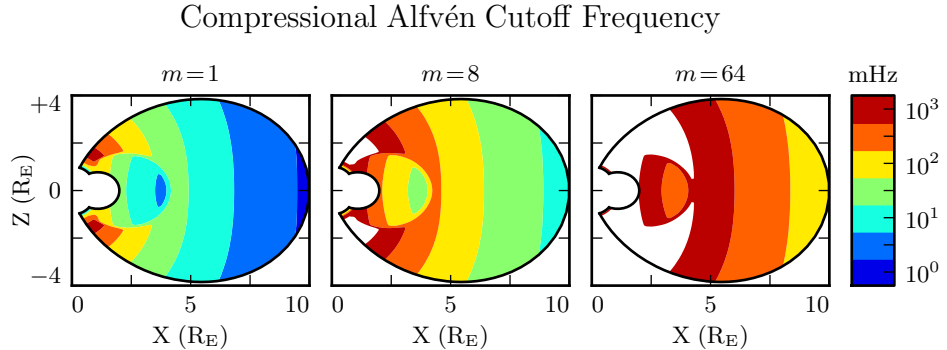


Figure 4.1: Taking $k_y \sim \frac{m}{2\pi r}$ as a lower bound for the magnitude of the wave vector, the above figure demonstrates the lowest frequency at which compressional Alfvén waves may propagate as a function of position and m . Regions shown in white are off the color scale — they have a lower bound on the order of 10^4 mHz or more. The above Alfvén frequency profile is from Kelley[48], for quiet dayside conditions, as discussed in Section 5.2.

631 This imposes a frequency cutoff on compressional Alfvén waves which scales with the
632 azimuthal modenumber, as shown in Figure 4.1. At small values of m , most of the mag-
633 netosphere is conducive to compressional Alfvén waves in the Pc4 frequency range. As
634 m increases, and the wave vector with it, the inner magnetosphere becomes increasingly
635 inaccessible to them.

636 **Chapter 5**

637 **“Tuna Half” Dimensional Model**

638 The present section describes the implementation of Tuna, a new two and a half dimensional
639 Alfvén wave code based largely on work by Lysak[58, 61].

640 The half-integer dimensionality refers to the fact that Tuna’s spatial grid resolves a
641 two-dimensional slice of the magnetosphere, but that electric and magnetic fields —
642 as well as their curls — are three-dimensional vectors. This apparent contradiction is
643 reconciled by the use of a fixed azimuthal modenumber, m . Electric and magnetic fields
644 are taken to be complex-valued, varying azimuthally per $\exp(im\phi)$; derivatives with
645 respect to ϕ are then replaced by a factor of im .

646 Unlike a fully three-dimensional code, Tuna cannot resolve the evolution of wave structures
647 in the azimuthal direction. Furthermore, the model does not allow coupling between
648 the dayside and nightside magnetospheres. What Tuna does offer is efficiency.
649 The model’s economical geometry allows it to include a realistic Earthward boundary:
650 grid spacing on the order of 10 km, a height-resolved ionospheric conductivity tensor,
651 and even the computation of magnetic field signatures at the ground. Such features are
652 computationally infeasible for a large global code.

653 Tuna was developed with field line resonance in mind. As discussed in Chapter 3,
654 such waves are azimuthally localized, minimizing the importance of Tuna’s missing half
655 dimension. Moreover, because field line resonances are known to be affected by both

656 the ionosphere and the plasmasphere, a faithful treatment of the inner magnetosphere
657 is a crucial part of studying them numerically.

658 Perhaps the most exciting feature of Tuna is its novel driving mechanism: ring current
659 perturbation. Codes similar to Tuna have traditionally been driven using compressional
660 pulses at the outer boundary[58, 61, 100, 101]. This has precluded the investigation of
661 waves with large azimuthal modenumber — such as giant pulsations — which are guided,
662 and thus must be driven from within the magnetosphere.

663 TODO: The dipole geometry isn't super new, but it's not widely used. The height-
664 resolved ionosphere is new and exciting! Ground signatures are new and exciting!

665 TODO: The support software — the driver and the plotter — are also significant. Do
666 they get mentioned here? Does the Git repository where the code can be accessed get
667 mentioned here?

668 5.1 Coordinate System

Field line resonance has traditionally been modeled by straightening the field lines into a rectangular configuration[22, 64], by unrolling the azimuthal coordinate into a cylindrical coordinate system[78], or through the use of dipole coordinates[77]¹:

$$x \equiv -\frac{\sin^2 \theta}{r} \quad y \equiv \phi \quad z \equiv \frac{\cos \theta}{r^2} \quad (5.1)$$

669 Where r , θ , and ϕ take on their usual spherical meanings of radial distance, colatitude,
670 and azimuthal angle respectively.

671 The dipole coordinate x is constant over each equipotential shell², y is azimuthal angle,
672 and z indexes each field line from south to north. The unit vectors \hat{x} , \hat{y} , and \hat{z} point

¹The dipole coordinates x , y and z are perhaps more commonly named μ , ϕ , and ν respectively; however, in the present work, μ and ν take other meanings.

²In fact, x is inversely proportional to the McIlwain parameter L .

673 in the crosswise³ (radially outward at the equator), azimuthal (eastward), and parallel
 674 (northward at the equator) directions respectively.

Notably, the dipole coordinates in Equation (5.1) are normal to one another. While mathematically convenient, they do not readily accommodate a fixed-altitude boundary at the ionosphere, nor do they allow the dipole magnetic field to intersect the boundary at an oblique angle, as Earth's field does. As a solution, a nonorthogonal set of dipole coordinates was developed numerically by Proehl[76], then formalized analytically by Lysak[58] in terms of their contravariant components:

$$u^1 = -\frac{R_I}{r} \sin^2 \theta \quad u^2 = \phi \quad u^3 = \frac{R_I^2}{r^2} \frac{\cos \theta}{\cos \theta_0} \quad (5.2)$$

675 Above, R_I is the position of the ionosphere relative to Earth's center; it's typically taken
 676 to be $1 R_E + 100 \text{ km}$.

677 Like the dipole coordinates x , y , and z , Lysak's coordinates u^1 , u^2 , and u^3 correspond to
 678 L -shell, azimuthal angle, and position along a field line respectively. However, compared
 679 to z , u^3 has been renormalized using the invariant colatitude⁴ θ_0 . As a result, u^3 takes
 680 the value $+1$ at the northern ionospheric boundary and -1 at the southern ionospheric
 681 boundary for all field lines.

Because Lysak's coordinate system is not orthogonal⁵, it's necessary to consider covariant and contravariant basis vectors separately.

$$\hat{e}_i \equiv \frac{\partial}{\partial u^i} \underline{x} \quad \hat{e}^i \equiv \frac{\partial}{\partial \underline{x}} u^i \quad (5.3)$$

Covariant basis vectors \hat{e}_i are normal to the curve defined by constant u^i , while contravariant basis vectors \hat{e}^i are tangent to the coordinate curve (equivalently, \hat{e}^i is normal

³In the context of in situ measurements taken near the equatorial plane, \hat{x} is referred to as the radial direction; however, the present work extends the dipole grid to low altitudes, where \hat{x} can be more horizontal than vertical. The term "crosswise" is meant to indicate that \hat{x} is defined by the cross product of \hat{y} and \hat{z} .

⁴The invariant colatitude is the colatitude θ at which a field line intersects the ionosphere. It is related to the McIlwain parameter by $\cos \theta_0 \equiv \sqrt{1 - \frac{R_I}{L}}$.

⁵Curves of constant u^1 and curves of constant u^3 can intersect at non-right angles.

to the plane defined by constant u^j for all $j \neq i$). These vectors are reciprocal⁶ to one another, and can be combined to give components of the metric tensor $\underline{\underline{g}}$ [21].

$$\hat{e}^i \cdot \hat{e}_j = \delta_j^i \quad g_{ij} \equiv \hat{e}_i \cdot \hat{e}_j \quad g^{ij} \equiv \hat{e}^i \cdot \hat{e}^j \quad (5.4)$$

The metric tensor allows rotation between covariant and contravariant representations of vectors.

$$A_i = g_{ij} A^j \quad \text{and} \quad A^i = g^{ij} A_j \quad \text{where} \quad A_i \equiv \underline{A} \cdot \hat{e}_i \quad \text{and} \quad A^i \equiv \underline{A} \cdot \hat{e}^i \quad (5.5)$$

In addition, the determinant of the metric tensor is used to define cross products and curls⁷.

$$(\underline{A} \times \underline{B})^i = \frac{\varepsilon^{ijk}}{\sqrt{g}} A_j B_k \quad \text{and} \quad (\nabla \times \underline{A})^i = \frac{\varepsilon^{ijk}}{\sqrt{g}} \frac{\partial}{\partial u^j} A_k \quad \text{where} \quad g \equiv \det \underline{\underline{g}} \quad (5.6)$$

Explicit forms of the basis vectors and metric tensor can be found in the appendix of Lysak's 2004 paper[58]. At present, it's sufficient to note the mapping between Lysak's basis vectors and the usual dipole unit vectors.

$$\hat{x} = \frac{1}{\sqrt{g^{11}}} \hat{e}^1 \quad \hat{y} = \frac{1}{\sqrt{g^{22}}} \hat{e}^2 \quad \hat{z} = \frac{1}{\sqrt{g^{33}}} \hat{e}^3 \quad (5.7)$$

682 TODO: Do these need to be written out? Referring people to the code, which will be
683 in a public Git repository, is also a possibility.

The basis vectors can also be mapped to the spherical unit vectors, though Equation (5.8) is valid only at the ionospheric boundary.

$$\hat{\theta} = \frac{1}{\sqrt{g_{11}}} \hat{e}_1 \quad \hat{\phi} = \frac{1}{\sqrt{g_{22}}} \hat{e}_2 \quad \hat{r} = \frac{1}{\sqrt{g_{33}}} \hat{e}_3 \quad (5.8)$$

⁶The symbol δ_j^i is the Kronecker delta; the present work also makes use of the Levi-Civita symbol ε^{ijk} and Einstein's convention of implied summation over repeated indeces[24].

⁷The square root of the determinant of the metric tensor is called the Jacobian. It's sometimes denoted using the letter J , which is reserved for current in the present work.

684 The coordinates converge at the equatorial ionosphere, so an inner boundary is necessary
685 to maintain finite grid spacing. It's typically placed at $L = 2$. The outer boundary is
686 at $L = 10$. The dipole approximation of Earth's magnetic field is tenuous at the outer
687 boundary (particularly on the dayside); however, in practice, wave activity is localized
688 inside $L \sim 7$. The grid is spaced uniformly in u^1 , which gives finer resolution close to
689 Earth and coarser resolution at large distances.

690 Spacing in u^3 is set by placing grid points along the outermost field line. The points are
691 closest together at the ionosphere, and grow towards the equator. The spacing increases
692 in a geometric fashion, typically by 3%.

693 Typically, Tuna uses a grid 150 points in u^1 by 350 points in u^3 . The result is a resolution
694 on the order of 10 km at the ionosphere, which increases to the order of 10³ km at the
695 midpoint of the outermost field line.

696 There are no grid points in u^2 due to the two-and-a-half-dimensional nature of the
697 model. Fields are assumed to vary as $\exp(imu^2)$ — equally, $\exp(im\phi)$ — so derivatives
698 with respect to u^2 are equivalent to a factor of im . In effect, the real component of
699 each field is azimuthally in phase with the (purely real) driving, while imaginary values
700 represent behavior that is azimuthally offset.

701 The simulation's time step is set based on the grid spacing. As is the convention, δt is
702 set to match the smallest Alfvén zone crossing time, scaled down by a Courant factor
703 (typically 0.1). It bears noting that the smallest crossing time need not correspond to
704 the smallest zone; the Alfvén speed peaks several thousand kilometers above Earth's
705 surface, in the so-called Ionospheric Alfvén Resonator[61]. A typical time step is on the
706 order of 10⁻⁵ s.

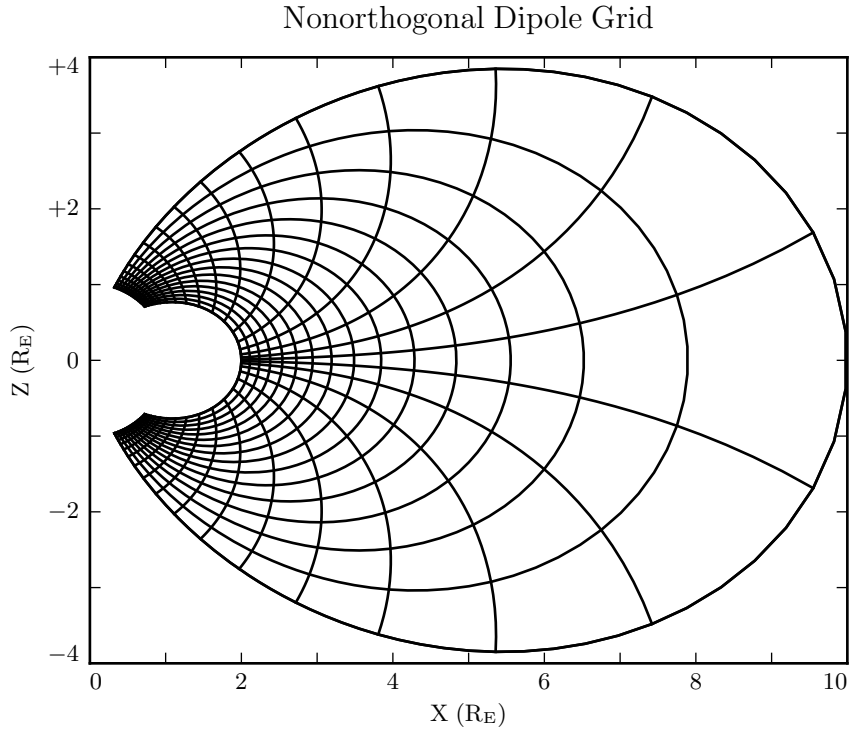


Figure 5.1: The model’s nonorthogonal dipole grid. Every fifth point is shown in each direction. The high concentration of grid points near Earth’s equator is a consequence of the coordinate system, which converges at the equatorial ionosphere. Earth (not shown) is centered at the origin with unit radius.

707 **5.2 Physical Parameter Profiles**

Tuna models Earth’s magnetic field to be an ideal dipole, so the zeroth-order field strength is written in the usual form:

$$\underline{B}_0 = 3.1 \times 10^4 \text{ nT} \left(\frac{R_E}{r} \right)^3 \left(2 \cos \theta \hat{r} - \sin \theta \hat{\theta} \right) \quad (5.9)$$

Number density is taken to be the sum of an inverse-radial-dependent auroral profile and a plasmaspheric profile dependent on the L -shell[61]:

$$n = n_{AZ} \frac{r_{AZ}}{r} + n_{PS} \exp\left(\frac{-L}{L_{PS}}\right) \left(\frac{1}{2} - \frac{1}{2} \tanh \frac{L - L_{PP}}{\delta L_{PP}} \right) \quad (5.10)$$

708 Where typical values are shown in Table 5.1.

Table 5.1: Typical Parameters for the Tuna Density Profile

Variable	Value	Description
L_{PS}	1.1	Scale L of the plasmasphere.
L_{PP}	4.0	Location of the plasmapause.
δL_{PP}	0.1	Thickness of the plasmapause.
n_{AZ}	$10 / \text{cm}^3$	Number density at the base of the auroral zone.
n_{PS}	$10^4 / \text{cm}^3$	Number density at the base of the plasmasphere.
r_{AZ}	1 R_E	Scale height of the auroral density distribution.

The perpendicular component of the electric tensor, ϵ_{\perp} , is computed based on Kelley's[48] tabulated low-density values, ϵ_K , which are adjusted to take into account the effects of high density in the plasmapause.

$$\epsilon_{\perp} = \epsilon_K + \frac{Mn}{B_0^2} \quad (5.11)$$

709 Where M is the mean molecular mass, which is large ($\sim 28 \text{ u}$) at 100 km altitude, then
710 drops quickly (down to 1 u by $\sim 1000 \text{ km}$)[61].

711 The Alfvén speed profile is computed from the perpendicular electric constant in the
712 usual way, $v_A^2 \equiv \frac{1}{\mu_0 \epsilon_{\perp}}$. This form takes into account the effect of the displacement
713 current, which becomes important in regions where the Alfvén speed approaches the
714 speed of light.

715 While the density profile is held constant for all runs discussed in the present work,
716 the Alfvén speed profile is not. Four different profiles are used for the low-density

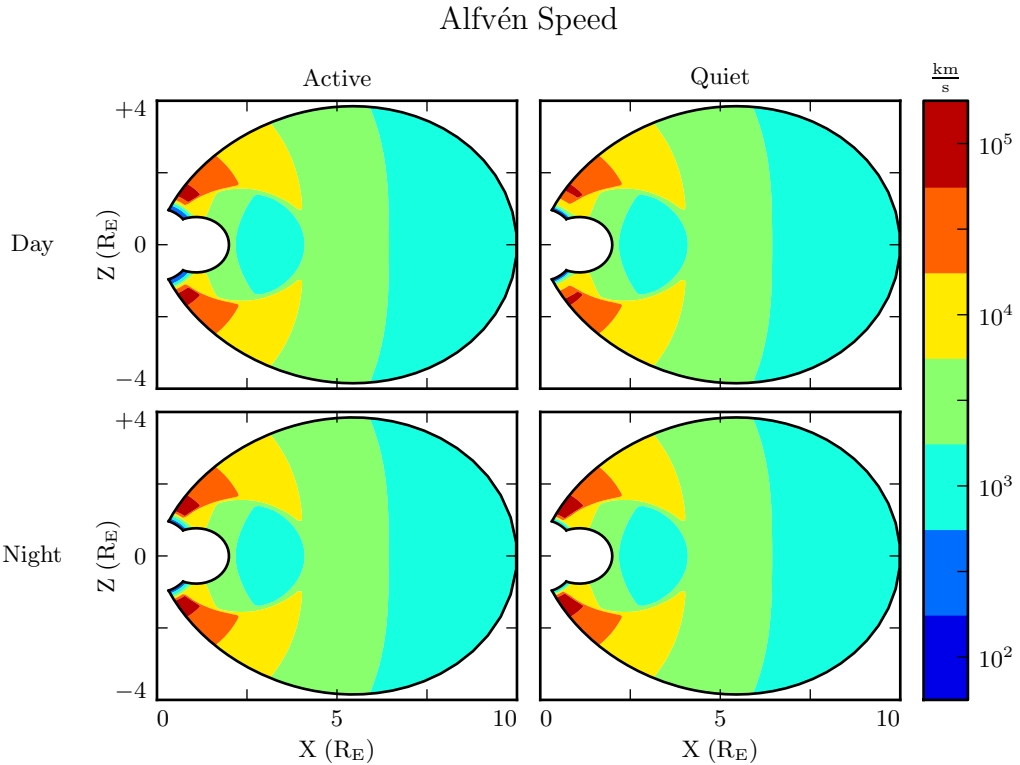


Figure 5.2: Alfvén speed profiles are based on low-density values tabulated by Kelley[48]. They are adjusted to take into account the density of the plasmapause and mass loading near the Earthward boundary.

717 perpendicular electric constant ϵ_K , corresponding to the differing ionospheric conditions
 718 between the dayside and the nightside, and between the high and low points in the
 719 solar cycle. These differences are visible in Figure 5.2, particularly in the size of the
 720 ionospheric Alfvén resonator (the peak in Alfvén speed in the high-latitude ionosphere).

721 **TODO:** Runs are only carried out for day and night... is it even worth showing the
 722 flank profile?

723 Ionospheric conductivity profiles are also based on values tabulated by Kelley, adjusted
 724 by Lysak[61] to take into account the abundance of heavy ions near the Earthward
 725 boundary. Pedersen, Hall, and parallel conductivities are each resolved by altitude, as
 726 shown in Figure 5.3.

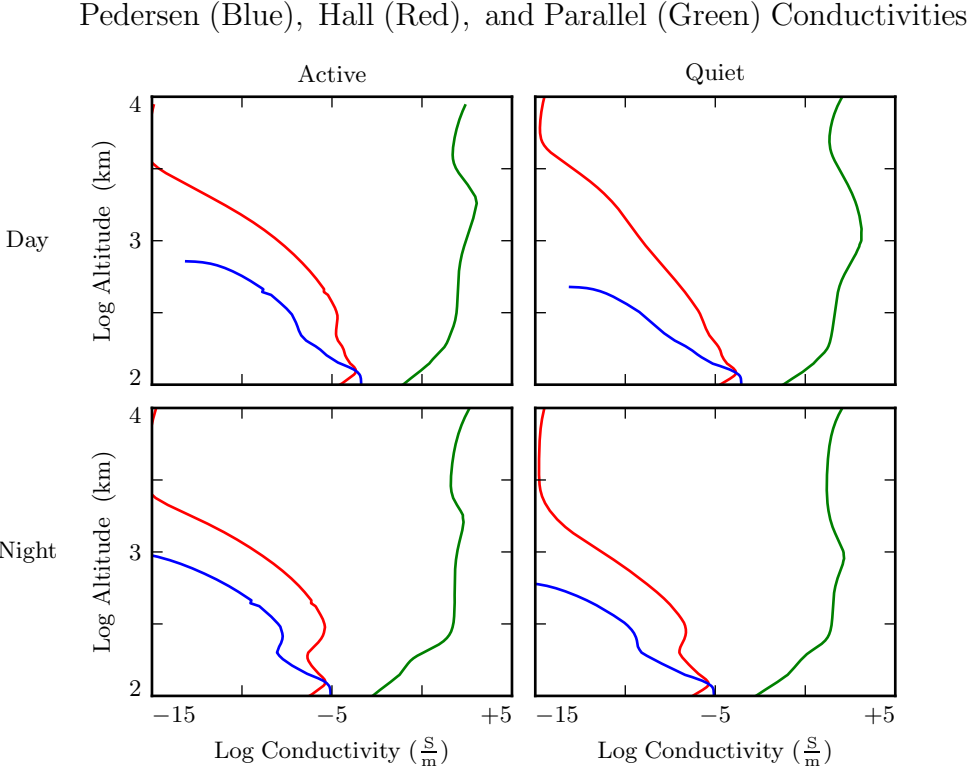


Figure 5.3: Ionospheric conductivity profiles are adapted by Lysak[61] from Kelley's tabulated values[48]. These profiles allow Tuna to simulate magnetosphere-ionosphere coupling under a variety of conditions.

727 Tuna's physical parameter profiles are static over the course of each run. Even so-called
 728 ultra low frequency waves like Pc4 pulsations are fast compared to convective timescales
 729 in the magnetosphere.

730 5.3 Driving

731 Models similar to Tuna have traditionally been driven using compression at the outer
 732 boundary[58, 61, 100, 101]. Such driving acts as a proxy for solar wind compression,
 733 Kelvin-Helmholtz effects at the magnetopause, and so on. However, because of the

734 constraints imposed by the dispersion relation for Alfvén waves⁸, simulations driven from
735 the outer boundary are constrained to the consideration of waves with low azimuthal
736 modenumber (equivalently, large azimuthal wavelength).

737 This issue is demonstrated in Figure 5.4. At low modenumber, energy delivered at
738 the outer boundary propagates across field lines in order to stimulate resonances in
739 the inner magnetosphere. However, as modenumber increases, Alfvén waves become
740 increasingly guided, and the inner magnetosphere is unaffected by perturbations at the
741 outer boundary.

742 In order to simulate high-modenumber Alfvén waves in the inner magnetosphere — such
743 as giant pulsations — a new driving mechanism is necessary. Perturbation of the ring
744 current is a natural choice, as Alfvén waves in the Pc4 range are known to interact with
745 ring current particles through drift and drift-bounce resonances. The ring current is a
746 dynamic region, particularly during and after geomagnetic storms; it's easy to imagine
747 the formation of localized inhomogeneities.

748 In order to estimate an appropriate magnitude for perturbations of the ring current,
749 the Sym-H storm index is used. The index is measured once per minute, and so cannot
750 directly detect ring current modulations in the Pc4 frequency range. Instead, the index
751 is transformed into the frequency domain, allowing a fit of its pink noise⁹.

752 **TODO:** Sym-H is basically the same as DST [99].

753 As shown in Figure 5.5, a Fourier transform of the Sym-H index (taken here from the
754 June 2013 storm) suggests that magnetic field perturbations at Earth's surface due to
755 ring current activity in the Pc4 frequency range could be up to the order of 10^{-2} nT.
756 Supposing that the ring current is centered around $5 R_E$ geocentric, that corresponds to
757 a current on the order of 0.1 MA. Tuna's driving is spread using a Gaussian profile in
758 u^1 (typically centered at $L = 5$) and u^3 (typically centered just off the equator), with a
759 characteristic area of $1 R_E^2$; this gives a current density on the order of $10^{-4} \mu\text{A}/\text{m}^2$.

⁸See Section 4.4.

⁹Pink noise, also called $\frac{1}{f}$ noise, refers to the power law decay present in the Fourier transforms of all manner of physical signals.

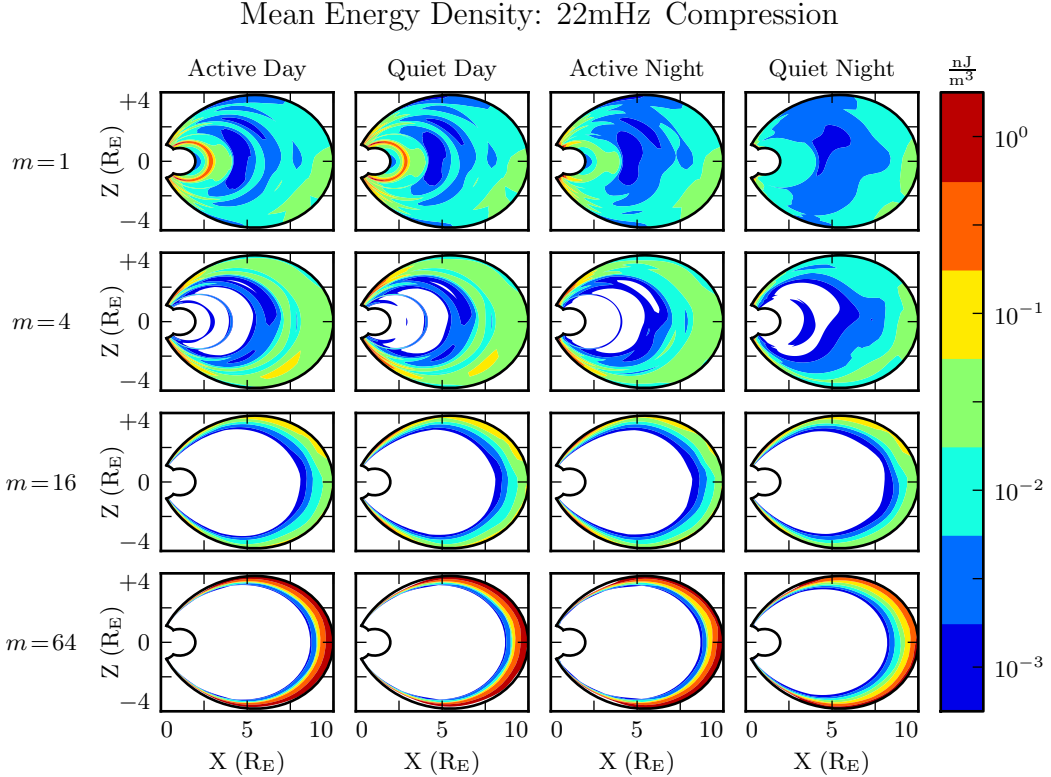


Figure 5.4: Each cell presents the mean energy density over the course of a 300s run, as a function of position, due to compressional driving at the outer boundary. Azimuthal modenumber varies by row, and ionospheric conditions vary by column. For runs with small azimuthal modenumber, it's clear that energy is able to propagate across field lines and stimulate wave activity in the inner magnetosphere. When the modenumber is large, energy is unable to penetrate to the inner magnetosphere. Notably, the large values on the bottom row should be taken with a grain of salt; it's not clear that the model's results are reliable when waves are continuously forced against the boundary.

- 760 TODO: Admittedly, estimating the strength of localized perturbations using Sym-H —
 761 an index averaged over the entire globe — is a bit of a kludge.
- 762 In situ observations of Pc4 pulsations and giant pulsations have shown waves with
 763 modenumbers across the range $1 \lesssim m \lesssim 100$ [18, 19, 90]. Simulations are carried out
 764 across that range, corresponding to ring current perturbations with azimuthal extent as
 765 small as $0.5 R_E$.

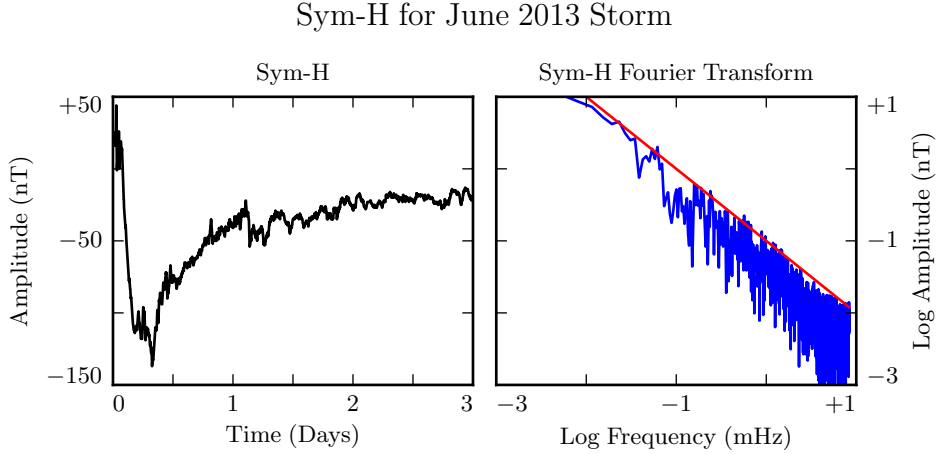


Figure 5.5: The Sym-H storm index[71] measures magnetic perturbations on Earth’s surface due to ring current activity. The amplitude of oscillations in the Pc4 range is estimated by fitting the pink noise in its Fourier transform.

- 766 TODO: Driving is delivered in the azimuthal component of the current only.
- 767 TODO: Driving is sinusoidal.
- 768 TODO: In case it’s not clear: Chapter 7 discusses ONLY simulations using ring current
- 769 driving. The only compressional driving we look at is Figure 5.4.
- 770 TODO: Driving on the dayside is centered at $L = 5$. On the nightside, due to the
- 771 increased Alfvén speed, it’s moved out to $L = 6$. The Alfvén bounce time at $L = 5$ on
- 772 the nightside is well above the Pc4 range.
- 773 TODO: ACTUALLY we should show the runs driven at $L \sim 5$ across the board. Dayside
- 774 and nightside. That way we can make a fair comparison.

775 5.4 Maxwell’s Equations

- 776 Tuna simulates the evolution of electromagnetic waves in accordance with Ampère’s
- 777 law and Faraday’s law. Computation is carried out on a Yee grid[105]: electric fields
- 778 and magnetic fields are offset by half a time step, and each field component is defined

779 on either odd or even grid points in each dimension to ensure that curls are computed
 780 using centered differences.

The Ohmic current in Ampère's law is replaced with $\underline{\sigma} \cdot \underline{E}$ per Kirchhoff's formulation of Ohm's law. Then, taking \underline{J} to represent the driving current discussed in Section 5.3, Maxwell's equations can be written

$$\frac{\partial}{\partial t} \underline{B} = -\nabla \times \underline{E} \quad \underline{\epsilon} \cdot \frac{\partial}{\partial t} \underline{E} = \frac{1}{\mu_0} \nabla \times \underline{B} - \underline{J} - \underline{\sigma} \cdot \underline{E} \quad (5.12)$$

It is convenient to introduce shorthand for the curl of each field: $\underline{C} \equiv \nabla \times \underline{E}$ and $\underline{F} \equiv \nabla \times \underline{B} - \mu_0 \underline{J}$. Or, recalling Equation (5.6),

$$C^i = \frac{\varepsilon^{ijk}}{\sqrt{g}} \frac{\partial}{\partial u^j} E_k \quad F^i = \frac{\varepsilon^{ijk}}{\sqrt{g}} \frac{\partial}{\partial u^j} B_k - J^i \quad (5.13)$$

In these terms, Faraday's law can simply be written:

$$\frac{\partial}{\partial t} B^i = -C^i \quad (5.14)$$

Writing each component out explicitly, and using the metric tensor (per Equation (5.5)) to eliminate contravariant magnetic field components¹⁰, Equation (5.14) becomes:

$$\begin{aligned} B_1 &\leftarrow B_1 - g_{11} \delta t C^1 - g_{13} \delta t C^3 \\ B_2 &\leftarrow B_2 - g_{22} \delta t C^2 \\ B_3 &\leftarrow B_3 - g_{31} \delta t C^1 - g_{33} \delta t C^3 \end{aligned} \quad (5.15)$$

781 Note that the \leftarrow operator is used in Equation (5.15) to indicate assignment, rather than
 782 equality. Terms on the left are new, while those on the right are old.

¹⁰Fields are stored only in terms of their covariant components, and curls in terms of their contravariant components. This reduces Tuna's memory footprint (since each field need not be stored twice) as well as its computational cost (since time need not be spent rotating between bases). As a result, Tuna's solutions to Maxwell's equations are linear expressions whose coefficients are a mishmash of physical constants and geometric factors. To save time, each coefficient is computed once and stored, rather than being multiplied out from scratch with each time step.

Unlike Faraday's law, Ampère's law cannot be trivially solved. Not only does the derivative of \underline{E} depend on its own future value, but the crosswise and azimuthal components of the equation are coupled by the Hall terms in the conductivity tensor. Fortunately, the electric tensor can be inverted, allowing a solution by integrating factors:

$$\underline{\epsilon} \cdot \frac{\partial}{\partial t} \underline{E} = \frac{1}{\mu_0} \underline{F} - \underline{\sigma} \cdot \underline{E} \quad \text{becomes} \quad \left(\underline{\Omega} + \underline{\mathbb{I}} \frac{\partial}{\partial t} \right) \cdot \underline{E} = \underline{V}^2 \cdot \underline{F} \quad (5.16)$$

Where $\underline{\mathbb{I}}$ is the identity tensor and in x - y - z coordinates¹¹,

$$\underline{V}^2 \equiv \frac{1}{\mu_0} \underline{\epsilon}^{-1} = \begin{bmatrix} v_A^2 & 0 & 0 \\ 0 & v_A^2 & 0 \\ 0 & 0 & c^2 \end{bmatrix} \quad \text{and} \quad \underline{\Omega} \equiv \underline{\epsilon}^{-1} \cdot \underline{\sigma} = \begin{bmatrix} \frac{\sigma_P}{\epsilon_{\perp}} & \frac{-\sigma_H}{\epsilon_{\perp}} & 0 \\ \frac{\sigma_H}{\epsilon_{\perp}} & \frac{\sigma_P}{\epsilon_{\perp}} & 0 \\ 0 & 0 & \frac{\sigma_0}{\epsilon_0} \end{bmatrix} \quad (5.17)$$

Multiplying through by $\exp(\underline{\Omega} t)$ and applying the product rule, Equation (5.16) becomes¹²

$$\frac{\partial}{\partial t} \left(\exp(\underline{\Omega} t) \cdot \underline{E} \right) = \exp(\underline{\Omega} t) \cdot \underline{V}^2 \cdot \underline{F} \quad (5.18)$$

Equation (5.18) can then be integrated over a small time step δt and expressed in terms of the assignment operator introduced in Equation (5.15).

$$\underline{E} \leftarrow \exp(-\underline{\Omega} \delta t) \cdot \underline{E} + \delta t \exp(-\underline{\Omega} \frac{\delta t}{2}) \cdot \underline{V}^2 \cdot \underline{F} \quad (5.19)$$

The tensor exponential can be evaluated by splitting $\underline{\Omega}$ into the sum of its diagonal and Hall components¹³. The Hall exponential condenses into sines and cosines, giving a rotation around the magnetic field line:

$$\underline{E} \leftarrow \exp(-\underline{\Omega}' \delta t) \cdot \underline{R}_z \left(\frac{-\sigma_H \delta t}{\epsilon_{\perp}} \right) \cdot \underline{E} + \delta t \underline{V}^2 \cdot \exp(-\underline{\Omega}' \frac{\delta t}{2}) \cdot \underline{R}_z \left(\frac{-\sigma_H \delta t}{2\epsilon_{\perp}} \right) \cdot \underline{F} \quad (5.20)$$

¹¹Note the parallel component of the present definition of $\underline{\Omega}$ differs slightly from that used in Chapter 4, due to the present neglect of inertial effects; see Chapter 6.

¹²Tensor exponentiation is analogous to scalar exponentiation[37]: $\exp(\underline{T}) \equiv \sum_n \frac{1}{n!} \underline{T}^n$.

¹³For tensors, $\exp(\underline{S} + \underline{T}) = \exp(\underline{S}) \exp(\underline{T})$ as long as $\underline{S} \cdot \underline{T} = \underline{T} \cdot \underline{S}$.

Where

$$\underline{\underline{R}}_z(\theta) = \begin{bmatrix} \cos \theta & -\sin \theta & 0 \\ \sin \theta & \cos \theta & 0 \\ 0 & 0 & 1 \end{bmatrix} \quad \text{and} \quad \underline{\underline{\Omega}}' \equiv \begin{bmatrix} \frac{\sigma_P}{\epsilon_{\perp}} & 0 & 0 \\ 0 & \frac{\sigma_P}{\epsilon_{\perp}} & 0 \\ 0 & 0 & \frac{\sigma_0}{\epsilon_0} \end{bmatrix} \quad (5.21)$$

The parallel component of term of Equation (5.20) is simply

$$E_z \leftarrow E_z \exp\left(\frac{-\sigma_0 \delta t}{\epsilon_0}\right) + c^2 \delta t F_z \exp\left(\frac{-\sigma_0 \delta t}{2\epsilon_0}\right) \quad (5.22)$$

Or, using Equation (5.7) to map to the covariant basis,

$$E_3 \leftarrow E_3 \exp\left(\frac{-\sigma_0 \delta t}{\epsilon_0}\right) + c^2 \delta t (g_{31} F^1 + g_{33} F^3) \exp\left(\frac{-\sigma_0 \delta t}{2\epsilon_0}\right) \quad (5.23)$$

783 Tuna's conductivity profile gives a minimum value of $\frac{\sigma_0 \delta t}{\epsilon_0}$ on the order of 10^3 , making
 784 $\exp\left(\frac{-\sigma_0 \delta t}{\epsilon_0}\right)$ far too small to be stored in a double precision variable¹⁴. That is, this
 785 model takes E_3 (and, proportionally, E_z) to be uniformly zero. This issue is revisited
 786 in Chapter 6.

The perpendicular components of Equation (5.20) give the expressions:

$$\begin{aligned} E_1 + \frac{g^{13}}{g^{11}} E_3 &\leftarrow E_1 \cos\left(\frac{-\sigma_H \delta t}{\epsilon_{\perp}}\right) \exp\left(\frac{-\sigma_P \delta t}{\epsilon_{\perp}}\right) \\ &\quad + E_2 \sin\left(\frac{-\sigma_H \delta t}{\epsilon_{\perp}}\right) \exp\left(\frac{-\sigma_P \delta t}{\epsilon_{\perp}}\right) \sqrt{\frac{g^{22}}{g^{11}}} \\ &\quad + E_3 \cos\left(\frac{-\sigma_H \delta t}{\epsilon_{\perp}}\right) \exp\left(\frac{-\sigma_P \delta t}{\epsilon_{\perp}}\right) \frac{g^{13}}{g^{11}} \\ &\quad + F^1 \cos\left(\frac{-\sigma_H \delta t}{2\epsilon_{\perp}}\right) \exp\left(\frac{-\sigma_P \delta t}{2\epsilon_{\perp}}\right) \frac{v_A^2 \delta t}{g^{11}} \\ &\quad + F^2 \sin\left(\frac{-\sigma_H \delta t}{2\epsilon_{\perp}}\right) \exp\left(\frac{-\sigma_P \delta t}{2\epsilon_{\perp}}\right) \frac{v_A^2 \delta t}{\sqrt{g^{11} g^{22}}} \end{aligned} \quad (5.24)$$

¹⁴Not coincidentally, $\frac{\sigma_0}{\epsilon_0}$ can also be written $\frac{\omega_P^2}{\nu}$. At the ionosphere, the collision frequency ν is fast compared to field line resonance timescales, but it's still slow compared to the plasma frequency.

and

$$\begin{aligned}
E_2 \leftarrow & -E_1 \sin\left(\frac{-\sigma_H \delta t}{\epsilon_{\perp}}\right) \exp\left(\frac{-\sigma_P \delta t}{\epsilon_{\perp}}\right) \sqrt{\frac{g^{11}}{g^{22}}} \\
& + E_2 \cos\left(\frac{-\sigma_H \delta t}{\epsilon_{\perp}}\right) \exp\left(\frac{-\sigma_P \delta t}{\epsilon_{\perp}}\right) \\
& - E_3 \sin\left(\frac{-\sigma_H \delta t}{\epsilon_{\perp}}\right) \exp\left(\frac{-\sigma_P \delta t}{\epsilon_{\perp}}\right) \frac{g^{13}}{\sqrt{g^{11} g^{22}}} \\
& - F^1 \sin\left(\frac{-\sigma_H \delta t}{2\epsilon_{\perp}}\right) \exp\left(\frac{-\sigma_P \delta t}{2\epsilon_{\perp}}\right) \frac{v_A^2 \delta t}{\sqrt{g^{11} g^{22}}} \\
& + F^2 \cos\left(\frac{-\sigma_H \delta t}{2\epsilon_{\perp}}\right) \exp\left(\frac{-\sigma_P \delta t}{2\epsilon_{\perp}}\right) \frac{v_A^2 \delta t}{g^{22}}
\end{aligned} \tag{5.25}$$

787 The E_3 terms in Equations (5.24) and (5.25) can be ignored at present. They are
788 revisited in Chapter 6.

789 It bears recalling that the driving current is defined as part of \underline{F} , per Equation (5.13).
790 When the driving current is purely azimuthal ($J^1 = J^3 = 0$), the driving is in principle
791 applied to both the poloidal and the toroidal electric fields through F^2 . However,
792 in practice, the driving applied to the toroidal electric field is vanishingly small. The
793 driving current J^2 is localized around $5 R_E$ geocentric, and $\exp\left(\frac{-\sigma_P \delta t}{2\epsilon_{\perp}}\right)$ drops off quickly
794 with altitude.

795 5.5 Boundary Conditions

796 Dirichlet and Neumann boundary conditions are applied to the electric field components
797 and magnetic field components respectively. That is, electric fields are forced to go to
798 zero at the inner and outer boundaries, and magnetic fields are forced to have a zero
799 derivative normal to the inner and outer boundaries.

800 These boundary conditions can in principle cause nonphysical reflections at the bound-
801 ary¹⁵. However, in practice, wave activity is concentrated well within the simulation
802 domain. Simulation results are robust under an exchange of Dirichlet and Neumann

¹⁵See, for example, the bottom row of Figure 5.4.

boundary conditions (though a self-inconsistent set of boundary conditions, such as applying Neumann boundary conditions to B_1 but Dirichlet boundary conditions to B_3 , quickly causes instability).

The Earthward boundary conditions are as follows.

Between the top of the neutral atmosphere and the bottom of the ionosphere, the model includes a thin, horizontal current sheet representing the ionosphere's E layer[58]. By integrating Ampère's law over the layer, it can be shown[28] that the horizontal electric field values at the edge of the grid are determined by the jump in the horizontal magnetic fields:

$$\underline{\underline{\Sigma}} \cdot \underline{E} = \frac{1}{\mu_0} \lim_{\delta r \rightarrow 0} \left[\hat{r} \times \underline{B} \right]_{R_I - \delta r}^{R_I + \delta r} \quad (5.26)$$

The integrated conductivity tensor $\underline{\underline{\Sigma}}$ can be written in θ - ϕ coordinates as[58]:

$$\underline{\underline{\Sigma}} \equiv \begin{bmatrix} \frac{\Sigma_0 \Sigma_P}{\Sigma_0 \cos^2 \alpha + \Sigma_P \sin^2 \alpha} & \frac{-\Sigma_0 \Sigma_H}{\Sigma_0 \cos^2 \alpha + \Sigma_P \sin^2 \alpha} \\ \frac{\Sigma_0 \Sigma_H}{\Sigma_0 \cos^2 \alpha + \Sigma_P \sin^2 \alpha} & \Sigma_P + \frac{\Sigma_H^2 \sin^2 \alpha}{\Sigma_0 \cos^2 \alpha + \Sigma_P \sin^2 \alpha} \end{bmatrix} \quad (5.27)$$

Where α is the angle between the magnetic field and the vertical direction, given by $\cos \alpha \equiv \frac{-2 \cos \theta}{\sqrt{1+3 \cos^2 \theta}}$, and Σ_P , Σ_H , and Σ_0 are the height-integrated Pedersen, Hall, and parallel conductivities respectively. Their values are determined by integrating Kelley's[48] conductivity profiles from Earth's surface to the ionospheric boundary; values are shown in Table 5.2.

Table 5.2: Integrated Atmospheric Conductivity (S)

	Σ_0	Σ_P	Σ_H
Active Day	424	0.65	6.03
Quiet Day	284	0.44	4.02
Active Night	9	0.01	0.12
Quiet Night	9	0.01	0.12

An expression for the horizontal electric fields at the boundary can be obtained by inverting Equation (5.26). After mapping to covariant coordinates per Equation (5.8), and taking $\Sigma \equiv \det \underline{\underline{\Sigma}}$,

$$\begin{aligned} E_1 &\leftarrow \frac{1}{\mu_0 \Sigma} \lim_{\delta r \rightarrow 0} \left[-\Sigma_{\theta\phi} B_1 - \sqrt{\frac{g_{11}}{g_{22}}} \Sigma_{\phi\phi} B_2 \right]_{R_I-\delta r}^{R_I+\delta r} \\ E_2 &\leftarrow \frac{1}{\mu_0 \Sigma} \lim_{\delta r \rightarrow 0} \left[\sqrt{\frac{g_{22}}{g_{11}}} \Sigma_{\theta\theta} B_1 + \Sigma_{\phi\theta} B_2 \right]_{R_I-\delta r}^{R_I+\delta r} \end{aligned} \quad (5.28)$$

812 In order to compute the atmospheric magnetic field, a scalar magnetic potential (Ψ
813 such that $\underline{B} = \nabla\Psi$) is computed as a linear combination of harmonics. The neutral
814 atmosphere is considered to be a perfect insulator, giving $\nabla \times \underline{B} = 0$. Combined with
815 $\nabla \cdot \underline{B} = 0$ (per Maxwell's equations), Ψ satisfies Laplace's equation, $\nabla^2\Psi = 0$.

Laplace's equation can be solved analytically; however, a numerical solution is preferable to ensure orthonormality on a discrete and incomplete¹⁶ grid. After separating out the radial and azimuthal dependence in the usual way, the latitudinal component of Laplace's equation can be written in terms of $s \equiv -\sin^2\theta$:

$$(4s^2 + 4s) \frac{d^2}{ds^2} Y_\ell + (4 + 6s) \frac{d}{ds} Y_\ell - \frac{m^2}{s} Y_\ell = \ell(\ell+1) Y_\ell \quad (5.29)$$

Using centered differences to linearize the derivatives, Equation (5.29) becomes a system of coupled linear equations, one per field line. It can be solved numerically for eigenvalues $\ell(\ell+1)$ and eigenfunctions Y_ℓ ¹⁷. In terms of the harmonics Y_ℓ , Ψ between the Earth's surface and the top of the atmosphere can be written using eigenweights a_ℓ and b_ℓ :

$$\Psi = \sum_\ell \left(a_\ell r^\ell + b_\ell r^{-\ell-1} \right) Y_\ell \quad (5.30)$$

¹⁶As discussed in Section 5.1, the grid is constrained to finite L , which excludes the equator as well as the poles.

¹⁷Solving Laplace's equation analytically results in spherical harmonics indexed by both ℓ and m , the separation constants for θ and ϕ respectively. In two and a half dimensions, ϕ is not explicitly resolved, so m is set manually.

As a boundary condition for Ψ , Earth is assumed to be a perfect conductor. This forces the magnetic field at Earth's surface to be horizontal; that is, $B_r = \frac{\partial}{\partial r} \Psi = 0$. Noting that solutions to Laplace's equation are orthonormal, each element of the sum in Equation (5.30) must be independently zero at R_E . This allows the coefficients a_ℓ and b_ℓ to be expressed in terms of one another.

$$b_\ell = \frac{\ell}{\ell + 1} R_E^{2\ell+1} a_\ell \quad (5.31)$$

The current sheet at the top of the atmosphere is assumed to be horizontal, so the radial component of the magnetic field must be the same just above and just below it. Taking the radial derivative of Equation (5.30) at the top of the atmosphere, and eliminating b_ℓ with Equation (5.31), gives

$$B_r = \sum_\ell \ell a_\ell R_I^{\ell-1} \left(1 - \lambda^{2\ell+1}\right) Y_\ell \quad \text{where} \quad \lambda \equiv \frac{R_E}{R_I} \sim 0.975 \quad (5.32)$$

The summation can be collapsed by “integrating” over a harmonic¹⁸. Inverse harmonics can be obtained by inverting the eigenvector matrix. Then $Y_\ell \cdot Y_{\ell'}^{-1} = \delta_{\ell\ell'}$ by construction.

$$a_\ell = \frac{1}{\ell R_I^{\ell-1}} \frac{B_r \cdot Y_\ell^{-1}}{1 - \lambda^{2\ell+1}} \quad (5.33)$$

Combining Equations (5.30), (5.31), and (5.33) allows the expression of Ψ at the top and bottom of the atmosphere as a linear combination of radial magnetic field components at the bottom of the ionosphere.

$$\begin{aligned} \Psi_E &= \sum_\ell Y_\ell \frac{R_I}{\ell (\ell - 1)} \frac{(2\ell - 1) \lambda^\ell}{1 - \lambda^{2\ell+1}} B_r \cdot Y_\ell^{-1} \\ \Psi_I &= \sum_\ell Y_\ell \frac{R_I}{\ell (\ell - 1)} \frac{(\ell - 1) + \ell \lambda^{2\ell+1}}{1 - \lambda^{2\ell+1}} B_r \cdot Y_\ell^{-1} \end{aligned} \quad (5.34)$$

¹⁸Because the functions are defined on a discrete grid, their inner product is not an integral, but a sum: $B_r \cdot Y_\ell^{-1} \equiv \sum_i B_r[i] Y_\ell^{-1}[i]$.

Horizontal magnetic fields are obtained by taking derivatives of Ψ .

$$B_1 = \frac{\partial}{\partial u^1} \Psi \quad B_2 = \frac{\partial}{\partial u^2} \Psi \quad (5.35)$$

- 816 Horizontal magnetic field values at the top of the atmosphere are used to impose bound-
817 ary conditions on the electric fields at the bottom of the ionosphere, per Equation (5.28).
818 Those at Earth's surface are valuable because they allow a direct comparison between
819 model output and ground magnetometer data, after being mapped to physical coordi-
820 nates per Equation (5.8).

821 **Chapter 6**

822 **Electron Inertial Effects**

823 As laid out in Chapter 5, Tuna resolves neither parallel currents nor parallel electric
824 fields. This is unfortunate; parallel electric fields generated by kinetic and inertial Alfvén
825 waves (including fundamental field line resonances[79, 95]) are a topic of particular
826 interest in the study of auroral particle precipitation.

Parallel currents and electric fields can be added to Tuna through the consideration of electron inertial effects in Ohm's law:

$$0 = \sigma_0 E_z - J_z \quad \text{becomes} \quad \frac{1}{\nu} \frac{\partial}{\partial t} J_z = \sigma_0 E_z - J_z \quad (6.1)$$

With the addition of the electron inertial term, it is necessary to track the parallel current independent of the parallel electric field¹. Solving by integrating factors² gives

$$J_3 \leftarrow J_3 \exp(-\nu \delta t) + \delta t \frac{ne^2}{m_e} E_3 \exp\left(-\nu \frac{\delta t}{2}\right) \quad (6.2)$$

¹The parallel current J_z is defined on the same points of the Yee grid as E_z . It is offset in time by half of a time step.

²The integrating factors technique is laid out explicitly for Ampère's law in Section 5.4.

From there, the parallel electric field can be updated directly; Equation (5.23) is replaced by the following:

$$E_3 \leftarrow E_3 + c^2 \delta t (g_{31} F^1 + g_{33} F^3) - \frac{\delta t}{\epsilon_0} J_3 \quad (6.3)$$

827 The present section explores the complications that arise from the addition of the elec-
 828 tron inertial term to Ohm's law, as well as a few results that may be gleaned despite
 829 those complications. Notably — for reasons discussed in Section 6.3 — the results
 830 presented in Chapter 7 do not make use of the electron inertial term.

831 6.1 The Boris Factor

With the addition of the electron inertial term, a cyclical dependence appears between Ampère's law and Ohm's law:

$$\frac{\partial}{\partial t} E_z \sim -\frac{1}{\epsilon_0} J_z \quad \text{and} \quad \frac{\partial}{\partial t} J_z \sim \frac{ne^2}{m_e} E_z \quad \text{so} \quad \frac{\partial^2}{\partial t^2} E_z \sim -\omega_P^2 E_z \quad (6.4)$$

832 That is, electron inertial effects come hand in hand with the plasma oscillation.
 833 As mentioned in Chapter 4 and shown in Figure 6.1, plasma oscillation is quite fast —
 834 several orders of magnitude smaller than Tuna's time step as determined in Section 5.1
 835 ($\sim 10 \mu s$). This poses a conundrum. At Tuna's usual time step, the plasma oscillation
 836 becomes unstable within seconds³. On the other hand, reducing the time step by three
 837 orders of magnitude to resolve the plasma oscillation is computationally infeasible; a
 838 run slated for an hour would require six weeks to complete.
 839 As it happens, this problem can be solved by artificially increasing the parallel electric
 840 constant above its usual value of ϵ_0 . Doing so lowers both the speed of light and the
 841 plasma frequency within the simulation.
 842 This technique — and others like it — has been widespread in numerical modeling since
 843 it was presented by Boris in 1970[7]. More recently, Lysak and Song considered its use

³For stability, $\omega_P \delta t < 1$ is necessary.

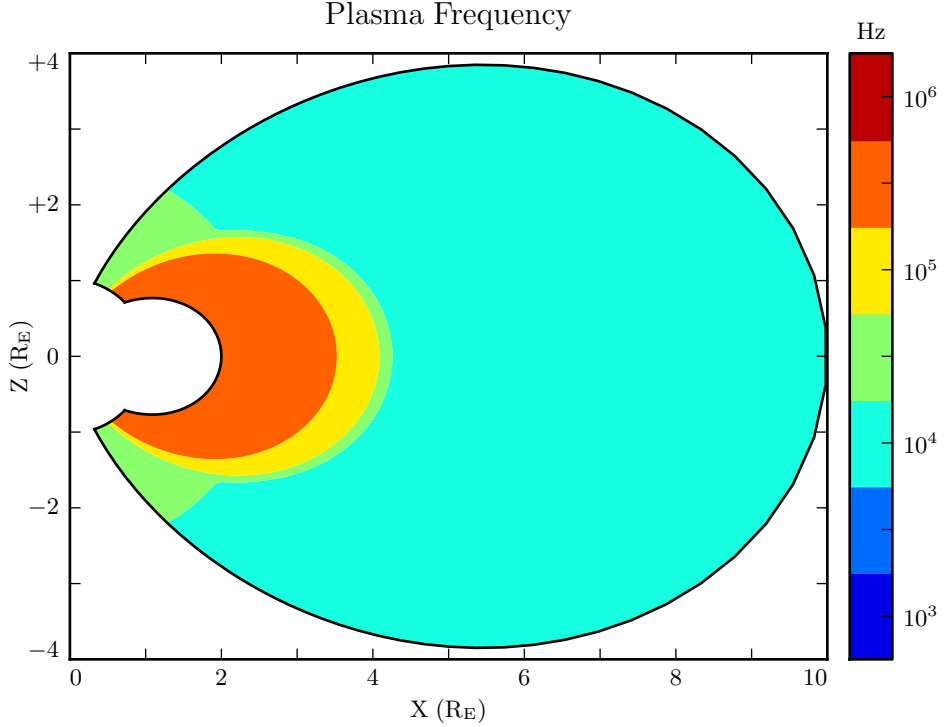


Figure 6.1: The plasma frequency reaches a peak value just under 10^6 Hz near the equator. Outside the plasmasphere, its value is closer to 10^4 Hz, which is still not well-resolved by Tuna's usual time step.

⁸⁴⁴ specifically for the case of electron inertial effects[60]. The following paraphrases their
⁸⁴⁵ argument.

Supposing that the current and electric field are oscillating at frequency ω , the parallel components of Ampère's law and Ohm's law can be written

$$-i\omega\epsilon_0 E_z = \frac{1}{\mu_0} (\nabla \times \underline{B})_z - J_z \quad -\frac{i\omega}{\nu} J_z = \sigma_0 E_z - J_z \quad (6.5)$$

Then, eliminating the current, the parallel electric field can be related to the curl of the magnetic field by⁴

$$\left(1 - \frac{\omega^2 - i\nu\omega}{\omega_P^2}\right) E_z = \frac{c^2}{\omega_P^2} (\nu - i\omega) (\nabla \times \underline{B})_z \quad (6.6)$$

- In Equation (6.6), $\frac{c}{\omega_P}$ is the electron inertial length. While the speed of light and the plasma frequency each depend on ϵ_0 , their ratio does not. This allows an estimation of how much the model should be affected by an artificially-large electric constant (and thus an artificially-small plasma frequency). So long as $\frac{\omega^2 - i\nu\omega}{\omega_P^2}$ remains small compared to unity, the model should behave faithfully.
- For waves with periods of a minute or so, even perhaps-implausibly large Boris factors are allowed; for example, increasing ϵ_0 by a factor of 10^6 gives $\left|\frac{\omega^2 + i\omega\nu}{\omega_P^2}\right| \lesssim 0.01$.

6.2 Parallel Currents and Electric Fields

- As discussed in Section 4.4, parallel electric fields in this regime are expected to be six or more orders of magnitude smaller than the perpendicular electric fields. Numerical results show general agreement: in Figure 6.2, the parallel electric field appears comparable to its perpendicular counterparts only after its been scaled up by six orders of magnitude.
- As such, the inclusion of electron inertial effects does not appreciably impact the simulation's gross behavior; in Faraday's law, $\nabla \times \underline{E}$ is essentially unaffected. Side by side snapshots of the magnetic fields in runs carried out with and without electron inertial effects are not visibly distinguishable⁵ (not shown).
- Even if there is no significant feedback through Faraday's law, it's informative to consider the structures that arise in parallel currents and electric fields driven by perturbations in the ring current. For example, the parallel electric field perturbation (with

⁴From Equation (4.4), $c^2 \equiv \frac{1}{\mu_0 \epsilon_0}$ and $\sigma_0 \equiv \frac{ne^2}{m_e \nu}$ and $\omega_P^2 \equiv \frac{ne^2}{m_e \epsilon_0}$.

⁵In a sense, this is reassuring. It ensures that the present section does not cast doubt on the results presented in Chapter 7, where electron inertial effects are neglected.

Electric Field Snapshots: Quiet Day, 10mHz Current, $m = 16$

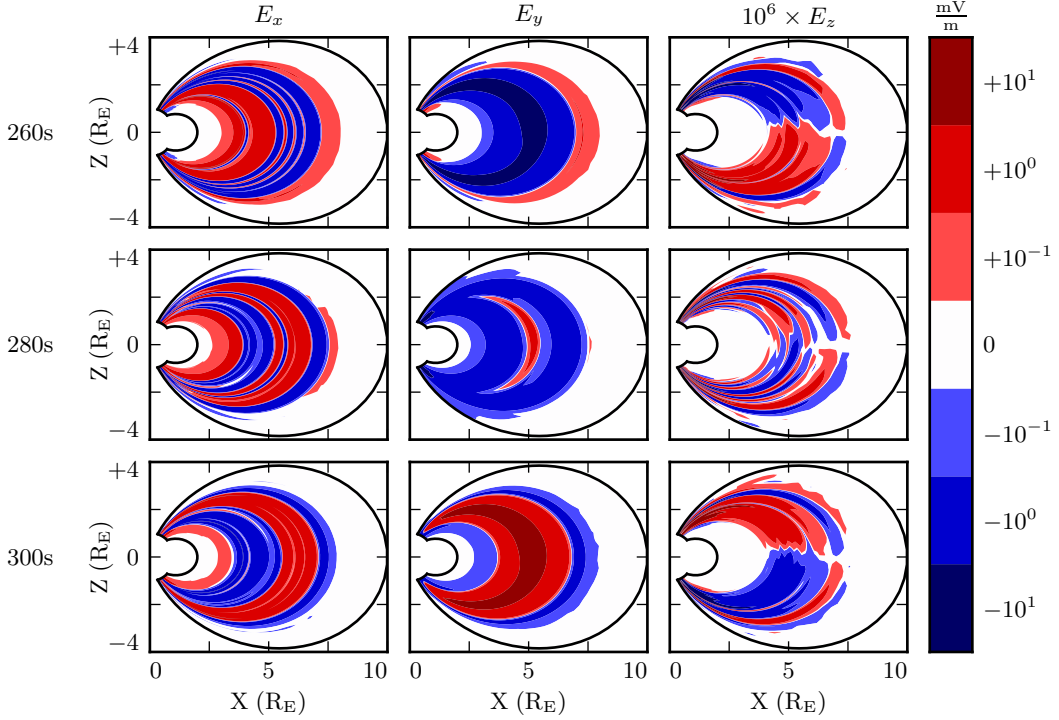


Figure 6.2: Parallel electric fields are smaller than perpendicular electric fields by about six orders of magnitude. As a result, parallel electric fields do not contribute significantly to $\nabla \times \underline{E}$ in Faraday's law.

maxima near the ionosphere) exhibits the opposite harmonic structure to the perpendicular electric field components (which peak near the equator). It is furthermore notable that the parallel electric field (and the parallel current that comes from it) exhibits real and imaginary components of comparable magnitude.

TODO: The compressional component of the magnetic field is also flipped compared to the perpendicular components. Should this have been mentioned in Chapter 3, with the figures showcasing harmonic structure? Radoski showed that it should be the case[78].

873

At low altitude, where the Hall conductivity muddles all of the electric field components together, parallel currents coincide with strong Poynting flux. The imaginary component

Current and Poynting Flux at 100km: Quiet Day , 16mHz Current

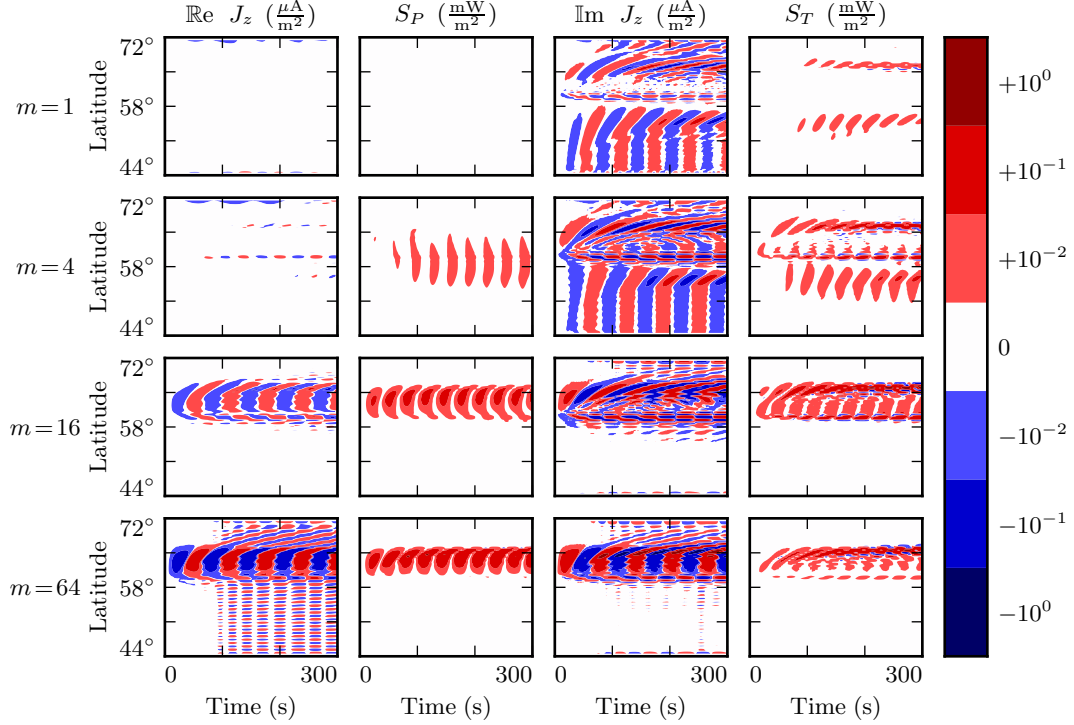


Figure 6.3: TODO: ...

of the current lines up with the toroidal Poynting flux (which comes from imaginary E_x and imaginary B_y^*), while the real current lines up with the poloidal Poynting flux (E_y and B_x^* are real)⁶. This is shown in Figure 6.3, which lays out the real and imaginary components of the parallel current (in the first and third column respectively) next to the poloidal and toroidal Poynting flux (second and fourth columns). Four runs are shown, one per row, with azimuthal modenumbers 1, 4, 16, and 64. Values are measured at an altitude of 100 km, the edge of the simulation.

Notably, the Poynting flux waveforms are rectified — they primarily carry energy Earthward. The current, on the other hand, alternates between upward and downward flow.

⁶As mentioned in Chapter 5, poloidal field components are in practice overwhelmingly real, indicating that they coincide azimuthally with the (real) driving. Toroidal components are overwhelmingly imaginary, which corresponds to an azimuthal offset.

- 885 This effect presumably arises because the current is a linear quantity while the Poynting
 886 flux is quadratic: the electric and magnetic fields that make it up oscillate in phase, so
 887 their product is positive even when they are negative.
- 888 At higher altitude, where the Hall conductivity is small, parallel current is associated
 889 only with the toroidal mode. Figure 6.4 shows data from the same runs as Figure 6.3,
 890 arranged in the same way, but the values are taken at an altitude of 1000 km instead of
 891 100 km.
- 892 In Figure 6.4, as in Figure 6.3, the imaginary component of the parallel current (third
 893 column) coincides more or less with the toroidal Poynting flux (fourth column). How-
 894 ever, the real component of the parallel current (first column) is vanishingly small, even
 895 when the poloidal Poynting flux (second column) is strong. **TODO: Is this expected?**
 896 **Tikhonchuk[95] looks specifically at the toroidal mode when considering shear Alfven**
 897 **waves. Does the poloidal mode count as compressional even when it's guided?**
- 898 The magnitude of the parallel current tops out over $1 \mu\text{A}/\text{m}^2$, just shy of the up-to-tens
 899 of $\mu\text{A}/\text{m}^2$ inferred from ground observations and seen in situ[9, 46, 82].

It's also possible to consider the effect of parallel currents and electric fields on the ionosphere's energy budget, per Poynting's theorem:

$$\frac{\partial}{\partial t} u = -\nabla \cdot \underline{E} - \underline{J} \cdot \underline{E} \quad (6.7)$$

- 900 As shown in Figure 6.5, little energy transfer in the ionosphere is mediated by perpen-
 901 dicular components of the Poynting flux. The parallel component of $\underline{J} \cdot \underline{E}$ is comparably
 902 unimportant. The energy deposited in the ionosphere by the Poynting flux matches
 903 closely with the energy lost to Joule dissipation — as it should, to conserve energy
 904 — but according to the model, parallel currents and electric fields do not contribute
 905 significantly.

Current and Poynting Flux at 1000km: Quiet Day , 16mHz Current

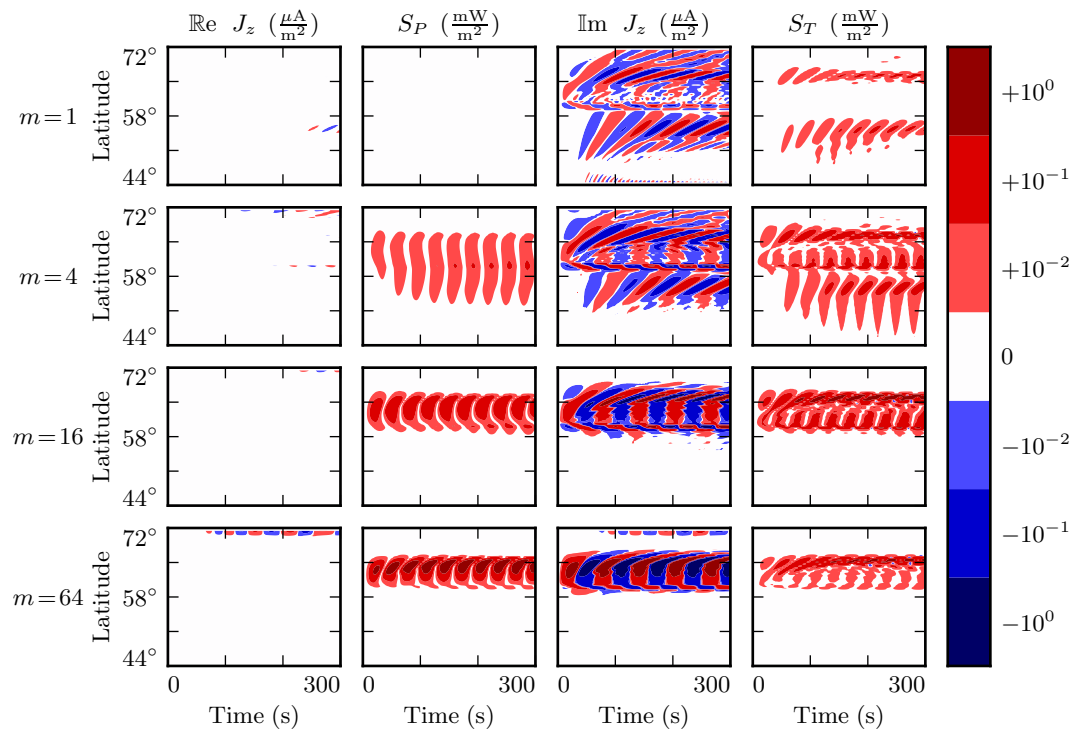


Figure 6.4: TODO: ...

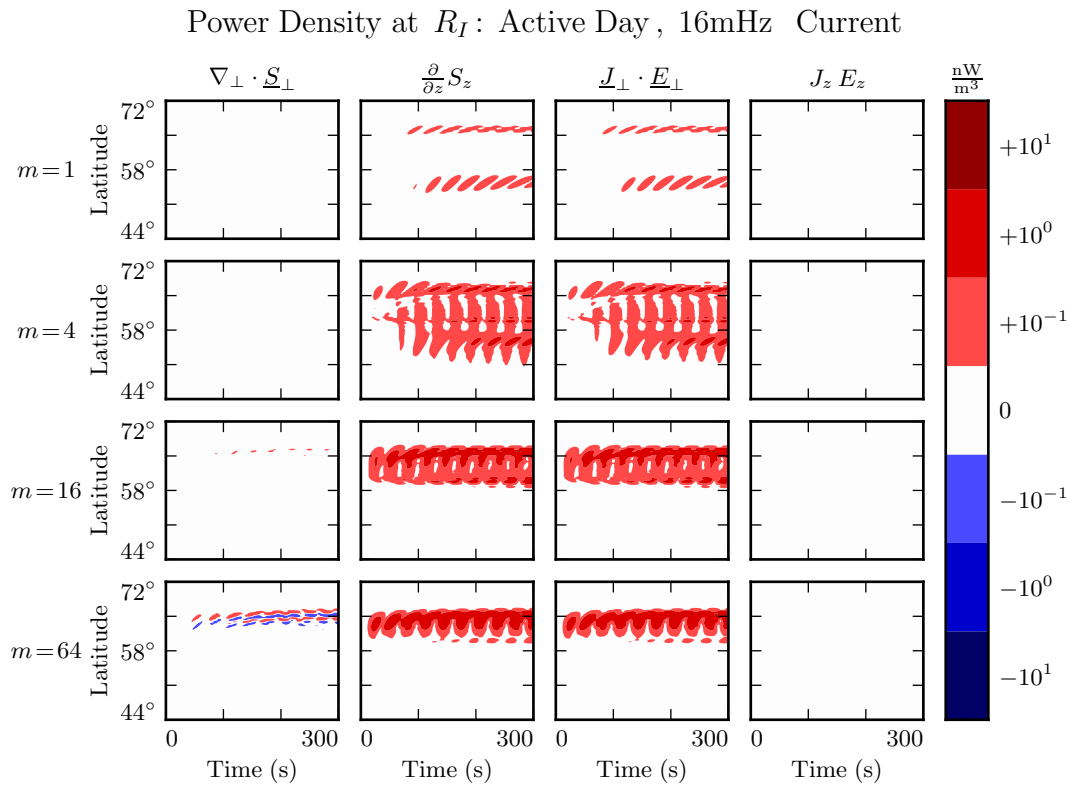


Figure 6.5: While field-aligned currents can be of significant size, they are not particularly good at depositing energy in the ionosphere. Energy deposited by the Poynting flux matches closely with Joule dissipation from the perpendicular currents, while $J_z E_z$ is smaller by several orders of magnitude.

906 6.3 Inertial Length Scales

907 It's not quite fair to compare the parallel and perpendicular contributions to $\nabla \times \underline{E}$ as
908 is done in Section 6.2. Perpendicular electric fields are on the order of 1 mV/m, with
909 wavelengths on the order of 10^5 km; they give rise to magnetic field gradients around
910 0.1 nT/s. Parallel electric fields, closer to 10^{-6} mV/m, would need to vary over length
911 scales of 0.1 km to match with that.

912 Such scales are believable. The characteristic length scale of the plasma oscillation is
913 the electron inertial length, $\frac{c}{\omega_p}$, which is on the order of 1 km in the auroral ionosphere
914 and 0.1 km in the low-altitude plasmasphere. However, Tuna's usual grid doesn't resolve
915 structures so fine; its resolution bottoms out closer to 10 km. That is, with the inclusion
916 of electron inertial effects, Tuna's grid is too coarse to resolve all of the waves expected
917 to be present. The model is prone to instability as a result.

918 Figure 6.6 shows a run with perpendicular resolution smaller than the electron inertial
919 length, side by side with an analogous run on the usual grid. In order to carry out
920 the inertial-scale run, several concessions were made to computational cost. The run
921 simulates only a duration of 100 s (other results in previous sections and in Chapter 7
922 show 300 s), and the grid covers only the auroral latitudes from $L = 5$ to $L = 7$.

923 Even so, the run presents a significant computational expense. Spread over 16 cores, a
924 100 s run on Tuna's usual grid takes well under an hour. The inertial-scale run barely
925 finished in 96 hours, the cutoff at the Minnesota Supercomputing Institute⁷.

926 The snapshot shown in Figure 6.6 uses a perpendicular grid resolution of 0.7 km at the
927 Earthward edge, which just satisfies the Nyquist rate for the minimum inertial length
928 of 1.7 km. It's still too coarse. There is clearly some small-scale structure developing in
929 the ionosphere, but it's not well resolved. The large number of "wiggles" portends an
930 imminent crash.

⁷Runtime goes as the inverse square of grid resolution. Not only does finer resolution require more grid cells, but it also gives rise to proportionally smaller crossing times, imposing a smaller time step.

Parallel Electric Fields: Quiet Day, 100s of 16mHz Current, $m = 16$

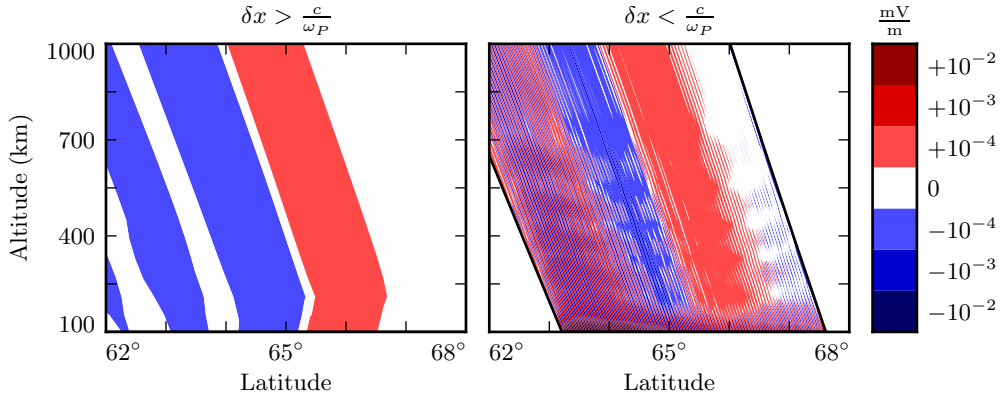


Figure 6.6: The parallel electric field develops significant structure when the perpendicular grid resolution is smaller than the electron inertial length. Unfortunately, such runs are prohibitively expensive. The lower panel — which still fails to resolve wave structure properly — represents a 100-fold increase in computational time.

931 6.4 Discussion

932 TODO: The dispersion relation in Chapter 4 suggests that parallel electric fields should
 933 be smaller than perpendicular electric fields by at least six orders of magnitude. Tuna
 934 agrees.

935 TODO: Tuna computes parallel currents a bit weaker than those that are observed —
 936 $\sim 1 \mu\text{A}/\text{m}^2$ rather than $\sim 10 \mu\text{A}/\text{m}^2$. The currents accompany the toroidal mode, but
 937 not the poloidal mode, except where the two are coupled by a strong Hall conductivity.
 938 Is this expected?

939 TODO: When inertial effects are not properly resolved, the code is prone to instability.
 940 Resolving inertial scales properly presents a prohibitive computational expense.

941 Electron inertial effects present a promising first-principles-based approach to the in-
 942 vestigation of parallel currents and electric fields associated with field line resonances.
 943 Unfortunately, because of the large differences in scale between Pc4 pulsations and the

944 plasma oscillation, the proper deployment of inertial effects presents a prohibitive com-
945 putational expense. Results shown in Chapter 7 make use of the core version of Tuna
946 presented in Chapter 5, which does not include the effects of electron inertia.

947 **Chapter 7**

948 **Numerical Results**

949 TODO: An overarching motivation for the present work is that FLRs exhibit significant
950 behavioral changes as a result of their azimuthal modenumber, but that prior models
951 have been unable to provide a good picture.

952 **7.1 Modenumber and Compression**

953 It's well known that the poloidal FLR mode is compressional at low modenumber,
954 but guided at high modenumber. However, the relationship is not well quantified.
955 Theoretical work has historically been concerned with the limits $m \rightarrow 0$ and $m \rightarrow$
956 ∞ [16, 78], and only a handful of satellite observations have explicitly considered an
957 event's azimuthal modenumber[19, 70, 90]. Using results from Tuna, the present section
958 examines the strength of the poloidal wave's compressional component at an ensemble
959 of finite modenumbers.

960 Figures 7.1 and 7.2 show magnetic field snapshots taken from a pair of runs. The first
961 uses a small azimuthal modenumber, and the second uses a large one. The runs are
962 otherwise identical: both simulations use the quiet dayside ionospheric profile, and both
963 are driven at 22 mHz.

964 The differences between the two runs are striking. At low modenumber, wave activity
965 is visible throughout the simulation domain. Structure in the poloidal magnetic field is
966 only vaguely governed by the dipole geometry, and the compressional magnetic field is
967 comparably strong to the two perpendicular components.

968 In contrast, at high modenumber, the poloidal magnetic field is localized to the L -shells
969 where the driving is delivered: $4 \lesssim L \lesssim 6$. The compressional field is weaker than
970 the poloidal field by at least an order of magnitude. A third-harmonic poloidal mode
971 is visible at the outer boundary — its magnitude is just barely large enough to be
972 visible on the logarithmic scale. The gap between $L \sim 5$ (where 22 mHz matches a first-
973 harmonic FLR) and $L \sim 10$ (where 22 mHz matches a third-harmonic FLR) speaks to
974 the evanescence of non-guided waves above the compressional Alfvén cutoff frequency¹.

975 In both the low- m and high- m runs, toroidal activity is more or less coincident with
976 poloidal activity — as is to be expected, since the driving is purely poloidal, and the
977 poloidal mode rotates to the toroidal mode over time. It is further notable that the
978 toroidal mode is sharply guided. Particularly in Figure 7.2, strong, narrow, toroidal
979 FLRs of opposite phase can be seen oscillating very close to one another. Strong poloidal
980 waves, in contrast, are smeared in L .

981 Snapshots are not shown for runs carried out using the other ionospheric profiles (active
982 day, quiet night, and active night). The morphology of their waves is qualitatively
983 similar. The differences between the profiles is considered in Sections 7.2 to 7.4.

984 Figure 7.3 quantifies the compressional component of the poloidal mode as a function of
985 modenumber. Each subplot corresponds to a different run of Tuna — the runs shown in
986 Figures 7.1 and 7.2 are in the rightmost column, second from the top and second from the
987 bottom respectively. The red line indicates the ratio between the RMS compressional
988 magnetic field and the RMS poloidal magnetic field; both averages are taken over the
989 entire simulation “volume” each time step. Mean values are shown in black.

¹See Section 4.4.

- 990 At $m = 1$, the compressional and poloidal magnetic fields are comparable in magnitude.
991 As m increases, however, the compressional component quickly falls off. The compres-
992 sional component is half the strength of the poloidal component at $m \sim 5$, and a quarter
993 by $m \sim 10$.
- 994 A slight frequency dependence is apparent across each row in Figure 7.3. Compressional
995 coupling falls off slower for waves at higher frequency. This is because higher-frequency
996 waves are that much closer to the cutoff frequency (described in Section 4.4), and so
997 their propagation across L -shells is that much less evanescent.
- 998 Similarly, poloidal waves are more prone to compression on the nightside. Due to the
999 higher Alfvén speed on the nightside, driving is delivered at $L \sim 6$ instead of $L \sim 5$. The
1000 cutoff frequency depends inversely on radial distance. For nightside runs (not shown),
1001 $\left| \frac{B_z}{B_x} \right|$ falls to 50% at $m \sim 8$ and to 25% at $m \sim 16$.
- 1002 Notably, the waves considered in the present work are fundamental harmonics. The
1003 compressional behavior of the poloidal mode may vary for the (more-common) second
1004 harmonic: Radoski suggests that the asymptotic value of $\left| \frac{B_z}{B_x} \right|$ is inversely proportional
1005 to the harmonic number[78].

Magnetic Field Snapshots: Quiet Day , 22mHz Current, $m = 2$

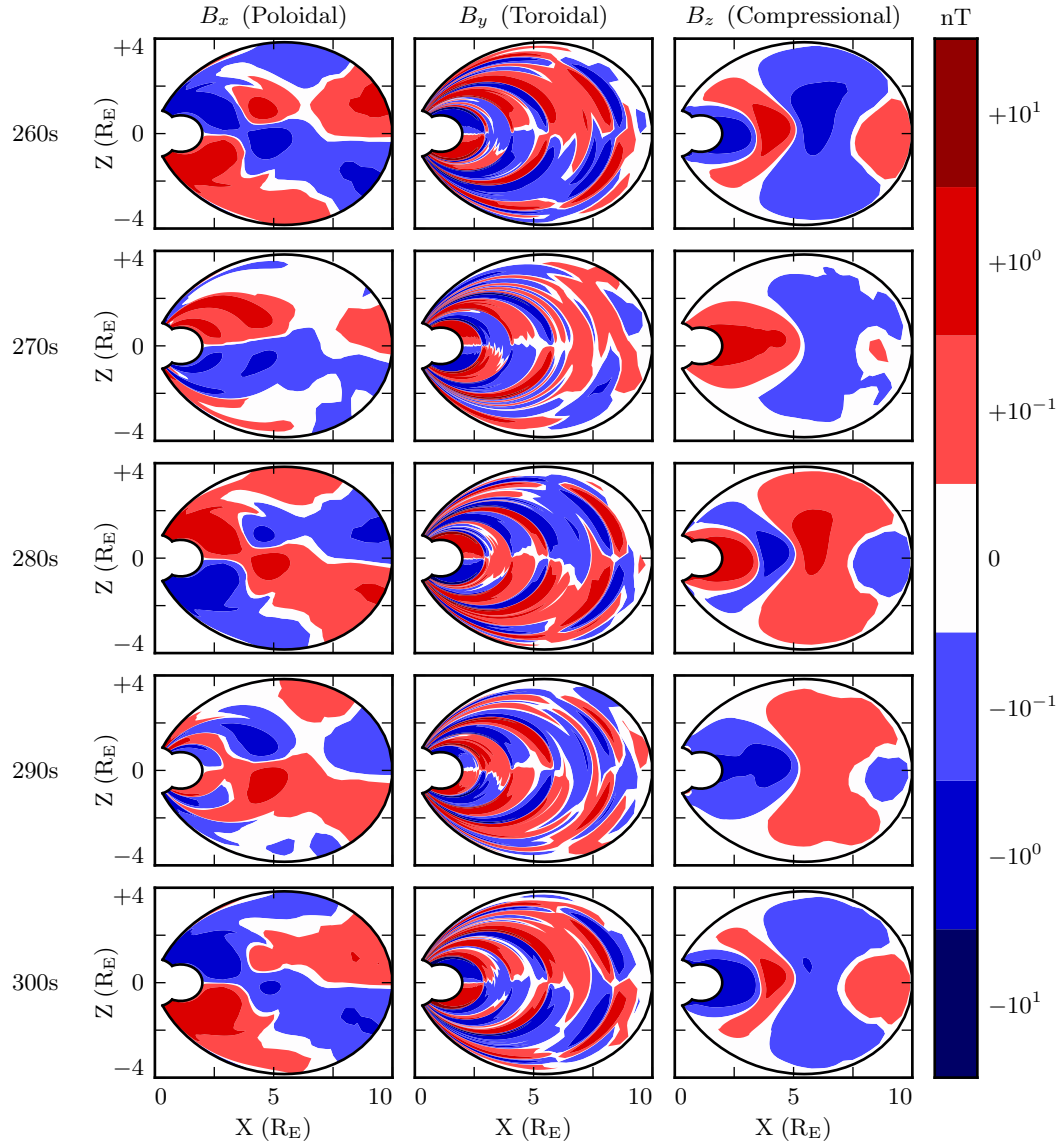


Figure 7.1: Each row in the above figure is a snapshot in time. The three columns show the simulated poloidal, toroidal, and compressional magnetic field. Due to the run's low azimuthal modenumber, the poloidal mode has a significant compressional component. This is visible both in the fact that B_z is comparable in size to B_x , and in that structure in B_x is only vaguely guided by the geometry of the magnetic field. Toroidal waves, in contrast, are sharply guided.

Magnetic Field Snapshots: Quiet Day , 22mHz Current, $m = 32$

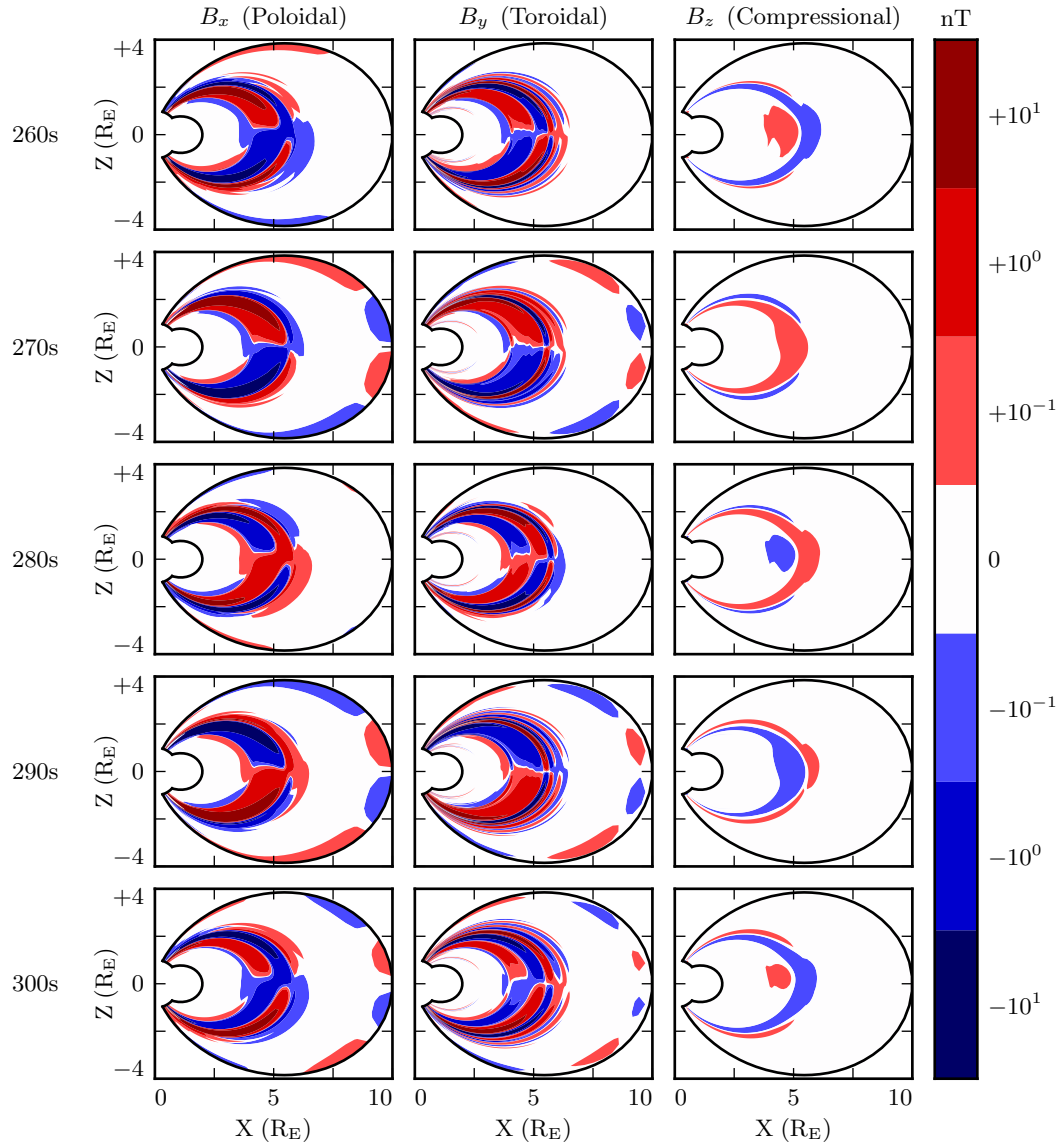


Figure 7.2: The above figure is analogous to Figure 7.1, but the runs use a larger azimuthal modenumber. The change has a dramatic effect. The poloidal wave is concentrated much more sharply in L , and its compressional component is weakener by an order of magnitude. Regardless of modenumber, toroidal waves exist at a range of L shells similar to poloidal waves, and show sharp definition across L -shells.

Compressional Coupling to the Poloidal Mode: Quiet Day

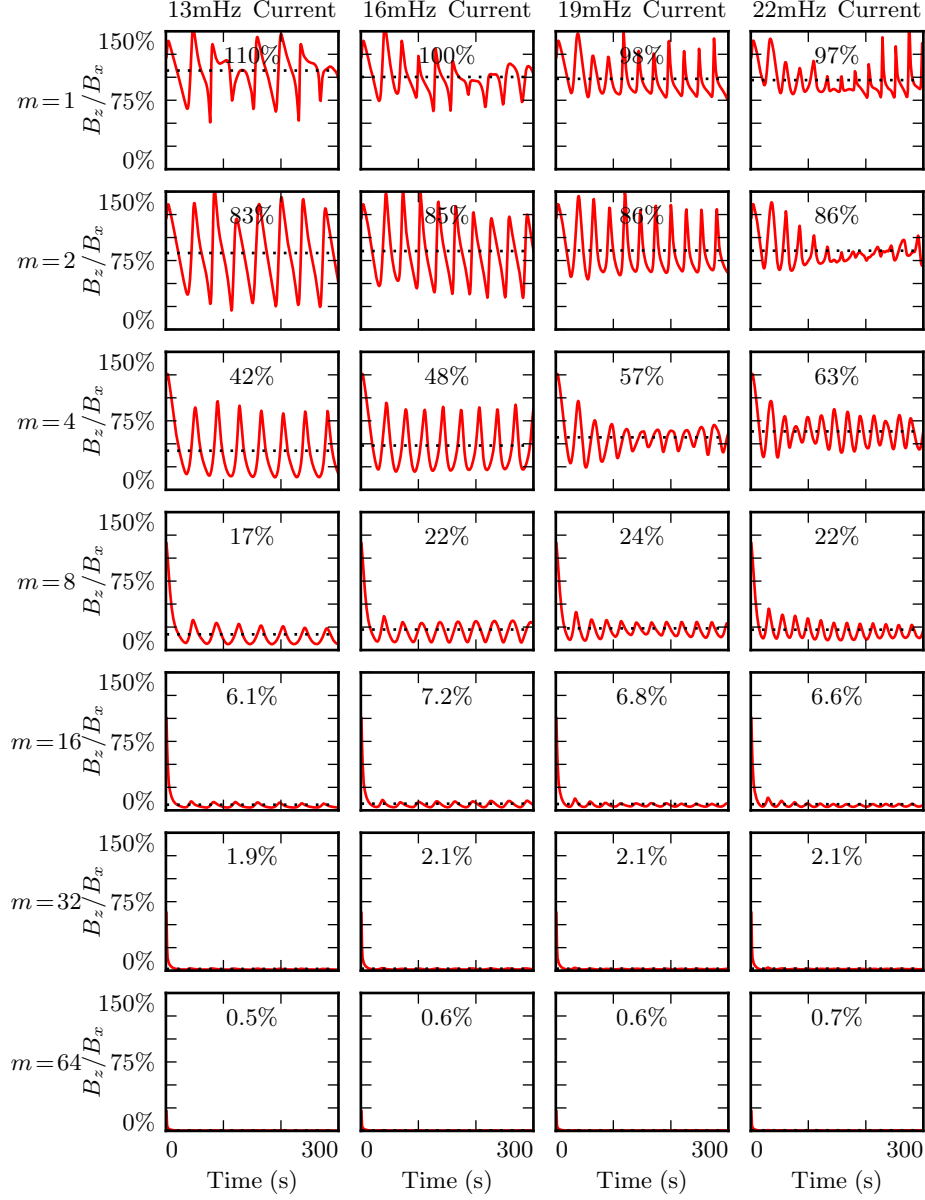


Figure 7.3: Each subplot above corresponds to a different run; the runs shown in Figures 7.1 and 7.2 are in the rightmost column, second from the top and second from the bottom respectively. Red lines indicate the ratio between the RMS compressional and poloidal magnetic fields. Mean values are shown in black. The compressional field is comparable to the poloidal field at $m = 1$, but falls quickly.

1006 **7.2 Resonance and Rotation on the Dayside**

1007 In his 1974 paper, Radoski argues that a poloidally-polarized wave should asymptotically
1008 rotate to the toroidal polarization[78] as a result of the curved derivative in the
1009 meridional plane. The question of finite poloidal lifetimes is considered further in a 1995
1010 paper by Mann and Wright[64]. Their numerical work used a straightened field line,
1011 with an Alfvén speed gradient in the “radial” direction. They also found a rotation over
1012 time from poloidal to toroidal polarization, with the characteristic time proportional to
1013 the azimuthal modenumber.

1014 The present section builds on the aforementioned results by relaxing several of their non-
1015 physical assumptions. Tuna’s geometry is more realistic than Radoski’s half-cylinder or
1016 the box model used by Mann and Wright. Previous work has considered the evolution
1017 of an initial condition, while the simulations shown below include driving delivered
1018 over time. In addition, Tuna features a finite, height-resolved ionospheric conductivity
1019 profile, rather than the perfectly-reflecting boundaries used in the past.

Each subplot in Figure 7.4 is analogous to Figure 3 in Mann and Wright’s paper[64]. Blue lines show the total energy in the poloidal mode as a function of time. Red lines show toroidal energy. Runs are organized analogous to those in Figure 7.3: drive frequency is constant down each column, and azimuthal modenumber is constant across each row. Axis bounds are held constant across all subplots. The poloidal and toroidal energy are computed by integrating over the electromagnetic energy density, per Poynting’s theorem:

$$U_P = \int \frac{dV}{2\mu_0} \left(B_x^2 + \frac{1}{v_A^2} E_y^2 \right) \quad U_T = \int \frac{dV}{2\mu_0} \left(B_y^2 + \frac{1}{v_A^2} E_x^2 \right) \quad (7.1)$$

1020 Where the differential volume dV is computed using the Jacobian² to account for Tuna’s
1021 unusual geometry. The integral is evaluated in u^1 and u^3 but not u^2 (Tuna’s missing
1022 half-dimension), which gives energy in units of gigajoule per radian. More than anything
1023 else, this serves as a reminder that Pc4 pulsations are localized in MLT.

²See Section 5.1.

1024 The 28 runs shown in Figure 7.4 use an ionospheric profile corresponding to the dayside
1025 during times of low solar activity, where the conductivity is relatively high. The active
1026 and quiet dayside profiles are briefly contrasted in Section 7.4; for the most part, the
1027 focus of the present work is on the difference between the dayside and the nightside
1028 (Section 7.3). Differences between the two dayside profiles are small in comparison.

1029 The fact that red (toroidal) lines appear at all in Figure 7.4 speaks to a net rotation
1030 of energy from the poloidal mode to the toroidal. As discussed in Section 5.3, Tuna’s
1031 driving is delivered purely into the poloidal electric field (reflecting a perturbation in
1032 the magnitude of the ring current).

1033 As expected, the rotation from poloidal to toroidal is slowest at large azimuthal mode-
1034 numbers. The toroidal energy overtakes the poloidal energy within a single drive period
1035 at $m = 4$; at $m = 64$, the most of the energy is in the poloidal mode for ~ 10 periods.
1036 However, the relationship between azimuthal modenumber and rotation timescale is
1037 not linear, as was suggested by Mann and Wright. Instead, in a practical setting, the
1038 rotation is fastest at $m \sim 4$.

1039 This is explained by the compressional character of the poloidal mode. At very low
1040 modenumber, energy in the poloidal mode moves readily across L -shells. A significant
1041 fraction of that energy is lost to the outer boundary before rotating to the toroidal
1042 mode. At high modenumber — as discussed in Section 7.1 — compressional propagation
1043 is evanescent, so all energy in the poloidal mode must ultimately rotate to the toroidal
1044 mode or be lost to Joule dissipation.

1045 Joule dissipation is a major player in the system’s energy economy. However, due to the
1046 highly conductive dayside ionosphere, dissipation timescales are in the tens of Pc4 wave
1047 periods. Energy loss through Joule dissipation asymptotically balances energy input
1048 from driving, but most of that energy is not lost until after it has rotated from the
1049 poloidal mode to the toroidal. As such, in most runs shown in Figure 7.4, the energy
1050 content of the toroidal mode asymptotically exceeds that of the poloidal mode.

1051 The asymptotic energy content of the system also depends on how well the drive fre-
1052 quency matches the local eigenfrequency. If the two do not match, energy is lost to
1053 destructive interference between the standing wave and the driving.

1054 In principle, energy moves between the poloidal and toroidal modes due to their direct
1055 coupling through the ionospheric Hall conductivity. In practice, this effect is small.
1056 When the runs shown in Figure 7.4 are repeated with the Hall conductivity set to zero,
1057 the resulting energy curves are not visibly different.

1058 The low- m runs at 19 mHz merit additional discussion. These runs accumulate energy
1059 over a large number of wave periods, while the low- m waves at 13 mHz, 16 mHz, and
1060 22 mHz do not. This effect is likely nonphysical. At 19 mHz, a third-harmonic resonance
1061 forms very close to the outer boundary. The resonance is likely enhanced by nonphysical
1062 reflections against the simulation’s boundary conditions.

1063 The presence of individual harmonics can be seen in the contours shown in Figures 7.5
1064 and 7.6. These figures show the same runs as Figure 7.4, arranged in the same way on
1065 the page. However, instead of showing the total energy integrated over the simulation
1066 domain, the energy densities are averaged over the volume of each flux tube individually.
1067 Figure 7.5 shows contours of poloidal energy density and Figure 7.6 shows toroidal
1068 energy density.

1069 The top few rows of Figure 7.5 confirm that the poloidal mode’s compressional nature is
1070 to blame for its failure to accumulate energy at low modenumber. Waves move so readily
1071 across field lines that no visible amount of energy builds up at $L \sim 5$, the location of the
1072 driving. Some energy moves inward, and is trapped by the peak in Alfvén speed just
1073 inside the plasmapause, while the rest moves to the outer boundary. The time spent
1074 moving across field lines counts against the poloidal mode’s finite lifetime, inhibiting
1075 the buildup of poloidal energy density even at L -shells where the wave matches the local
1076 eigenfrequency.

1077 As m increases, the energy distribution becomes more concentrated in L , though indi-
1078 vidual features remain fairly broad. At $m = 8$, runs at 13 mHz and 16 mHz are inclined
1079 to build up energy just inside the plasmapause, while those at 19 mHz and 22 mHz res-
1080 onate just outside the plasmapause; in all four cases, the energy is spread over a range
1081 of at least 1 in L .

1082 The peak energy density in the bottom-right run (22 mHz driving, $m = 64$) is by far the
1083 largest of any run in Figure 7.5. The azimuthal modenumber is large, so the poloidal

1084 mode is purely guided; energy is not smeared across multiple L -shells. And, crucially, the
1085 frequency of the driving matches closely with the Alfvén frequency at $L \sim 5$. Other runs
1086 on the bottom row are also guided, but they reach lower asymptotic energy densities
1087 because of a mismatch between the drive frequency and the local eigenfrequency —
1088 resulting in destructive interference between the standing wave and its driver.

1089 The eigenfrequencies in the magnetosphere are significantly affected by the location of
1090 the plasmapause. When the runs in Figure 7.5 are repeated with the plasmapause at
1091 $L = 5$ instead of $L = 4$, the strongest resonance at $L \sim 5$ drops from 22 mHz to 16 mHz
1092 (not shown).

1093 Whereas the poloidal contours are smeared over a swath of L -shells (though the high- m
1094 runs less so), the toroidal contours in Figure 7.6 appear only where the wave frequency
1095 matches the local eigenfrequency. A horizontal line drawn through the Alfvén speed
1096 frequency profiles (recall Figure 3.1) intersects the profile up to three times: once as
1097 the Alfvén frequency drops through the Pc4 range from its low-latitude peak, again as
1098 the Alfvén frequency rises sharply at the plasmapause, and a third time as the Alfvén
1099 frequency drops asymptotically. Toroidal waves can be seen resonating at all three of
1100 these locations in the $m = 4$, 22 mHz run in Figure 7.6, along with a third harmonic at
1101 large L . This is consistent with observations: toroidal resonances are noted for having
1102 frequencies which depend strongly on L , in contrast to the poloidal mode's less-strict
1103 relationship between frequency and location.

1104 In only one of the runs shown in Figure 7.5 does the poloidal mode attain an energy
1105 density on the order of 10^{-1} nJ/m³. On the other hand, the toroidal mode reaches
1106 $\sim 10^{-1}$ nJ/m³ in six of the runs in Figure 7.6. That is, the poloidal mode only exhibits
1107 a high energy density on the dayside only when conditions are ideal; the toroidal mode
1108 isn't nearly so particular.

Poloidal (Blue) and Toroidal (Red) Energy: Quiet Day

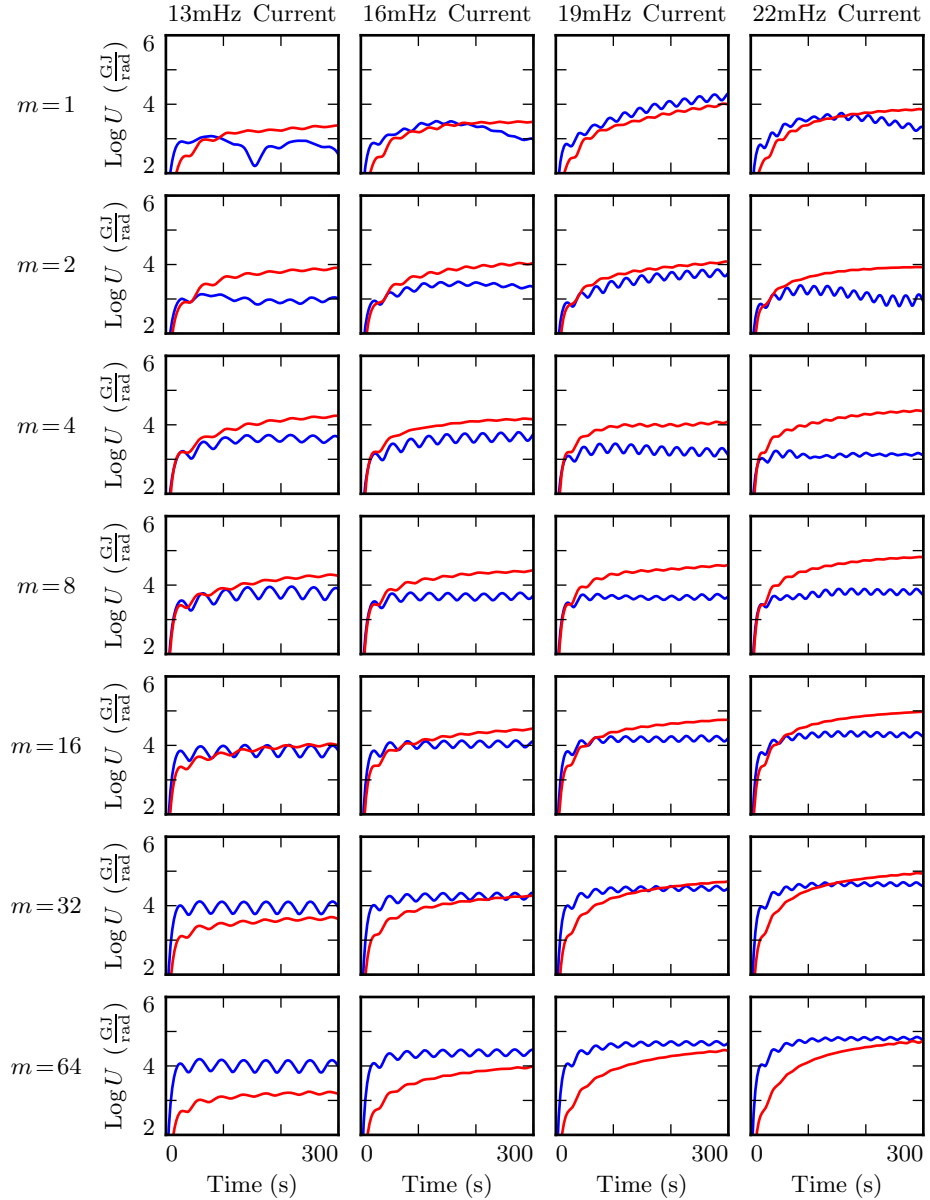


Figure 7.4: TODO: Lorem ipsum dolor sit amet, consectetur adipiscing elit, sed do eiusmod tempor incididunt ut labore et dolore magna aliqua. Ut enim ad minim veniam, quis nostrud exercitation ullamco laboris nisi ut aliquip ex ea commodo consequat. Duis aute irure dolor in reprehenderit in voluptate velit esse cillum dolore eu fugiat nulla pariatur.

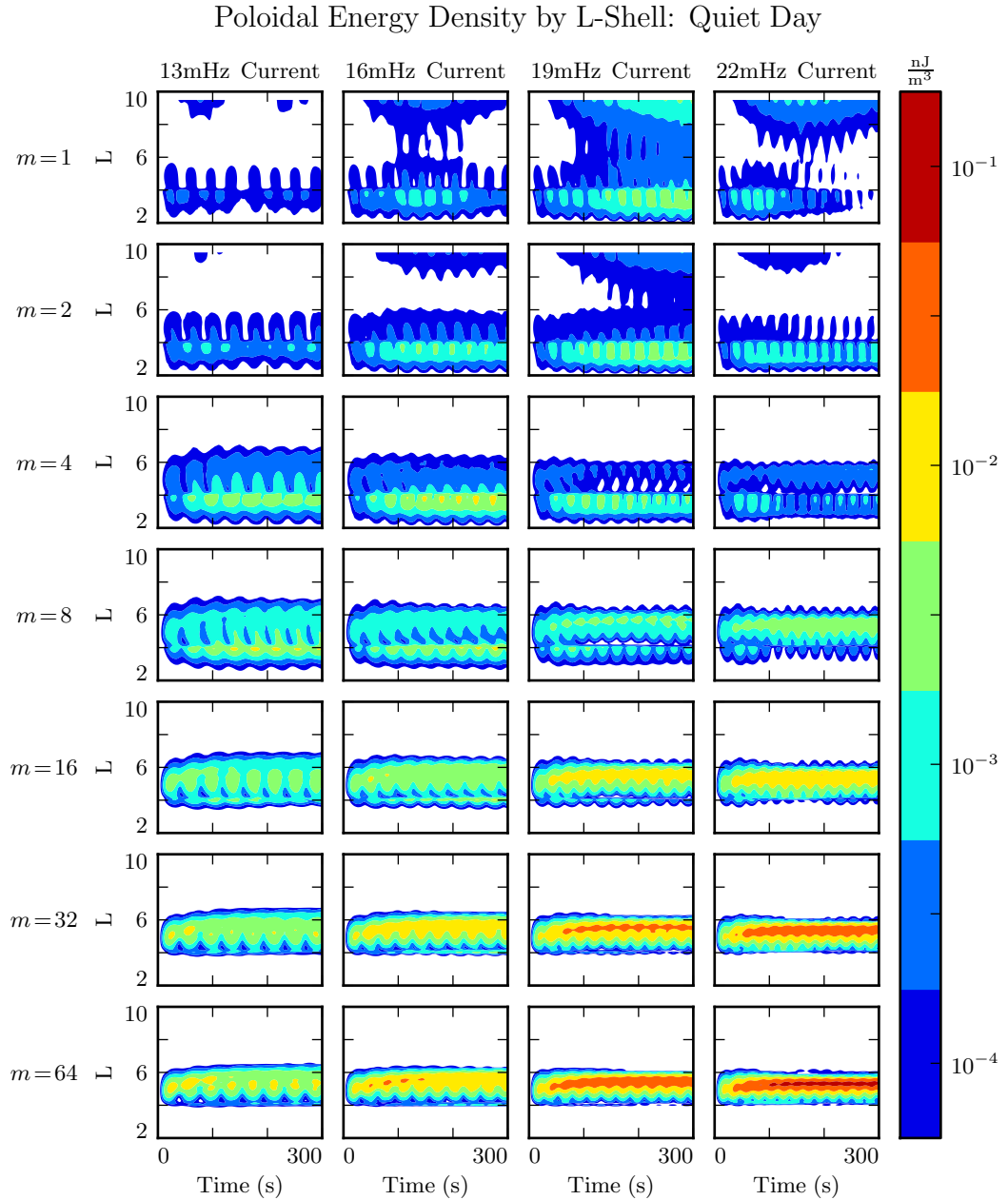


Figure 7.5: TODO: Lorem ipsum dolor sit amet, consectetur adipiscing elit, sed do eiusmod tempor incididunt ut labore et dolore magna aliqua. Ut enim ad minim veniam, quis nostrud exercitation ullamco laboris nisi ut aliquip ex ea commodo consequat. Duis aute irure dolor in reprehenderit in voluptate velit esse cillum dolore eu fugiat nulla pariatur.

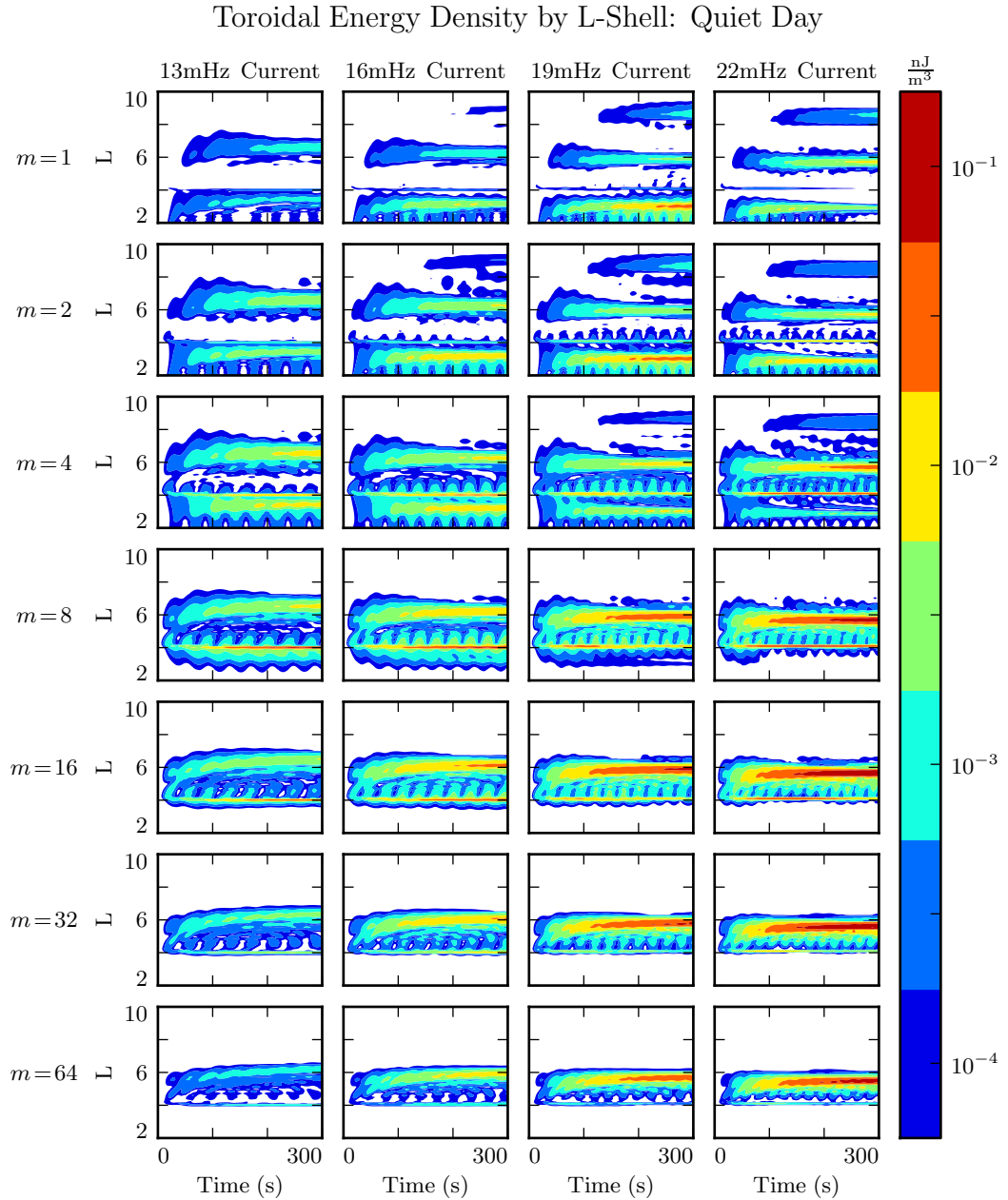


Figure 7.6: TODO: Lorem ipsum dolor sit amet, consectetur adipiscing elit, sed do eiusmod tempor incididunt ut labore et dolore magna aliqua. Ut enim ad minim veniam, quis nostrud exercitation ullamco laboris nisi ut aliquip ex ea commodo consequat. Duis aute irure dolor in reprehenderit in voluptate velit esse cillum dolore eu fugiat nulla pariatur.

1109 **7.3 Resonance and Rotation on the Nightside**

1110 **TODO: ACTUALLY** we should show the runs driven at $L \sim 5$ across the board. Dayside
1111 and nightside. That way we can make a fair comparison.

1112 Compared to the dayside ionosphere employed in Section 7.2, the nightside exhibits
1113 two major differences. The ionospheric conductivity is lower, and the Alfvén speed is
1114 higher. As a result of the higher Alfvén speed, driving on the nightside is delivered at
1115 $L \sim 6$ instead of $L \sim 5$. Runs in the present section specifically use Tuna’s ionospheric
1116 profile corresponding to the nightside during quiet solar conditions; the active nightside
1117 is discussed briefly in Section 7.4, but for the most part the present work is concerned
1118 with the behavior of the nightside compared to that on the dayside.

1119 Other than the change in ionospheric profile, Figures 7.7 to 7.9 are analogous to Fig-
1120 ures 7.4 to 7.6. Each subplot corresponds to a different 300 s run of Tuna. Drive
1121 frequency is constant down each column, and azimuthal modenumber is constant across
1122 each row.

1123 The low conductivity on the nightside gives rise to strong Joule dissipation. Waves are
1124 damped out in just a few bounces, so asymptotic energy values are reached quickly.
1125 No combination of frequency and modenumber gives rise to the accumulation of energy
1126 over multiple drive periods.

1127 As on the dayside, rotation of energy from the poloidal to toroidal mode is fastest at
1128 $m \sim 4$. Unlike the dayside, however, dissipation on the nightside is fast compared to
1129 the rotation of energy to the toroidal mode. Toroidal energy does not asymptotically
1130 exceed the poloidal energy by a significant margin in any run. At $m = 64$, where the
1131 rotation timescale is slowest, no more than **TODO: ...** of the energy in the poloidal
1132 mode rotates to the toroidal mode before being lost.

1133 **TODO:** The damping on the quiet nightside is so severe that basically nothing resonates
1134 anywhere. Should we show the active nightside instead?

Poloidal (Blue) and Toroidal (Red) Energy: Quiet Night

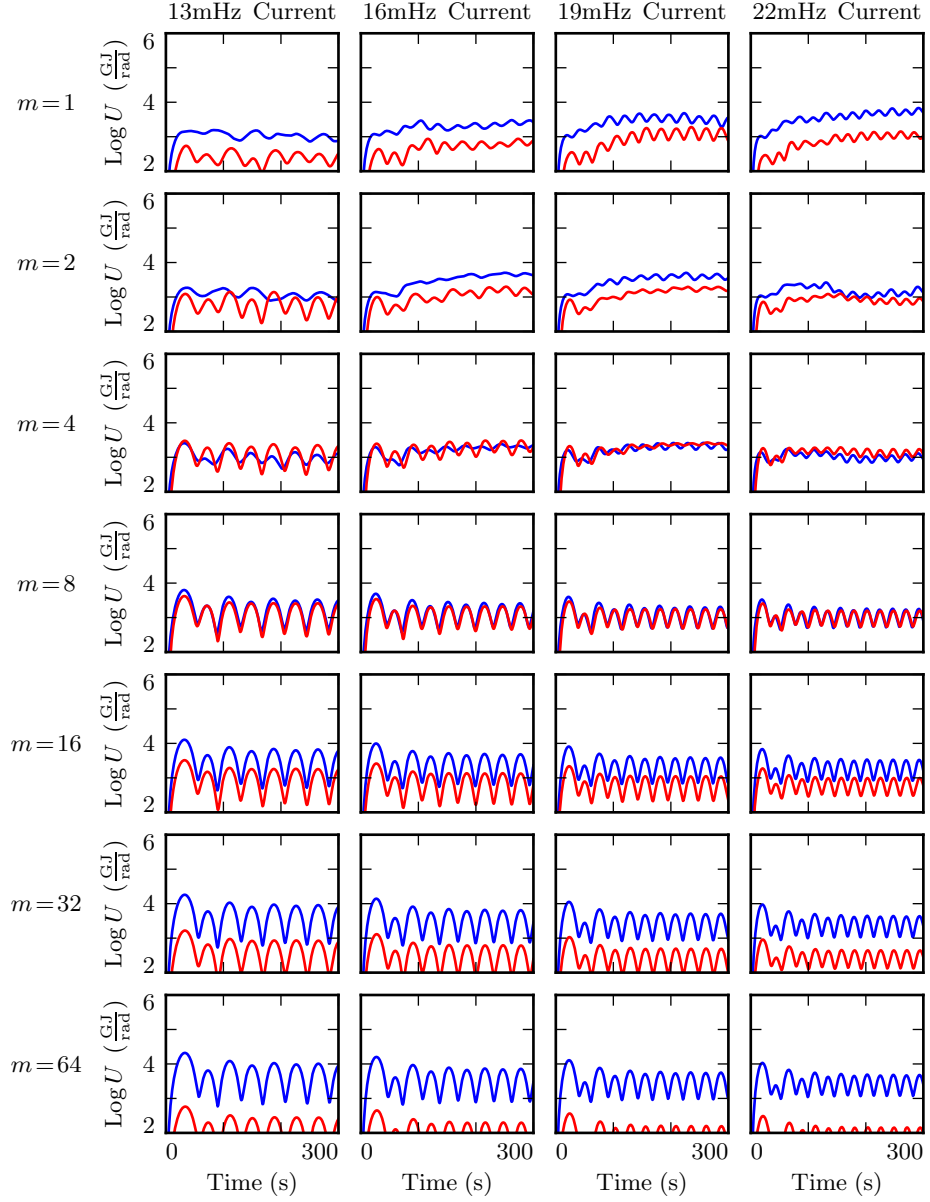


Figure 7.7: TODO: Lorem ipsum dolor sit amet, consectetur adipiscing elit, sed do eiusmod tempor incididunt ut labore et dolore magna aliqua. Ut enim ad minim veniam, quis nostrud exercitation ullamco laboris nisi ut aliquip ex ea commodo consequat. Duis aute irure dolor in reprehenderit in voluptate velit esse cillum dolore eu fugiat nulla pariatur.

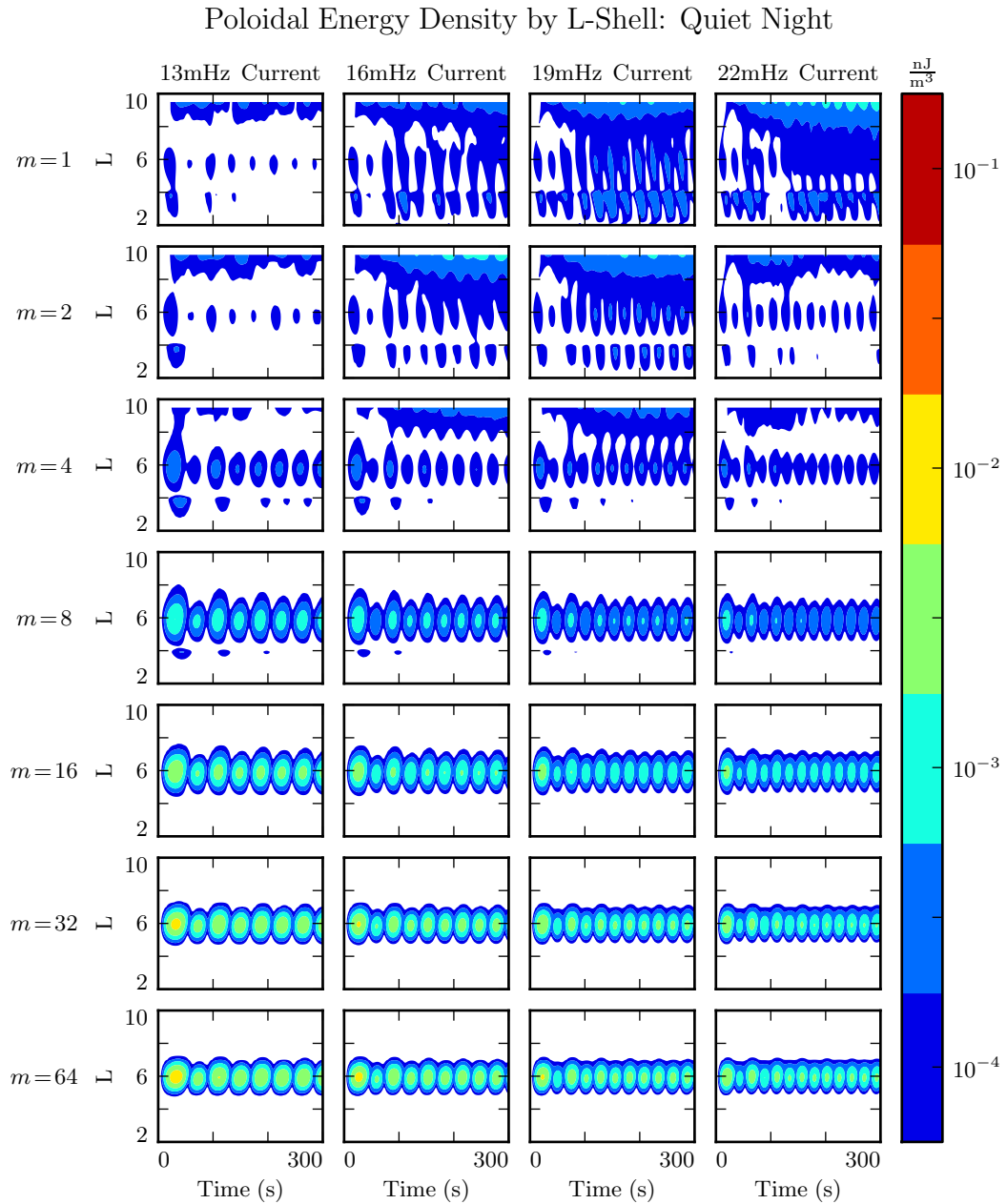


Figure 7.8: TODO: Lorem ipsum dolor sit amet, consectetur adipiscing elit, sed do eiusmod tempor incididunt ut labore et dolore magna aliqua. Ut enim ad minim veniam, quis nostrud exercitation ullamco laboris nisi ut aliquip ex ea commodo consequat. Duis aute irure dolor in reprehenderit in voluptate velit esse cillum dolore eu fugiat nulla pariatur.

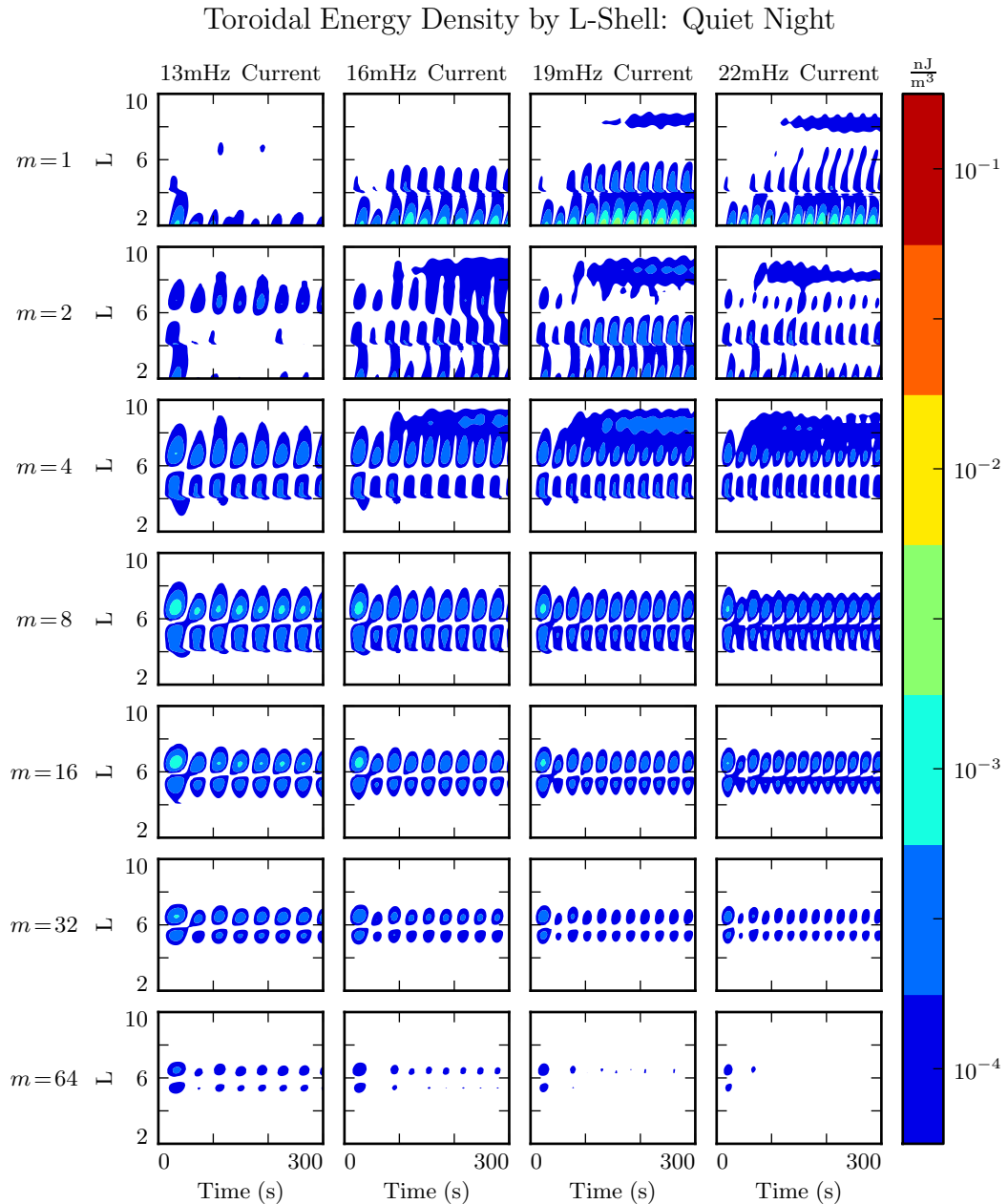


Figure 7.9: TODO: Lorem ipsum dolor sit amet, consectetur adipiscing elit, sed do eiusmod tempor incididunt ut labore et dolore magna aliqua. Ut enim ad minim veniam, quis nostrud exercitation ullamco laboris nisi ut aliquip ex ea commodo consequat. Duis aute irure dolor in reprehenderit in voluptate velit esse cillum dolore eu fugiat nulla pariatur.

1135 **7.4 Ground Signatures and Giant Pulsations**

1136 While the majority of the action is in space, the majority of FLR observations have
1137 historically been ground-based. The present section explores the same simulations dis-
1138 cussed in Sections 7.2 and 7.3, but in terms of their ground signatures rather than their
1139 broad energy distributions.

1140 As in the figures shown in Sections 7.2 and 7.3, each row in Figures 7.10 and 7.11 shows
1141 runs at a different modenumber. The columns are magnetic field contours; the vertical
1142 axis is latitude, and the horizontal axis is time. The four columns are components of
1143 the magnetic field signatures at the ground: the north-south magnetic field (first and
1144 third columns) and the east-west magnetic field (second and fourth columns). The pair
1145 on the left show a simulation carried out using the active ionospheric profile, and the
1146 pair on the right show a simulation using the quiet profile.

1147 Notably, the magnetic polarization of a low frequency Alfvén wave is rotated by $\sim 90^\circ$ as
1148 it passes through the ionosphere[41]. The east-west field on the ground (B_ϕ) corresponds
1149 to the poloidal polarization in space, and the north-south field on the ground (B_θ)
1150 corresponds to the toroidal mode.

1151 The most striking feature of Figures 7.10 and 7.11 is the modenumber dependence.
1152 As modenumber increases, the magnetic field signatures become sharply localized in
1153 latitude. At high m , ground signatures are concentrated between 60° and 70° , peaking
1154 near 64° on the dayside and 66° on the nightside. Appropriately enough, these latitudes
1155 lie at the $L \sim 5$ and $L \sim 6$ respectively.

1156 **TODO: Is it weird that we see no ducting from the ionosphere? Does the ionosphere**
1157 **duct ULF waves in the θ direction, or just in ϕ ?**

1158 At low modenumber, magnetic signatures are weak on the ground because the waves
1159 in space are also weak. At high modenumber, waves in space are strong, but so is
1160 the attenuation of magnetic signatures by the ionosphere³. The “sweet spot” at which
1161 magnetic ground signatures are maximized falls at $m = 16$ to $m = 32$.

3See Equation (3.3).

1162 Tuna shows stronger ground signatures on the dayside than on the nightside, more or
1163 less in proportion with the difference in magnitude in space. Energy on the dayside
1164 (which depends on field magnitude squared) peaks an order of magnitude larger than
1165 that on the nightside. Peak ground signatures on the dayside are larger by a factor of
1166 five: 45 nT compared to 10 nT. On both the dayside and the nightside, peak ground
1167 signatures are in B_ϕ , the east-west magnetic field component; both are also at $m = 16$,
1168 and both are seen in runs using the ionospheric profile for quiet solar activity.

1169 **TODO:** Check the other frequencies to make sure these are the real maxima. Probably
1170 also should print the maximum magnitude at the bottom of the subplot.

1171 These results match well with observations of giant pulsations, which tend to be east-
1172 west polarized, and are most often observed near 66° , with azimuthal modenumbers
1173 of 16 to 35, at the bottom of the solar cycle[93]. Pgs are most commonly observed
1174 pre-dawn, but dawn and dusk ionospheric profiles are not implemented for Tuna at
1175 present.

Dayside Magnetic Ground Signatures: 22mHz Current

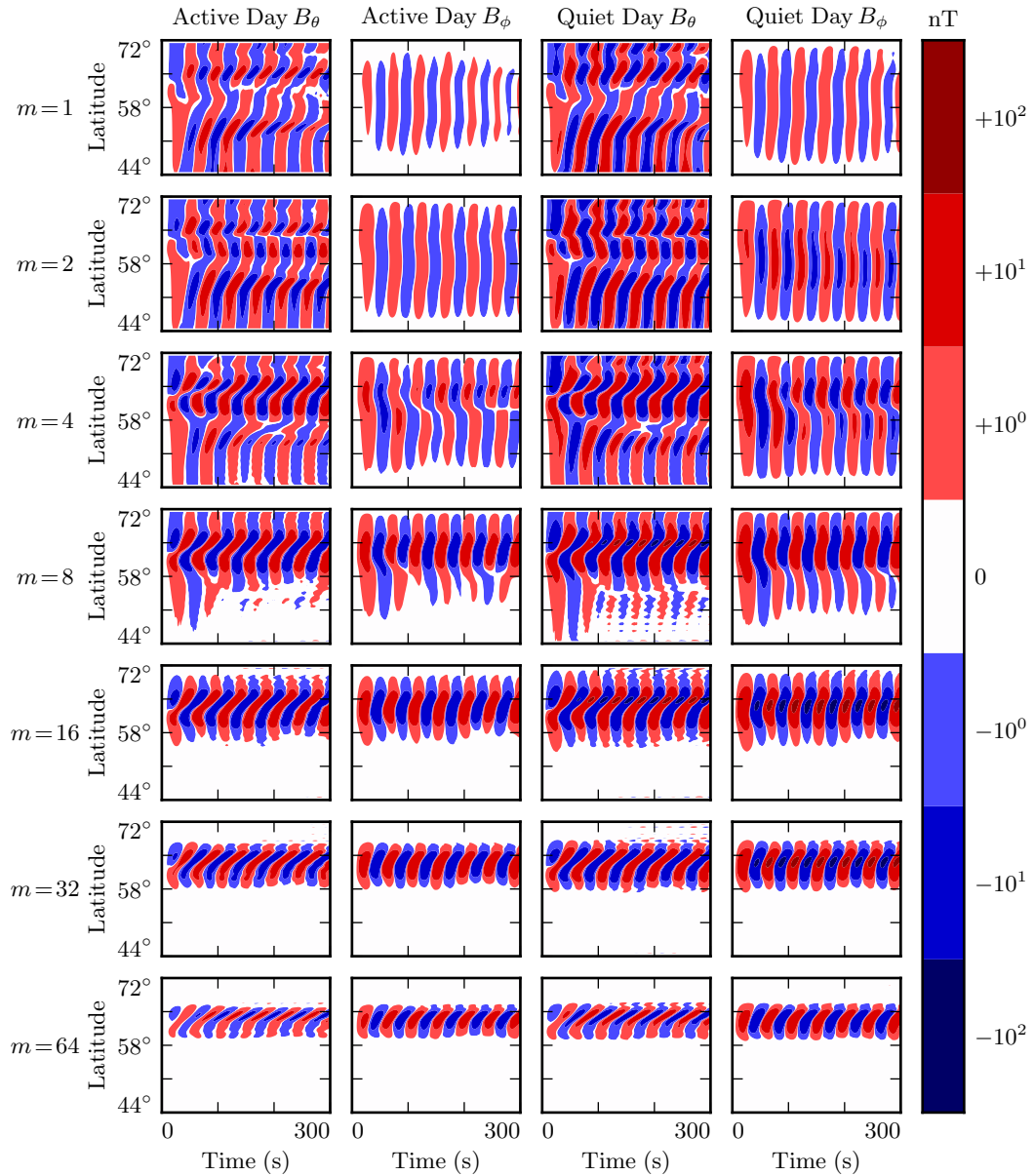


Figure 7.10: TODO: Lorem ipsum dolor sit amet, consectetur adipiscing elit, sed do eiusmod tempor incididunt ut labore et dolore magna aliqua. Ut enim ad minim veniam, quis nostrud exercitation ullamco laboris nisi ut aliquip ex ea commodo consequat. Duis aute irure dolor in reprehenderit in voluptate velit esse cillum dolore eu fugiat nulla pariatur.

Nightside Magnetic Ground Signatures: 13mHz Current

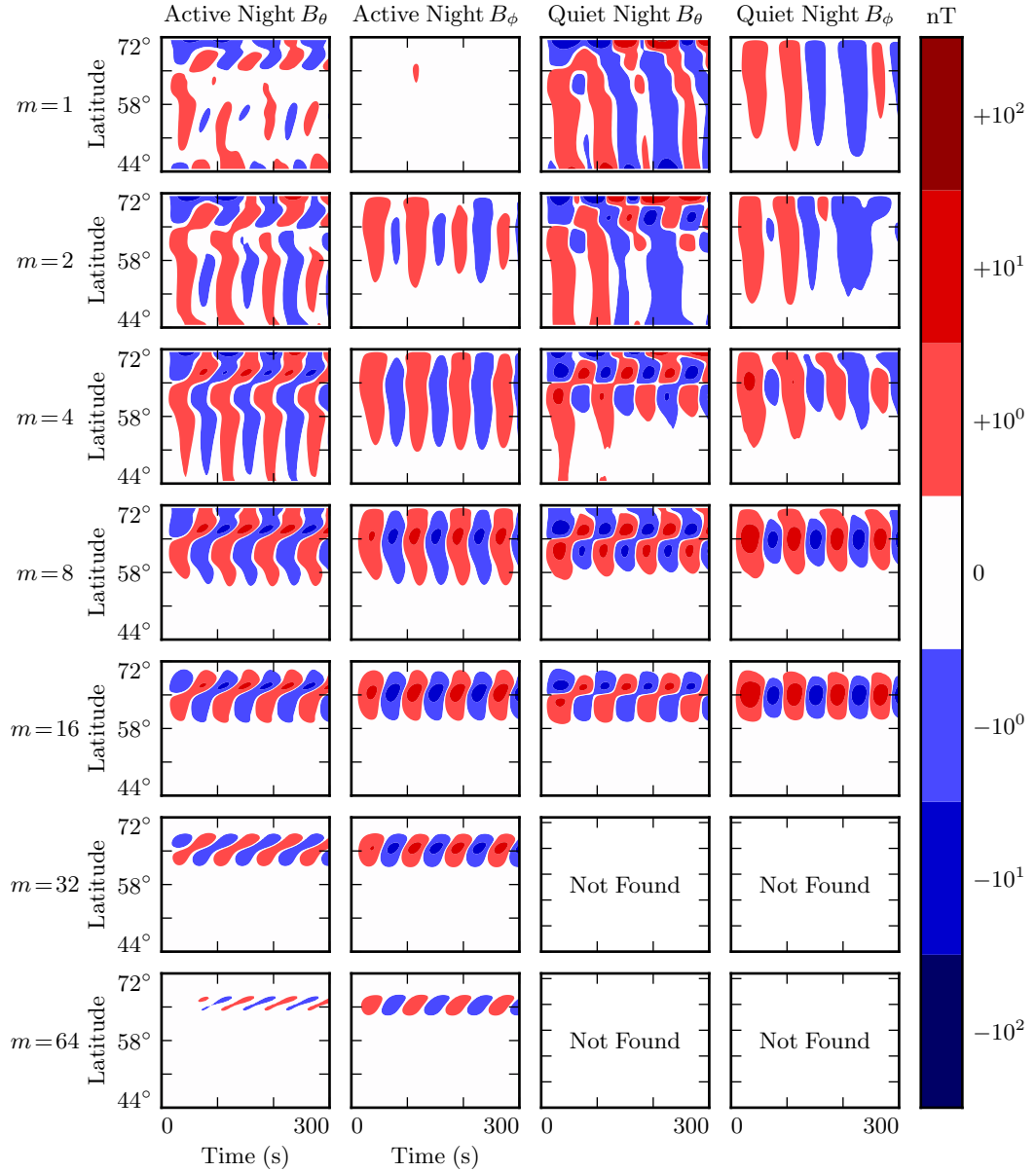


Figure 7.11: Nightside ground signatures are less strongly peaked than those on the dayside, but qualitative features are the same: the strongest signals are in B_ϕ , peaked over just a few degrees in latitude, at a modenumber of 16 or 32, under quiet ionospheric conditions.

1176 **7.5 Discussion**

1177 **TODO:** Make this section read nicely.

- 1178 Poloidal FLRs rotate to the toroidal mode over time. Toroidal modes do not appear to
1179 rotate back to the poloidal mode. When m is small, the rotation is comparable to an
1180 oscillation period; when m is large, rotation timescales are comparable to ten periods,
1181 sometimes more.
- 1182 On the dayside, little damping takes place over rotation timescales, so the toroidal mode
1183 asymptotically exceeds the toroidal mode. The exception is waves with low modenumber,
1184 where poloidal waves can escape by propagating across field lines. An evaluation
1185 of what happens then — whether they bounce back off the magnetopause, for example
1186 — is beyond the scope of the present work.
- 1187 On the nightside, the conductivity of the ionosphere is low enough that damping
1188 timescales become comparable to oscillation timescales. Waves are weaker, since they
1189 are unable to accumulate energy over as many periods. High- m toroidal waves are
1190 particularly weak, since the dissipation timescale is faster than the poloidal-to-toroidal
1191 rotation timescale.
- 1192 Waves resonate best when the frequency of the driving matches the local eigenfrequency
1193 where it's delivered. The eigenfrequency is significantly affected by the size of the
1194 plasmasphere.
- 1195 The poloidal mode, due to its compressional character, exhibits an energy profile which
1196 is smeared in L . The toroidal mode, on the other hand, forms sharp resonances where the
1197 drive frequency matches the local eigenfrequency. This may explain why the observed
1198 frequencies of poloidal waves depend weakly on L , while the frequencies of toroidal
1199 waves are strongly dependent on L .
- 1200 At low m , ground signatures are weak because waves in space are weak because energy
1201 can easily escape through the simulation's outer boundary. At large m , ground signatures
1202 are attenuated by the ionosphere. The “sweet spot” in azimuthal modenumber at
1203 which ground signatures are strongest is around 16 to 32. Furthermore, ground signatures
1204 are strongest when ionospheric profiles corresponding to solar minimum are used.

1205 Driving in the poloidal electric field gives rise to primarily ground signatures polarized
1206 primarily in the east-west direction at the ground. And, when the frequency of the
1207 driving does not match the local eigenfrequency, the high- m resonates weakly in place,
1208 rather than tunneling across field lines to resonate strongly somewhere else.

1209 These findings imply, awkwardly, that the morphology of giant pulsations may reveal
1210 relatively little about their origins. One can consider a hypothetical magnetosphere
1211 subject to constant driving: broadband in frequency, broadband in modenumber, just
1212 outside the plasmapause. Low- m poloidal waves will quickly rotate to the toroidal mode
1213 (and/or propagate away). High- m waves will resonate in place, accumulating energy
1214 over time, and giving rise to “multiharmonic toroidal waves”[89]; Fourier components
1215 that do not match the local eigenfrequency will quickly asymptote. Waves with very high
1216 modenumbers will be attenuated by the ionosphere. The response on the ground will be
1217 significantly stronger during quiet solar conditions. In other words, the measurements
1218 on the ground will look very much like a giant pulsation.

1219 **TODO:** Notably, the present work offers no explanation as to Pgs’ distinctive distribu-
1220 tion in MLT!

₁₂₂₁ **Chapter 8**

₁₂₂₂ **Van Allen Probe Observations**

₁₂₂₃ The results presented in Chapter 7 are perhaps interesting on their own, but become
₁₂₂₄ particularly valuable when combined with observational data. Unfortunately, only a
₁₂₂₅ small number of studies to date have explored how Pc4 observation rate is affected by
₁₂₂₆ the harmonic and polarization structure of those waves.

₁₂₂₇ While Pc4 pulsations have previously been studied in terms of both harmonic[5, 16, 27,
₁₂₂₈ 44, 83, 92] and polarization[3, 18, 19, 52, 56], little work has considered both at the
₁₂₂₉ same time. This has largely been due to observational constraints. The classification of
₁₂₃₀ a wave’s harmonic is best carried out by computing the phase offset of the magnetic and
₁₂₃₁ electric field waveforms, simultaneous in situ measurements of which have only recently
₁₂₃₂ become available as part of the THEMIS[4] and Van Allen Probe[86] missions. The
₁₂₃₃ Van Allen Probes (launched in 2012) are particularly well-suited to the study of Pc4
₁₂₃₄ pulsations as their apogee of $L \sim 6$ coincides closely with eigenfrequencies in the Pc4
₁₂₃₅ range.

₁₂₃₆ The present chapter uses data from the Van Allen Probes’ EFW instrument[103] to
₁₂₃₇ survey the occurrence rate of FLRs in the Pc4 range as a function of harmonic parity
₁₂₃₈ and polarization, as well as magnitude, frequency, and phase. The tools used to perform
₁₂₃₉ the present analysis — SPEDAS and the SPICE kernel — are publicly available. They,
₁₂₄₀ along with the Python routines used to download, filter, and plot the data, can be found
₁₂₄₁ in a Git repository at <https://github.com/chizarlicious/RBSP>.

1242 TODO: Set this up, along with Tuna, at https://github.com/chizarlicious/UMN_Space-Physics.

1244 8.1 Sampling Bias and Event Selection

1245 The present analysis makes use of Van Allen Probe data from October 2012 to August
1246 2015 — the entire range available at the time of writing. Between the two probes, that's
1247 just over 2000 days of observation.

1248 For the purposes of Pc4 pulsations, it's reasonable to consider the two probes to be
1249 independent observers. Nearly all Pc4 events occur near apogee ($L \gtrsim 5$), at which
1250 point the two probes are several hours apart in MLT. Pc4 events are typically not large
1251 enough to be seen by both probes simultaneously, and not long enough in duration to
1252 be seen by two probes passing through the same region of space several hours apart.

1253 TODO: Quantify how often an event is seen by both probes?

1254 Electric and magnetic field waveforms are collected using the probes' EFW and EMFISIS
1255 instruments respectively. Values are cleaned up by averaging over the ten-second spin
1256 period. Three-dimensional electric field data is then obtained using the $\underline{E} \cdot \underline{B} = 0$
1257 assumption. Notably, this assumption is taken only when the probe's spin plane is
1258 offset from the magnetic field by at least 15° . The rest of the data — about half — is
1259 discarded, which introduces a sampling bias against the flanks.

1260 A further bias is introduced by the probes' non-integer number of precessions around
1261 Earth. As of July 2014, apogee had precessed once around Earth[18]. The present work
1262 considers roughly one and a half precessions; the nightside has been sampled at apogee
1263 twice as often as the dayside.

1264 The spatial distribution of usable data — that is, data for which three-dimensional
1265 electric and magnetic fields are available — is shown in Figure 8.1. Bins are unitary in
1266 L and in MLT. Distribution in magnetic latitude is not shown; the Van Allen Probes
1267 are localized to within $\sim 10^\circ$ of the equatorial plane.

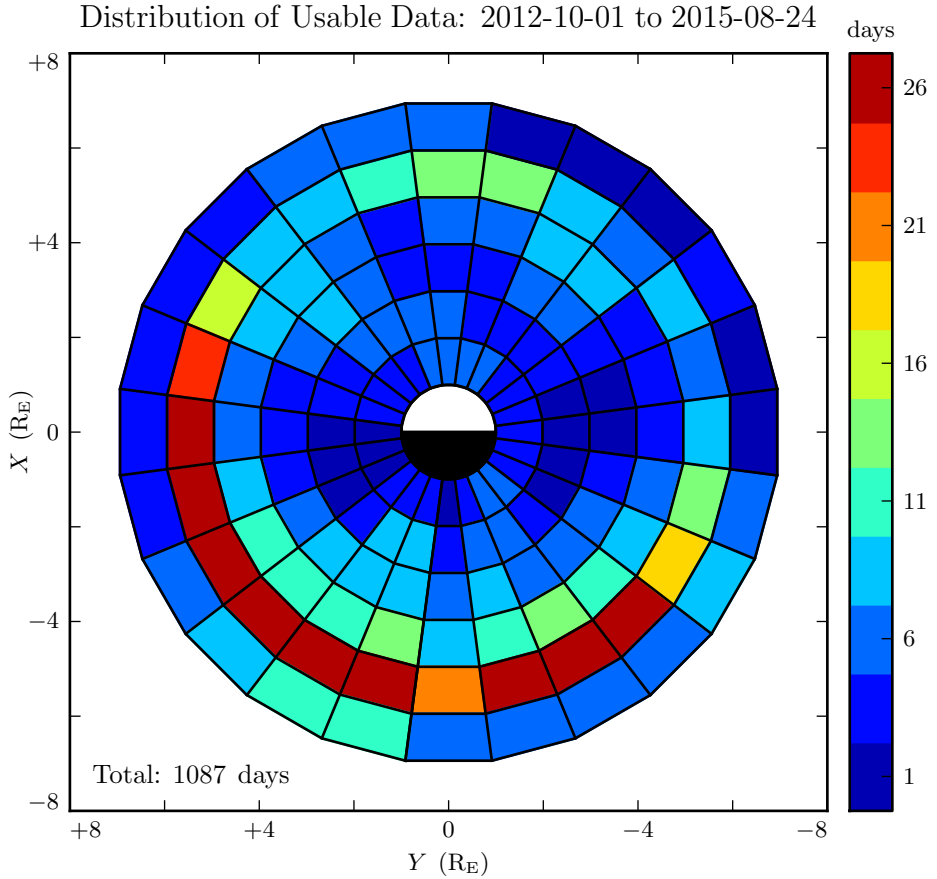


Figure 8.1: Three-dimensional electric field values are computed by assuming $\underline{E} \cdot \underline{B} = 0$. Data is discarded whenever the magnetic field falls within 15° of the spin plane, which introduces a bias against the flanks. Furthermore, the probes have completed one and a half precessions around Earth; the dayside has been sampled once at apogee, and the nightside twice.

1268 Field measurements are transformed from GSE coordinates into the same dipole coordi-
 1269 nates used in Chapters 5 and 7. The z axis (parallel to the background magnetic field)
 1270 is estimated using a ten-minute running average of the magnetic field measurements.
 1271 The y axis is set parallel to $\hat{z} \times \underline{r}$, where \underline{r} is the probe's geocentric position vector.
 1272 The x axis is then defined per $\hat{x} \equiv \hat{y} \times \hat{z}$. This scheme guarantees that the axes are
 1273 right-handed and pairwise orthogonal[56].

1274 The \sim 1000 days of usable data are considered half an hour at a time, which gives a fre-
 1275 quency resolution of \sim 0.5 mHz in the discrete Fourier transform. Spectra are computed
 1276 for all six field components: \tilde{B}_x , \tilde{B}_y , \tilde{B}_z , \tilde{E}_x , \tilde{E}_y , and \tilde{E}_z . The background magnetic
 1277 field is subtracted before transforming the magnetic field components, leaving only the
 1278 perturbation along each axis¹. Each waveform is also shifted vertically so that its mean
 1279 over the thirty minute event is zero.

Frequency-domain Poynting flux is computed from the electric and magnetic field transforms. A factor of L^3 compensates the compression of the flux tube, so that the resulting values are effective at the ionosphere. Poloidal and toroidal Poynting flux, respectively, are given by:

$$\tilde{S}_P \equiv -\frac{L^3}{\mu_0} \tilde{E}_y \tilde{B}_x^* \quad \tilde{S}_T \equiv \frac{L^3}{\mu_0} \tilde{E}_x \tilde{B}_y^* \quad (8.1)$$

1280 The poloidal and toroidal channels are independently checked for Pc4 waves. For each
 1281 channel, a Gaussian profile is fit to the magnitude of the Poynting flux, $|\tilde{S}(\omega)|$. If the
 1282 fit fails to converge, or if the peak of the Gaussian does not fall within 5 mHz of the
 1283 peak value of \tilde{S} , the event is discarded. Events are also discarded if their frequencies
 1284 fall outside the Pc4 frequency range (7 mHz to 25 mHz) or if their amplitudes fall below
 1285 10^{-2} mW/m² (out of consideration for instrument sensitivity).

1286 Events are discarded if their parity is ambiguous. The electric field and the magnetic
 1287 field must be coherent at a level of 0.9 or better (judged at the discrete Fourier transform
 1288 point closest to the peak of the Gaussian fit). Any event within 3° of the magnetic
 1289 equator is also not used; as discussed in Chapter 3, in order to distinguish an odd mode
 1290 from an even mode, it's necessary to know whether the observation is made north or
 1291 south of the equator.

1292 **TODO:** How much time do the probes spend within 3° of the magnetic equator?

1293 A visual inspection of events shows that those with broad “peaks” in their spectra
 1294 are typically not peaked at all — they are noisy spectra with several spectral features
 1295 grouped just closely enough to trick the fitting routine. A threshold is set at a FWHM

¹As in Chapters 5 and 7, B_x , refers not to the full magnetic field in the x direction, but to the perturbation in the x direction from the zeroth-order magnetic field. The same is true for B_y and B_z .

1296 of 3 mHz (equally, a standard deviation of 1.27 mHz). Any event with a Gaussian fit
1297 broader than that is discarded.

1298 Notably, events are not filtered on their phase — that is, on the division of their energy
1299 between standing and traveling waves. This is the topic of Section 8.5.

1300 **TODO:** Are we biased in terms of DST? What's the distribution look like for the good
1301 data and for the bad data?

1302 8.2 Events by Mode

1303 The filters described in Section 8.1 yield 762 Pc4 events, the spatial distribution of
1304 which is shown in Figure 8.2. In each bin, the event count is normalized to the amount
1305 of usable data, per Figure 8.1. Bins shown in white contain zero events. The rate in
1306 the bottom corner is an overall mean, weighing each bin equally.

1307 **TODO:** Bins should be weighted by L . The small inner bins count too much right now,
1308 and are dragging down the average.

1309 Consistent with previous work, Pc4 events peak on the dayside and are rarely observed
1310 at $L < 4$. Nearly 30 % of the usable data shown in Figure 8.1 is taken at $L < 4$, yet
1311 only 16 of the 762 events appear there.

1312 On the other hand, the present work runs contrary to Dai's 2015 result in terms of Pc4
1313 event rates with respect to the plasmapause (not shown). His analysis found (poloidal)
1314 Pc4 pulsations to be comparably common inside and outside the plasmapause[18]. In
1315 the present work, only 40 of the 762 events (5 %) fall inside the plasmasphere, despite
1316 the fact that 40 % of the available data falls within the plasmasphere. The disparity is
1317 not likely due to a difference in sampling — Dai's work, like the present work, uses data
1318 from the Van Allen Probes mission. Rather, the difference is likely due to disagreement
1319 in how the plasmapause is defined. Dai identifies the plasmapause by the maximum
1320 gradient in electron number density, while the present work takes an electron density of
1321 100 /cm³ to mark the plasmapause².

²Per ongoing work by Thaller.

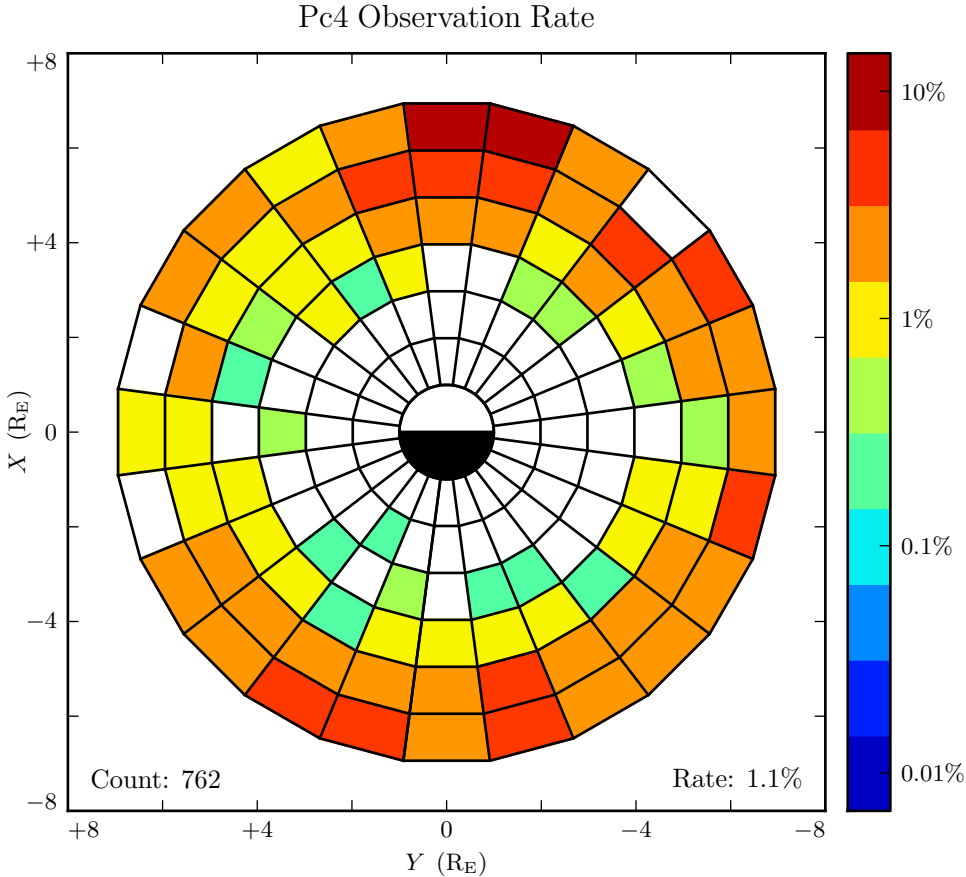


Figure 8.2: The above figure shows the spatial distribution of all 762 observed Pc4 events. Counts are normalized by the amount of usable data in each bin. The value in the bottom-right corner is the mean of the rate in each bin; it's an estimate of how often Pc4 events would be observed if the sampling were distributed uniformly in space. Events where the poloidal and toroidal channel trigger simultaneously ($\sim 10\%$ of cases) are counted as only a single event. Bins shown in white contain zero events.

1322 In Figure 8.3, events are partitioned by parity and polarization, yielding 124 odd poloidal
 1323 events, 214 even poloidal events, 415 odd toroidal events, and 83 even toroidal events
 1324 — a total of 836 events. The total is greater than 762 because in $\sim 10\%$ of events, the
 1325 poloidal and toroidal channels trigger independently. Such cases are marked as a single
 1326 event in Figure 8.2, but the toroidal and poloidal events are both shown in Figure 8.3.

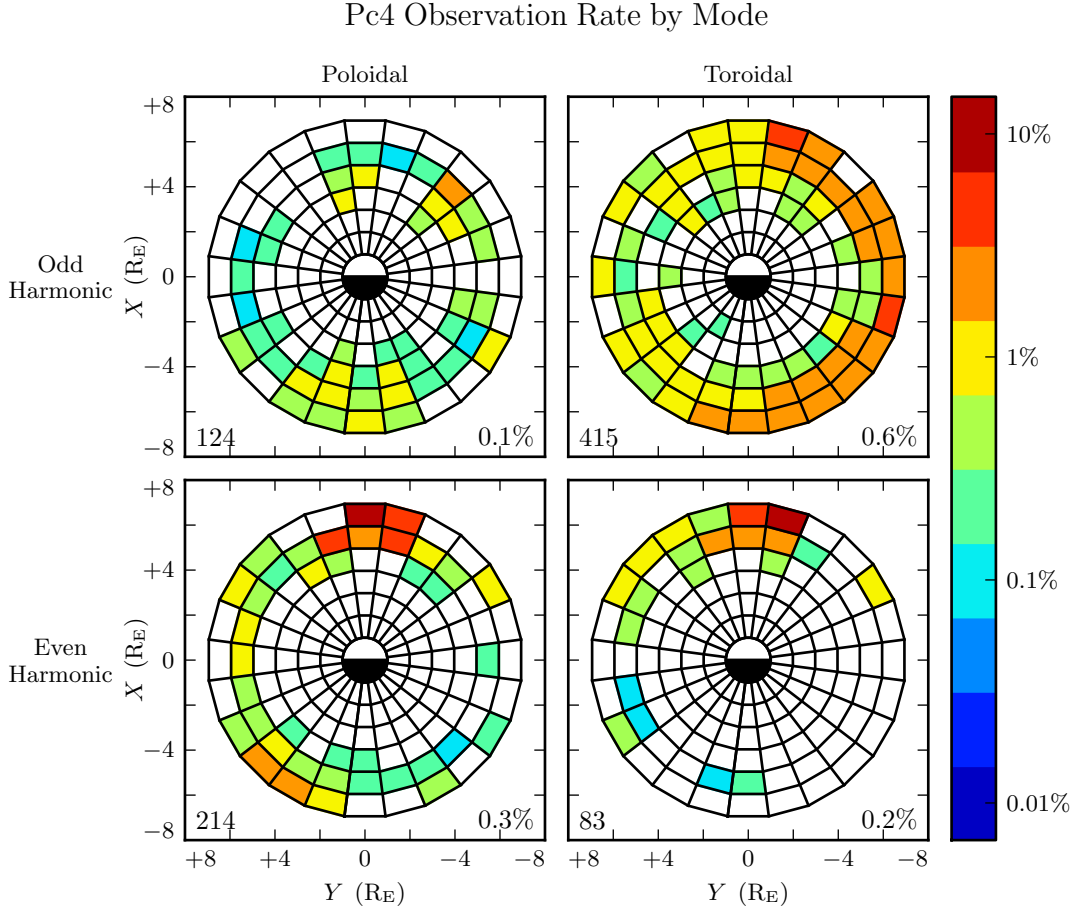


Figure 8.3: The above figure shows the spatial distribution for the same 762 events shown in Figure 8.2, partitioned by polarization and parity. The selection criteria described in Section 8.1 ensure that both properties are known for all events. Event counts are normalized by the time spent by the amount of usable data in each bin. Counts shown in the bottom-left corners do not sum to 762 because some events trigger on both the poloidal channel and the toroidal channel. Bins shown in white contain zero events.

1327 Double-triggering can be taken as a vague proxy for event quality. When the channels
 1328 both trigger independently, the two events almost always (71 of 74 events) exhibit the
 1329 same parity. This suggests a poloidal wave with sufficient power, and a sufficient narrow
 1330 spectral peak, that it can still be seen after much of its energy has rotated to the toroidal
 1331 mode.

1332 TODO: Show plot of double-triggering events.

1333 Odd double-triggering events are spread broadly in MLT. They rarely occur twice on the
1334 same day (23 events spread over 20 days), are observed at comparable rates regardless
1335 of DST.

1336 Even-harmonic double-triggering events, on the other hand, are mostly seen near noon,
1337 and are significantly more common when $DST < -30$ nT. Even events are also more
1338 concentrated than odd ones. The 48 even-harmonic double-events are spread over 20
1339 days, and 35 of them are spread over just 7 days. This clustering — where the poloidal
1340 and toroidal channel both trigger for five to ten half-hour events in the same day — is
1341 prevalent regardless of DST.

1342 The distribution of even poloidal events in Figure 8.3 is consistent with that reported
1343 by Dai[18]: the observation rate is peaked at noon, and smeared across the dusk side.
1344 Notably, Dai’s work focused on even poloidal waves. While he did not explicitly remove
1345 odd events from his sample, he did introduce a threshold in the magnetic field. This
1346 threshold is preferentially satisfied by even waves (which have a magnetic field antinode
1347 near the equator) compared to odd waves (which have a magnetic field node). Dai
1348 characterized the parity of only a quarter of his events; among those, he found even
1349 harmonics to outnumber odd harmonics ten-to-one.

1350 In fact — to the degree that they can be straightforwardly compared — the distributions
1351 in Figure 8.3 also show agreement with work by Anderson[3] (using AMPTE/CCE),
1352 Kokubun[52] (using ATS6), Liu[56] (using THEMIS), and Motoba[70] (using GOES).
1353 Toroidal events dominate overall, and are primarily seen on the morning side. Poloidal
1354 events are spread broadly in MLT, with a peak near noon and distinctive odd harmonics
1355 in the early morning.

1356 Crucially, the present work can offer insight into how previous results fit together. Unlike
1357 events considered in previous works, those shown in Figure 8.3 have all been categorized
1358 in terms of both polarization and parity. And, perhaps more importantly, the selection
1359 process has not introduced a bias with respect to polarization or parity (at least not an
1360 obvious one).

1361 Not only does Figure 8.3 show that toroidal events outnumber poloidal events, but it
1362 also shows that toroidal events are predominantly odd harmonics — as opposed to the
1363 primarily-even poloidal events. This may suggest that odd poloidal waves are more
1364 likely than even ones to be driven at low modenumber (allowing a prompt rotation of
1365 that energy to the toroidal mode). One might expect low- m poloidal modes to be driven
1366 by a broad, sudden change in solar wind dynamic pressure, for instance. The relative
1367 scarcity of odd poloidal observations on the dayside may indicate a short-lived source.
1368 At low m , energy rotates to the toroidal mode on the order of a wave period; without
1369 an ongoing source, there would be no poloidal wave to observe.

1370 This would furthermore be consistent with even modes' apparent dearth of ground
1371 signatures[93]. If even harmonics tend to be produced at higher modenumber than odd
1372 ones, even harmonics would be expected to produce ground signatures less often³.

1373 Even poloidal modes and even toroidal modes exhibit similar distributions in space:
1374 both are peaked at noon and smeared across the dusk flank, with little activity on the
1375 dawn side. This is further support for the even poloidal wave as a significant source for
1376 the even toroidal mode.

1377 TODO: People have talked about this. Is there a conventional explanation for dawn-dusk asymmetry?

1379 TODO: What else do we want to say here? Or does the rest of the commentary belong
1380 in the later sections? Note that plots in future sections are lower resolution, to make
1381 sure that the number of bins remains much smaller than the number of events.

1382 TODO: How does this relate to the numerical results in Chapter 7?

1383 8.3 Events by Amplitude

1384 One might reasonable be concerned that the spatial distributions presented in Figure 8.3
1385 are dominated by these small events, while Pc4 events large enough to be noteworthy

³See Equation (3.3).

1386 follow a different distribution entirely. The goal of the present section is to address that
 1387 concern.

Amplitude Distribution of Pc4 Events by Mode

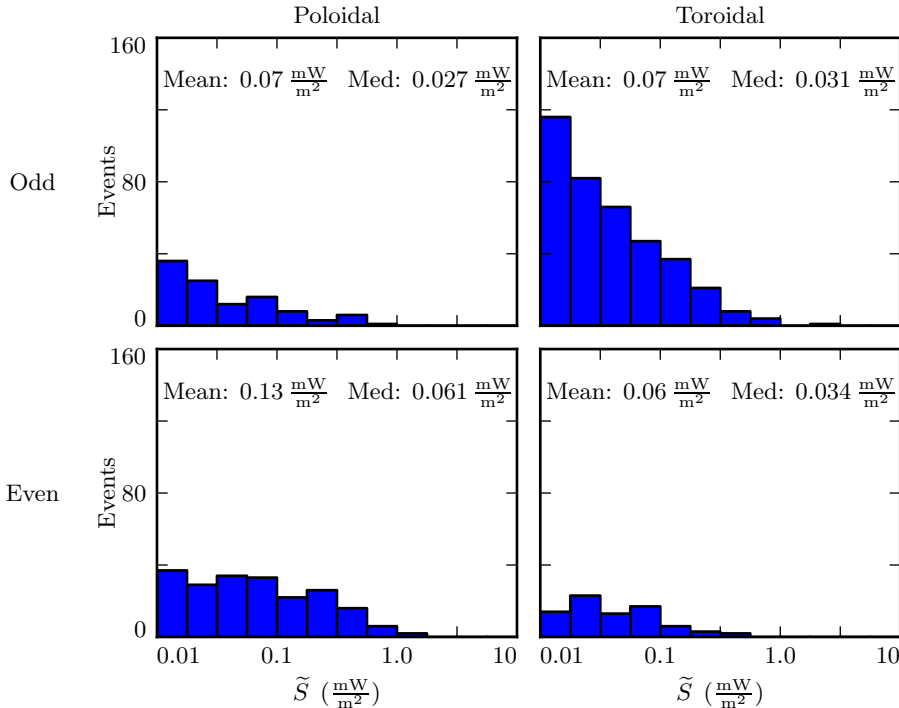


Figure 8.4: Amplitude distribution is shown for Pc4 events by parity and polarization, based on the peak of the spectrum's Gaussian fit. Odd poloidal events, odd toroidal events, and even toroidal events fall off sharply with increasing amplitude, while the even poloidal events are distributed more broadly — the mean and median of the even poloidal distribution is twice as large as that of the others.

1388 The distribution of event magnitudes is presented in Figure 8.4, graded based on the
 1389 peak of the Gaussian fit of each event's Poynting flux, $|\tilde{S}(\omega)|$. Mean and median
 1390 values are listed for each mode. Most events are small, with Poynting flux well below
 1391 0.1 mW/m^2 when mapped to the ionosphere. Only a handful of events — 3 out of 762
 1392 — exceed 1 mW/m^2 , typically taken to be the threshold at which visible auroral arcs
 1393 form. One such event is shown in Figure 8.5.

1394 TODO: Say something about this event? Not really clear what purpose is served by this
1395 example, actually. As a matter of curiosity, the apparent wave activity in the toroidal
1396 channel did not pass the event selection trigger because the electric and magnetic wave-
1397 forms are not coherent.

1398 Perhaps the most notable feature of Figure 8.4 is the relative uniformity of the distri-
1399 bution of even poloidal events. If a higher magnitude threshold is imposed, as shown in
1400 Figure 8.6, the proportion of even poloidal events rises.

1401 The spatial bins in Figure 8.6 are larger than those in Section 8.2; this change reflects
1402 an effort to keep the number of events large compared to the number of bins, even when
1403 considering relatively small subsets of the data. The larger bins — two hours wide in
1404 MLT and divided at $L = 5$ radially — are also used in Sections 8.4 and 8.5. All of the
1405 large-binned bullseye plots also share a common logarithmic color bar.

1406 All else being equal, one might expect the amplitude distribution of even toroidal modes
1407 to mimic that of even poloidal modes, since poloidal waves asymptotically rotate to
1408 toroidal waves. However, this does not seem to be the case. The mean and median
1409 magnitudes are more or less consistent for even toroidal modes, odd toroidal modes,
1410 and odd poloidal modes, while even poloidal modes are twice as large by those metrics.
1411 This would seem to imply that large even poloidal modes have disproportionately high
1412 modenumbers, and thus deliver energy to the toroidal mode less efficiently. This expla-
1413 nation is also unsatisfying, however; Figure 8.6 shows that even poloidal and toroidal
1414 modes both become more concentrated near noon at high amplitude, suggesting a com-
1415 mon origin.

Waveforms and Spectra: Odd Poloidal Wave

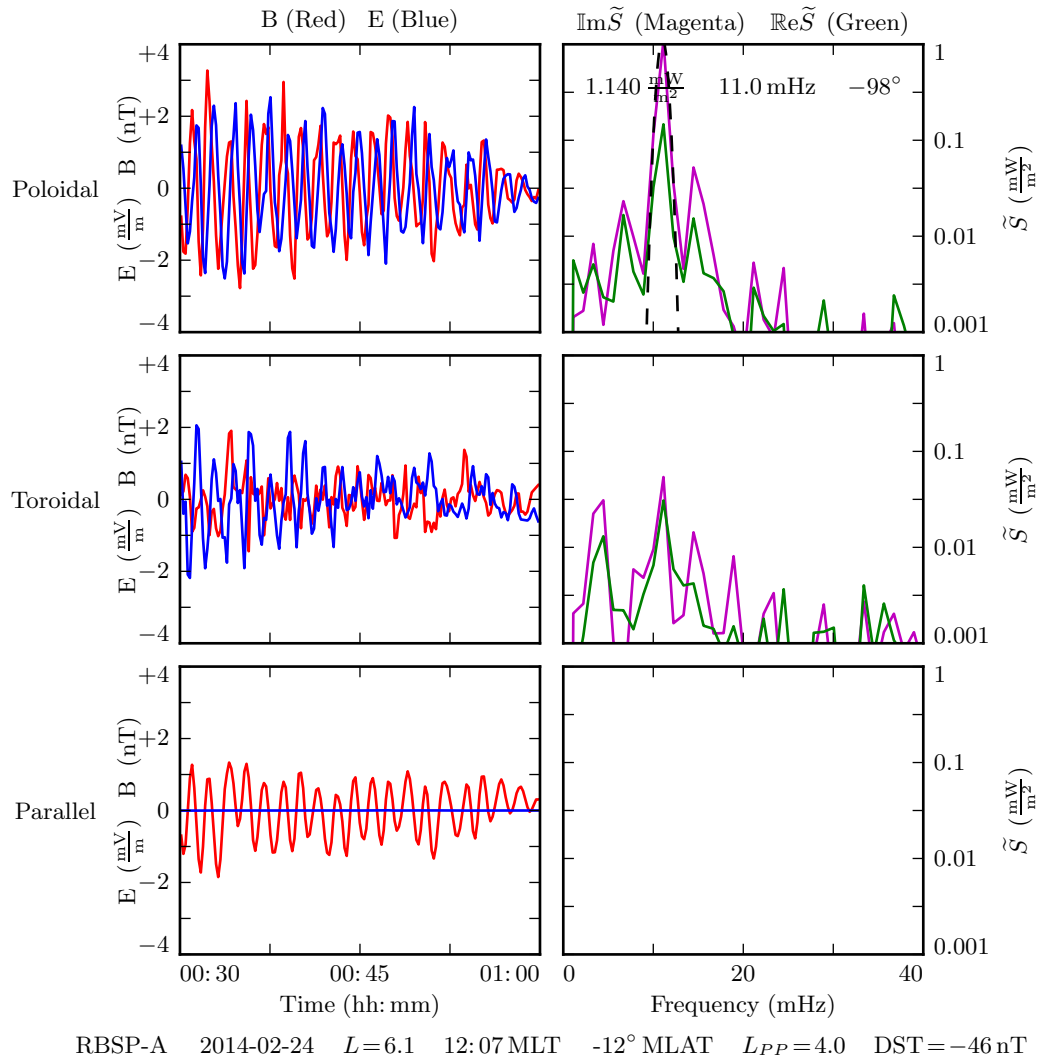


Figure 8.5: **TODO:** ...

Distribution of Pc4 Events by Mode and Amplitude

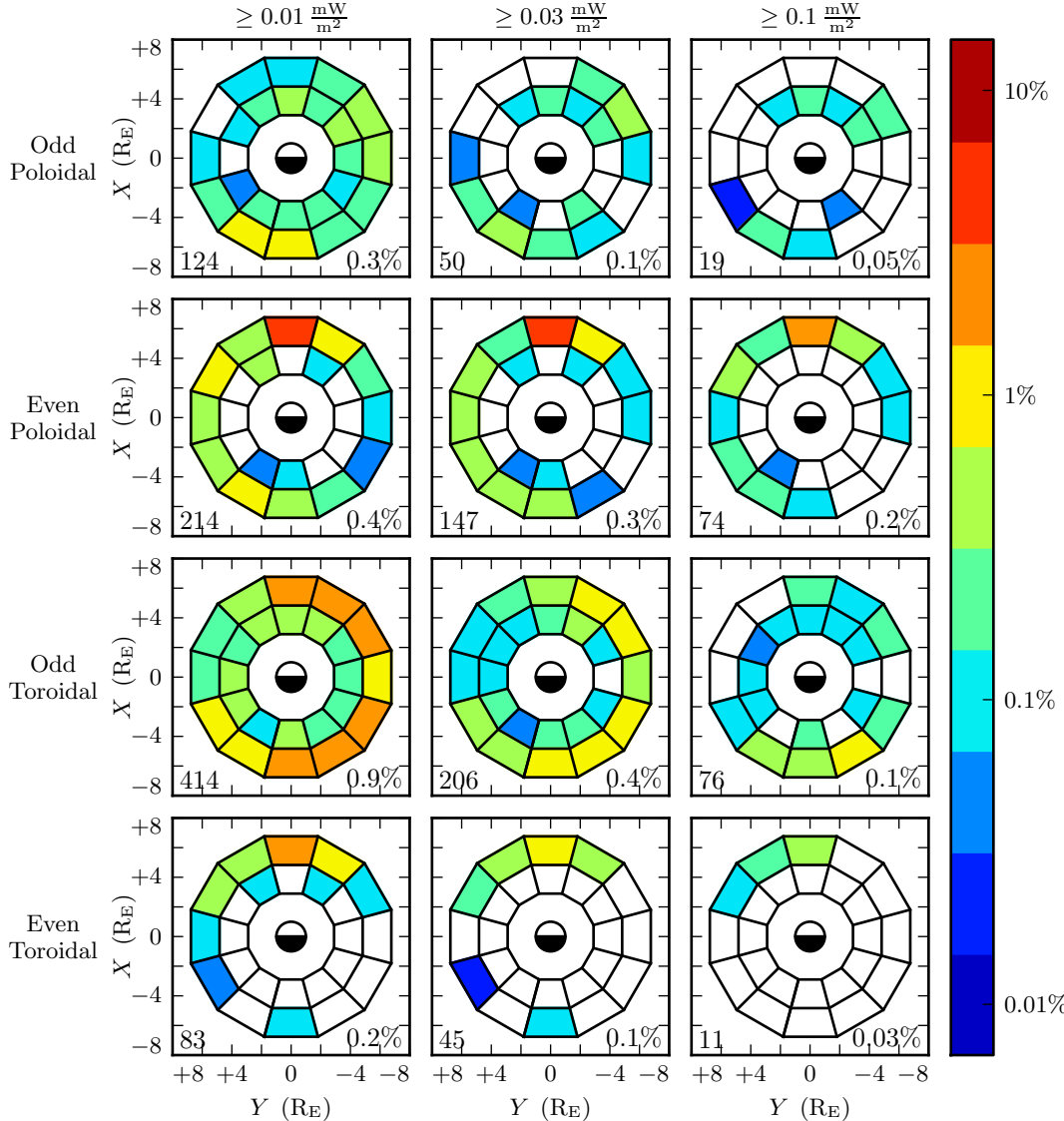


Figure 8.6: The above figure shows the distribution of Pc4 event observations by mode. Event magnitude cutoff is constant down each column, and increases from left to right. Stronger even events appear to become more concentrated on the dayside as the amplitude increases. Even poloidal events also become significantly more numerous relative to the other three modes, from 26 % at a cutoff of 0.01 mW/m^2 to 41 % at 0.1 mW/m^2 .

¹⁴¹⁶ 8.4 Events by Frequency

¹⁴¹⁷ The difference in magnetospheric conditions between the dayside and the nightside
¹⁴¹⁸ suggest that different eigenfrequencies should arise between dayside and nightside res-
¹⁴¹⁹ onances at the same L -shell. In fact, this phenomenon has been observed directly;
¹⁴²⁰ the frequencies of azimuthally-drifting FLRs have been shown to change over time[70].
¹⁴²¹ The effect is attributed to the difference in mass loading (and thus Alfvén speed) as a
¹⁴²² function of MLT.

¹⁴²³ This effect was furthermore apparent in the numerical results shown in Chapter 7, where
¹⁴²⁴ Alfvén speeds on the dayside (based on empirical profiles) gave rise to significantly higher
¹⁴²⁵ eigenfrequencies than those on the nightside.

¹⁴²⁶ In Figure 8.7, events at 11 mHz to 17 mHz (center column) do seem to be shifted night-
¹⁴²⁷ ward compared to those at 7 mHz to 11 mHz (left column), but the effect is far more
¹⁴²⁸ pronounced than what is suggested by Sections 7.2 and 7.3.

¹⁴²⁹ **TODO:** We should show the runs driven at $L \sim 5$ across the board. Dayside and
¹⁴³⁰ nightside. That way we can make a fair comparison.

¹⁴³¹ As might be expected, even events are more prevalent than first-harmonic-dominated
¹⁴³² odd events higher in the Pc4 range. Events at 7 mHz to 11 mHz (left column) outnumber
¹⁴³³ those at 17 mHz to 25 mHz (right column) ten-to-one or more for odd events. Among
¹⁴³⁴ even events, the comparison is closer to three-to-one.

¹⁴³⁵ The spatial distribution of odd toroidal events above 17 mHz warrants specific consid-
¹⁴³⁶ eration. Whereas odd toroidal events overall show an overwhelming preference for the
¹⁴³⁷ morning side, those at the top of the Pc4 frequency band instead appear from noon
¹⁴³⁸ to dusk. It's possible that this distribution is a consequence of the small number of
¹⁴³⁹ events (25). More likely, however, is that these are third-harmonic events, and that
¹⁴⁴⁰ their source more closely resembles the source for second-harmonic waves than it does
¹⁴⁴¹ first-harmonics.

¹⁴⁴² **TODO:** Have people looked at third harmonics?

1443 The frequency distribution for each mode is shown in Figure 8.8. The most distinctive
1444 feature, certainly, is the frequency peak in the odd toroidal mode near 9 mHz. This is
1445 in line with the idea that toroidal waves exhibit frequencies that depend sharply on L ,
1446 as discussed in Chapter 7. While the Van Allen Probes' orbits do cover a large range of
1447 L -shells, their observations (and thus the selected events) are concentrated near apogee
1448 at $L \sim 6$.

1449 TODO: Maybe put the Gaussian fit back on top of these distributions? The distributions
1450 are not particularly Gaussian, but it gives a quantitative estimate of the spread.

Distribution of Pc4 Events by Mode and Frequency

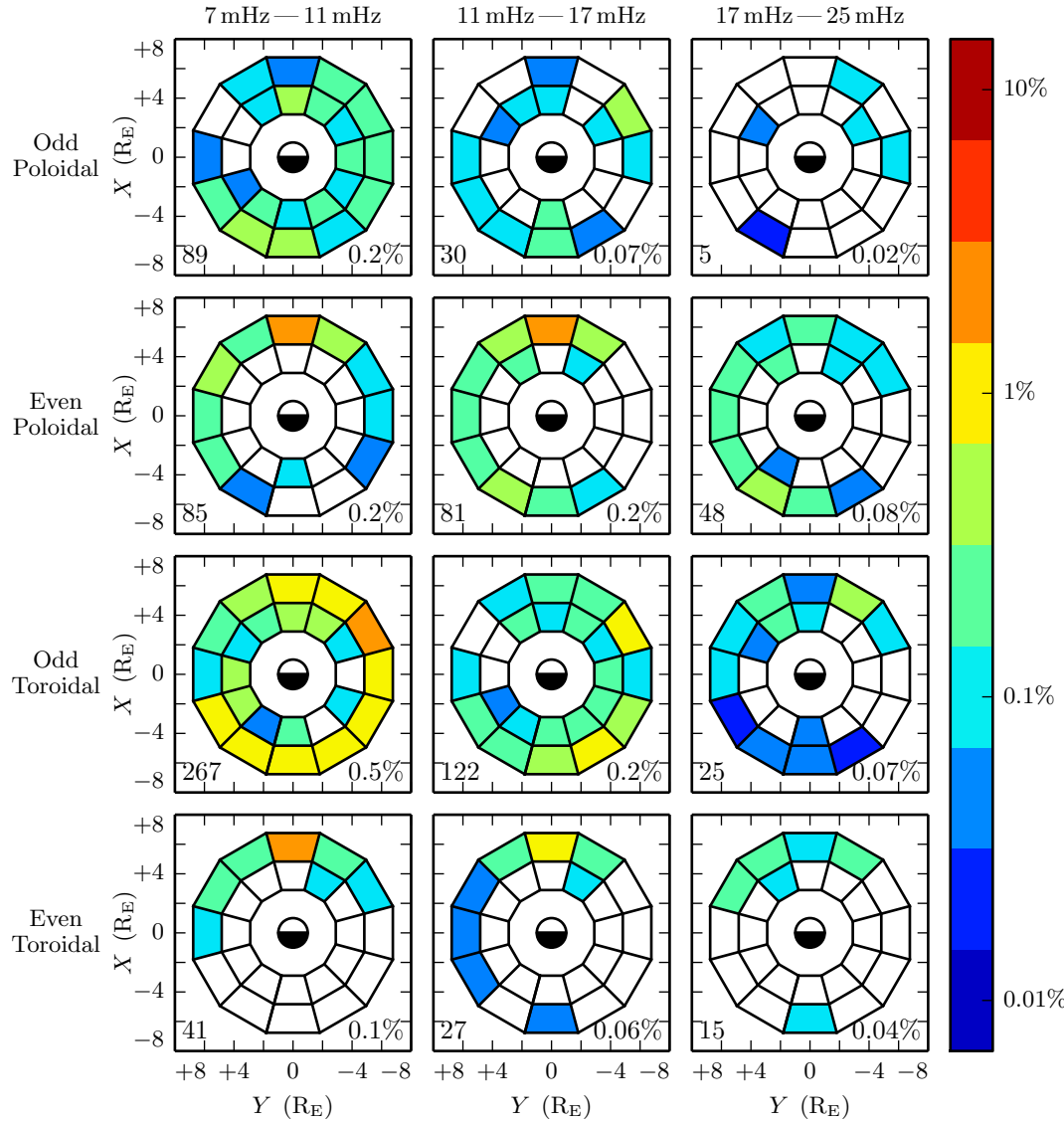


Figure 8.7: Event distributions above are shown in terms of mode (row) as well as event frequency (column). Mid-frequency Pc4 events are shifted somewhat nightward compared to low-frequency Pc4 events, as might be expected from the dayside's faster Alfvén speed. At the top of the Pc4 band, the distribution of odd toroidal events takes on a decidedly different character; this is likely because they are third harmonics rather than first harmonics.

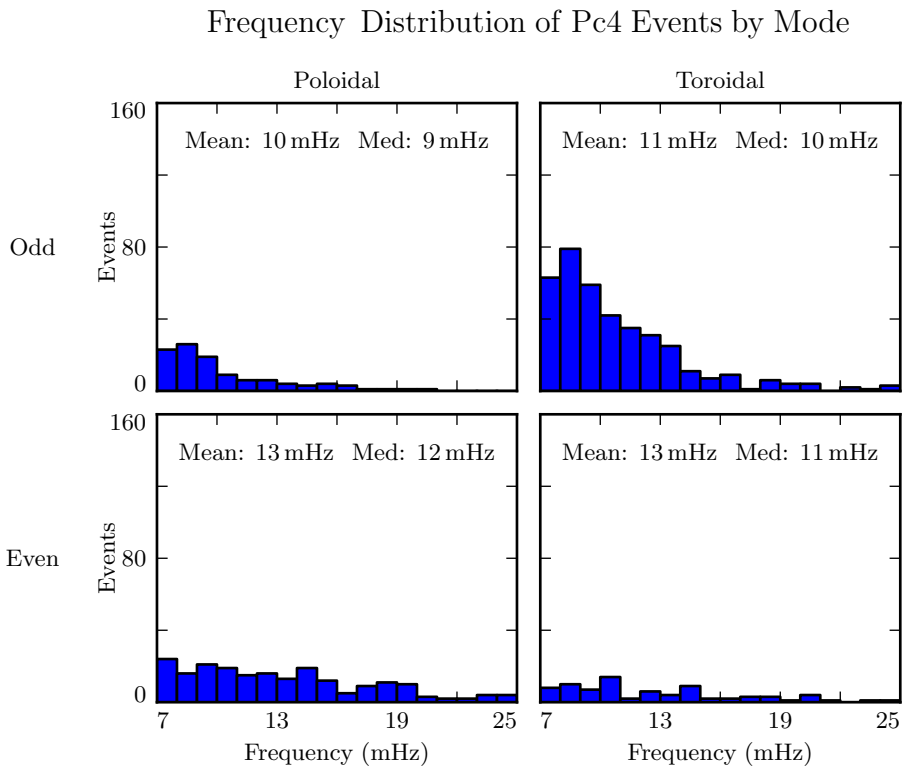


Figure 8.8: Frequency distributions are shown for all events, divided by harmonic and polarization. Odd toroidal events exhibit a particularly sharp peak in frequency, which is consistent with the toroidal mode's strong correlation with the local eigenfrequency. Poloidal modes appear more spread out in frequency, which is also consistent with past observations and with the numerical results in Chapter 7.

1451 8.5 Events by Phase

1452 The phase of a wave — that is, the phase offset between a wave's electric and magnetic
1453 fields — indicates how its energy is partitioned between the standing and traveling
1454 wave modes. An ideal standing wave has a phase of $\pm 90^\circ$, and thus its Poynting flux is
1455 completely imaginary. A traveling wave, on the other hand, has electric and magnetic
1456 fields in phase (or in antiphase), and is associated with a net movement of energy,
1457 usually toward the ionosphere.

1458 Wave phase is a topic of significant interest, since it allows an estimate to be made of
1459 the wave's lifetime. And, because phase can only be determined using simultaneous
1460 electric and magnetic field measurements, it has only recently become observable.

1461 **TODO: Do people really care about phase, or is it just John?**

The energy per unit volume, and the rate at which energy is carried out of that volume by Poynting flux, are respectively given by:

$$U = \frac{R^3}{2\mu_0} B^2 \quad \frac{\partial}{\partial t} U = \frac{R^2}{\mu_0} EB \cos \varphi \quad (8.2)$$

1462 Where B , E , and R are the characteristic magnetic field magnitude, electric field mag-
1463 nitude, and length scale. The phase, $\varphi \equiv \arctan \frac{\text{Im}S}{\text{Re}S}$, enters because only real Poynting
1464 flux carries energy.

The ratio of the two quantities in Equation (8.2) gives a characteristic timescale over which energy leaves the system

$$\tau \equiv \frac{BR}{2E \cos \varphi} \quad (8.3)$$

1465 In the present case, magnetic fields are on the order of 1 nT and electric fields are on
1466 the order of 1 mV/m. A reasonable scale length might be 10^4 km, the distance traversed
1467 by the probe over the course of a half-hour event (notably, back-to-back events are
1468 unusual).

1469 At a phase of 80° , this timescale is comparable to a $Pc4$ wave period. At 135° , where
1470 energy is divided evenly between the standing and traveling wave, the timescale is only
1471 7 seconds. A wave with a phase so far from 90° would quickly vanish unless it were
1472 constantly being replenished.

1473 An example of just such an event is shown in Figure 8.9. The left column shows
1474 electric and magnetic field waveforms in blue and red respectively. The right shows
1475 the corresponding spectra: imaginary Poynting flux in magenta (corresponding to the
1476 strength of the standing wave) and real Poynting flux in green (for the traveling wave).
1477 The black line is a Gaussian fit to the magnitude of the Poynting flux.

1478 The poloidal channel shows a mostly-standing wave, with a phase of 79° . The coherent
1479 activity in the compressional magnetic field implies a low azimuthal modenumber, and
1480 thus a fast rotation of energy from the poloidal mode to the toroidal mode. It's likely
1481 the rotation of energy from the poloidal mode contributes significantly to the toroidal
1482 mode's lifetime; the toroidal wave's phase is 130° , so its energy should be carried away
1483 quickly by Poynting flux.

1484 The selection process described in Section 8.1 does not explicitly consider phase. How-
1485 ever, the discrete Fourier transform is performed over a half-hour time span. An event
1486 with a comparatively short lifetime would be unlikely to register. It's unsurprising to
1487 see the events in Figure 8.10 tightly clustered near 90° .

1488 It's further notable in Figure 8.10 that the odd events are more spread out in phase
1489 than the even events. Near the equator, odd modes have an electric field antinode and
1490 a magnetic field node; per Equation (8.3), an odd mode's lifetime should be longer than
1491 that of an even mode with the same phase. Figure 8.10 uses the absolute value of each
1492 event's phase, as does Figure 8.11.

1493 Unlike amplitude (Section 8.3) and frequency (Section 8.4), events of different phase do
1494 not seem to exhibit different spatial distributions, as shown in Figure 8.11. Comparisons
1495 are limited by the small event counts in several of the subplots; however, coarsely
1496 speaking, events with phases of 75° and worse (left column) show spatial distributions
1497 more or less in proportion with events phased 85° or better (right column).

Waveforms and Spectra: Odd Poloidal Wave and Odd Toroidal Wave

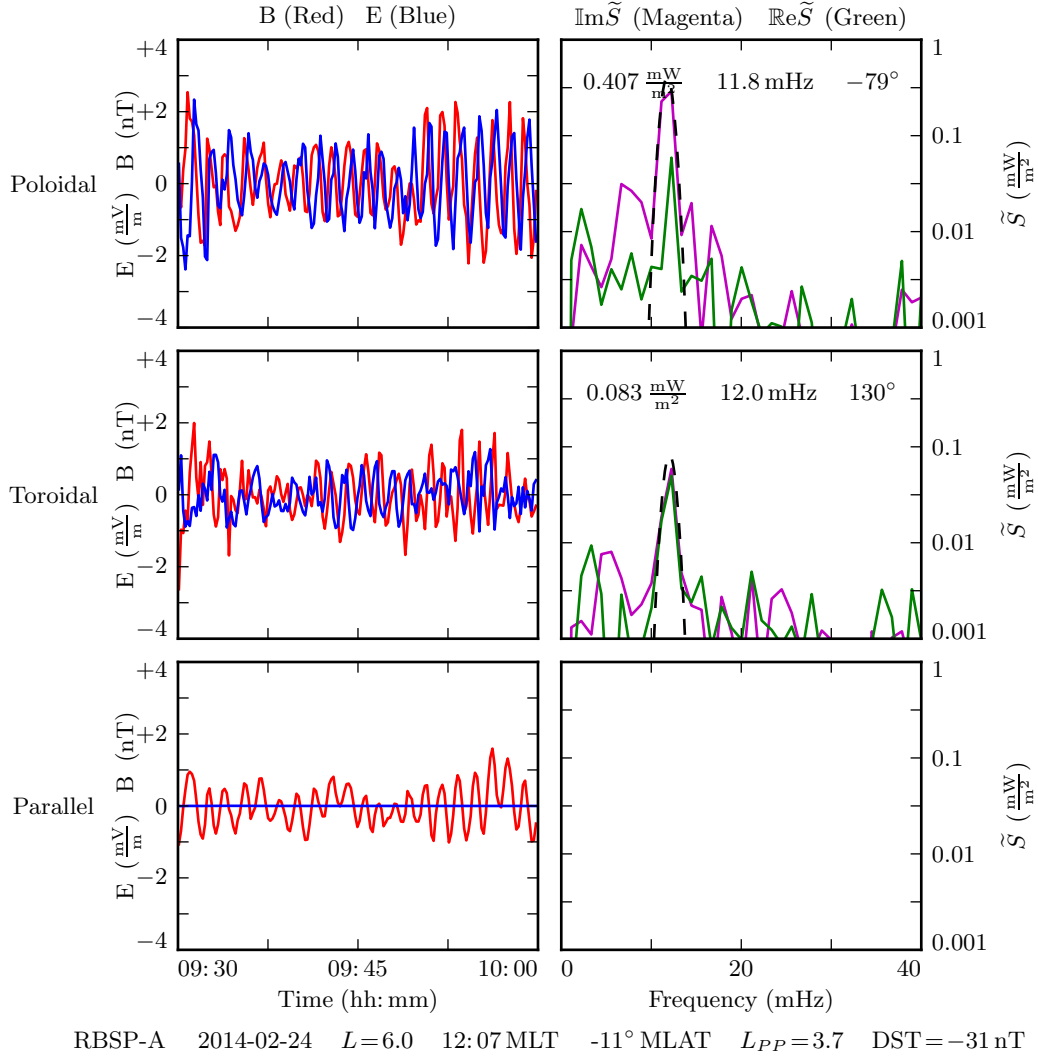


Figure 8.9: The above is a double event, where the poloidal and toroidal channels have been independently selected as events. The poloidal channel shows a wave with most of its energy in the standing wave (phase of 79°). The toroidal mode has a significant traveling component (phase of 130°). The compressional activity implies a low modenumber, which would cause energy to rotate quickly from the poloidal mode to the toroidal mode — evidently at a sufficient rate to replenish the losses due to the traveling mode's real Poynting flux.

Phase Distribution of Pc4 Events by Mode

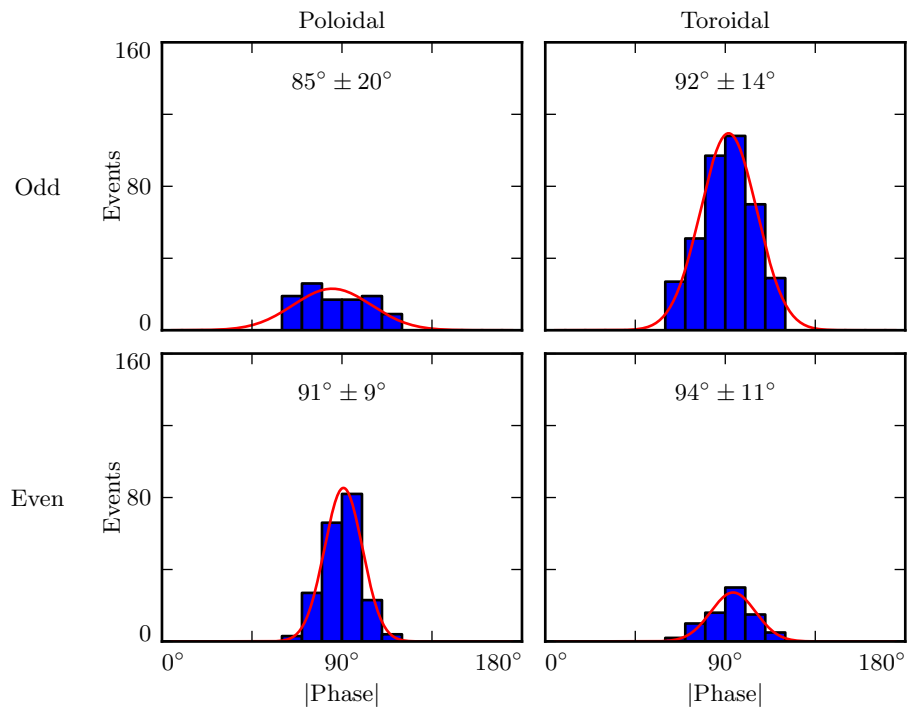


Figure 8.10: **TODO:** ...

Distribution of Pc4 Events by Mode and Phase

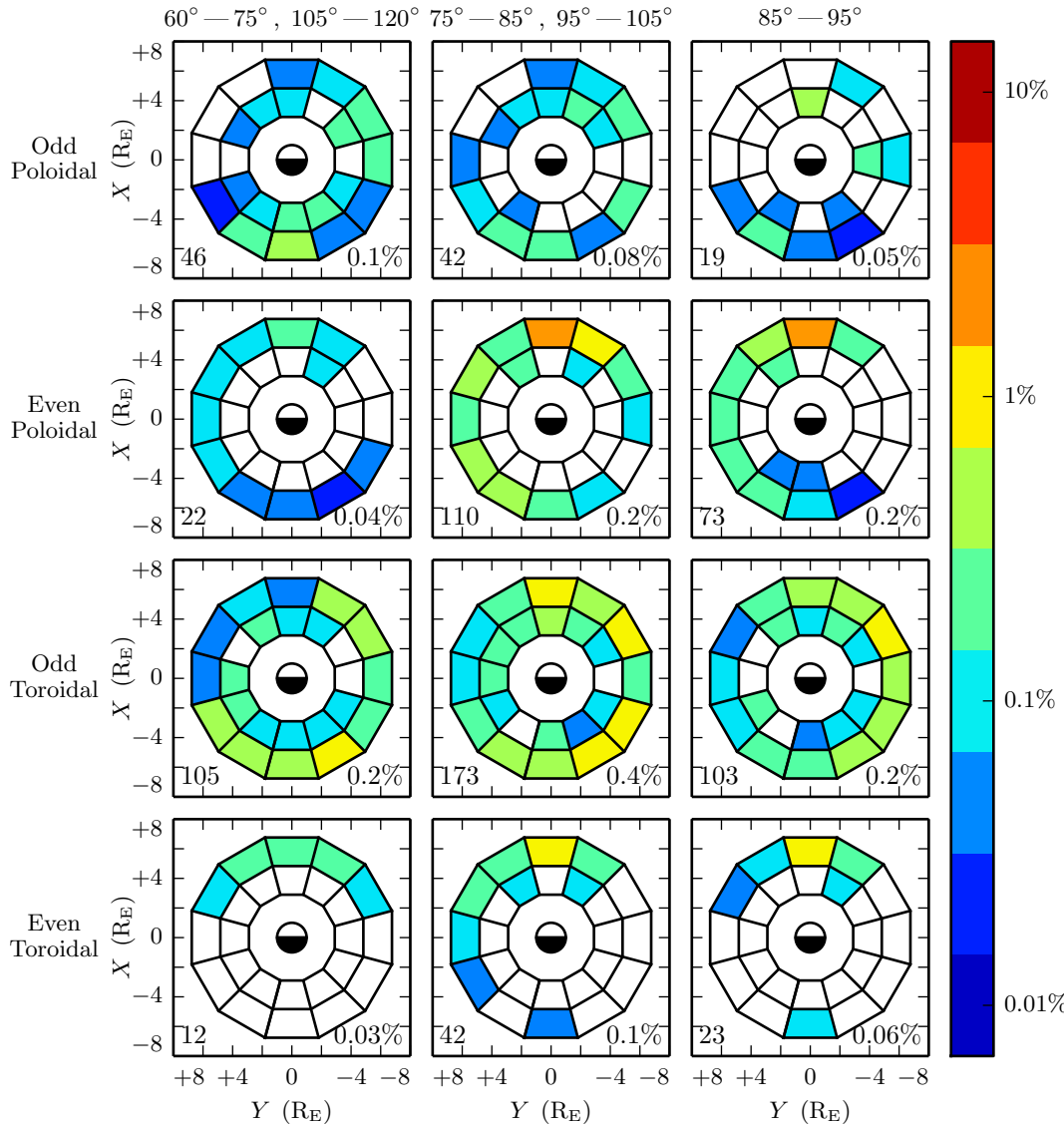


Figure 8.11: The observation rate of events is shown above, divided by (absolute) phase as well as mode. The closer a phase to 90° , the more of an event's energy is in the standing wave, rather than the traveling wave. The spatial distribution of events is more or less consistent between waves with phases very close to 90° and those with a significant traveling wave component.

1498 **8.6 Discussion**

1499 **TODO:** ...

1500 **Chapter 9**

1501 **Conclusion**

1502 **9.1 Summary of Results**

1503 TODO: Code development... Chapters 5 and 6

1504 TODO: Make the Git repository public, and link to it.

1505 TODO: Numerical results... Chapter 7

1506 TODO: Re-summarize the Discussion sections, I guess.

1507 TODO: Observational results... Chapter 8

1508 TODO: Link to the Git repository.

1509 **9.2 Future Work**

1510 TODO: Code development.

1511 Arbitrary deformation of grid. Get $\hat{e}_i = \frac{\partial}{\partial u^i} \underline{x}$, then $g_{ij} = \hat{e}_i \cdot \hat{e}_j$, then invert the metric
1512 tensor for contravariant components.

1513 MPI. Time to compute vs time to broadcast. This might make sense for inertial length
1514 scales.

- 1515 Better ionospheric profiles. Distinction between the dawn and dusk flanks. Maybe even
1516 update the conductivity based on energy deposition — precipitation causes ionization!
- 1517 IRI ionosphere model. Solar illumination effects.
- 1518 **TODO: Numerical work.**
- 1519 More complicated driving. Higher harmonics, non-sinusoidal waveforms. Maybe even
1520 drive based on events?
- 1521 Look at the phase of waves in Tuna. How much is standing/traveling?
- 1522 **TODO: Analysis of RBSP data.**
- 1523 Basically just do everything over again, twice as well, once the probes have finished
1524 sampling the dayside again.

1525

References

- 1526 [1] S.-I. Akasofu. The development of the auroral substorm. *Planetary and Space*
1527 *Science*, 12(4):273–282, 1964.
- 1528 [2] H. Alfvén. On the cosmogony of the solar system III. *Stockholms Observatoriums*
1529 *Annaler*, 14:9.1–9.29, 1946.
- 1530 [3] B. J. Anderson, M. J. Engebretson, S. P. Rounds, L. J. Zanetti, and T. A. Potemra.
1531 A statistical study of Pc 3-5 pulsations observed by the AMPTE/CCE magnetic
1532 fields experiment, 1. occurrence distributions. *J. Geophys. Res.*, 95(A7):10495,
1533 1990.
- 1534 [4] V. Angelopoulos. The THEMIS mission. *Space Science Reviews*, 141(1-4):5–34,
1535 2008.
- 1536 [5] C. W. Arthur and R. L. McPherron. The statistical character of Pc 4 magnetic
1537 pulsations at synchronous orbit. *J. Geophys. Res.*, 86(A3):1325, 1981.
- 1538 [6] K. Birkeland. Expédition norvégienne de 1899-1900 pour l'étude des aurores
1539 boréales. *Mat. Naturvidensk. Kl.*, KI(I), 1901.
- 1540 [7] J. P. Boris. A physically motivated solution of the Alfvén problem. *NRL Memo-*
1541 *randum Report*, 2167, 1970.
- 1542 [8] A. Brekke, T. Feder, and S. Berger. Pc4 giant pulsations recorded in Tromsø,
1543 1929-1985. *Journal of Atmospheric and Terrestrial Physics*, 49(10):1027–1032,
1544 1987.

- 1545 [9] C. W. Carlson, R. F. Pfaff, and J. G. Watzin. The fast auroral Snapshot (FAST)
1546 mission. *Geophys. Res. Lett.*, 25(12):2013–2016, 1998.
- 1547 [10] A. A. Chan, M. Xia, and L. Chen. Anisotropic alfvén-balloon modes in Earth’s
1548 magnetosphere. *J. Geophys. Res. Space Physics*, 99(A9):17351–17366, 1994.
- 1549 [11] L. Chen and A. Hasegawa. A theory of long-period magnetic pulsations: 1. steady
1550 state excitation of field line resonance. *J. Geophys. Res.*, 79(7):1024–1032, 1974.
- 1551 [12] L. Chen and A. Hasegawa. Kinetic theory of geomagnetic pulsations: 1. internal
1552 excitations by energetic particles. *J. Geophys. Res.*, 96(A2):1503, 1991.
- 1553 [13] L. Chen, R. White, C. Cheng, F. Romanelli, J. Weiland, R. Hay, J. V. Dam,
1554 D. Barnes, M. Rosenbluth, and S. Tsai. Theory and simulation of fishbone-type
1555 instabilities in beam-heated tokamaks. Technical report, 1984.
- 1556 [14] C. Z. Cheng and Q. Qian. Theory of ballooning-mirror instabilities for anisotropic
1557 pressure plasmas in the magnetosphere. *J. Geophys. Res.*, 99(A6):11193, 1994.
- 1558 [15] G. Chisham and D. Orr. Statistical studies of giant pulsations (pgs): Harmonic
1559 mode. *Planetary and Space Science*, 39(7):999–1006, 1991.
- 1560 [16] W. D. Cummings, R. J. O’Sullivan, and P. J. Coleman. Standing Alfvén waves in
1561 the magnetosphere. *J. Geophys. Res.*, 74(3):778–793, 1969.
- 1562 [17] L. Dai. Collisionless magnetic reconnection via Alfvén eigenmodes. *Phys. Rev.*
1563 *Lett.*, 102(24), 2009.
- 1564 [18] L. Dai, K. Takahashi, R. Lysak, C. Wang, J. R. Wygant, C. Kletzing, J. Bonnell,
1565 C. A. Cattell, C. W. Smith, R. J. MacDowall, S. Thaller, A. Breneman, X. Tang,
1566 X. Tao, and L. Chen. Storm time occurrence and spatial distribution of Pc4
1567 poloidal ULF waves in the inner magnetosphere: A Van Allen Probes statistical
1568 study. *J. Geophys. Res. Space Physics*, 120:4748–4762, 2015.
- 1569 [19] L. Dai, K. Takahashi, J. R. Wygant, L. Chen, J. Bonnell, C. A. Cattell, S. Thaller,
1570 C. Kletzing, C. W. Smith, R. J. MacDowall, D. N. Baker, J. B. Blake, J. Fennell,
1571 S. Claudepierre, H. O. Funsten, G. D. Reeves, and H. E. Spence. Excitation of

- 1572 poloidal standing Alfvén waves through drift resonance wave-particle interaction.
1573 *Geophys. Res. Lett.*, 40:4127–4132, 2013.
- 1574 [20] A. W. Degeling, R. Rankin, and Q.-G. Zong. Modeling radiation belt electron
1575 acceleration by ULF fast mode waves, launched by solar wind dynamic pressure
1576 fluctuations. *J. Geophys. Res. Space Physics*, 119(11):8916–8928, 2014.
- 1577 [21] W. D. D’haeseleer, W. N. G. H. J. D. Callen, and J. L. Shohet. *Flux Coordinates*
1578 and *Magnetic Field Structure*. Springer-Verlag, New York, 1991.
- 1579 [22] J. W. Dungey. The attenuation of Alfvén waves. *J. Geophys. Res.*, 59(3):323–328,
1580 1954.
- 1581 [23] J. W. Dungey. Interplanetary magnetic field and the auroral zones. *Phys. Rev.*
1582 Lett., 6(2):47–48, 1961.
- 1583 [24] A. Einstein. Die grundlage der allgemeinen relativitätstheorie. *Ann. Phys.*,
1584 354:769–822, 1916.
- 1585 [25] S. R. Elkington, M. K. Hudson, and A. A. Chan. Acceleration of relativistic
1586 electrons via drift-resonant interaction with toroidal-mode Pc-5 ULF oscillations.
1587 *Geophys. Res. Lett.*, 26(21):3273–3276, 1999.
- 1588 [26] M. J. Engebretson, D. L. Murr, K. N. Erickson, R. J. Strangeway, D. M. Klumpar,
1589 S. A. Fuselier, L. J. Zanetti, and T. A. Potemra. The spatial extent of radial
1590 magnetic pulsation events observed in the dayside near synchronous orbit. *J.*
1591 *Geophys. Res.*, 97(A9):13741, 1992.
- 1592 [27] M. J. Engebretson, L. J. Zanetti, T. A. Potemra, D. M. Klumpar, R. J. Strange-
1593 way, and M. H. Acuña. Observations of intense ULF pulsation activity near the
1594 geomagnetic equator during quiet times. *J. Geophys. Res.*, 93(A11):12795, 1988.
- 1595 [28] S. Fujita and T. Tamao. Duct propagation of hydromagnetic waves in the upper
1596 ionosphere, 1, electromagnetic field disturbances in high latitudes associated with
1597 localized incidence of a shear Alfvén wave. *J. Geophys. Res.*, 93(A12):14665, 1988.
- 1598 [29] K.-H. Glassmeier. Magnetometer array observations of a giant pulsation event. *J.*
1599 *Geophys.*, 48:127–138, 1980.

- 1600 [30] K.-H. Glassmeier. On the influence of ionospheres with non-uniform conductivity
1601 distribution on hydromagnetic waves. *J. Geophys.*, 54(2):125–137, 1984.
- 1602 [31] K.-H. Glassmeier, S. Buchert, U. Motschmann, A. Korth, and A. Pedersen. Con-
1603 cerning the generation of geomagnetic giant pulsations by drift-bounce resonance
1604 ring current instabilities. *Ann. Geophysicae*, 17:338–350, 1999.
- 1605 [32] C. Goertz. Kinetic alfvén waves on auroral field lines. *Planetary and Space Science*,
1606 32(11):1387–1392, 1984.
- 1607 [33] C. K. Goertz and R. W. Boswell. Magnetosphere-ionosphere coupling. *J. Geophys.*
1608 *Res.*, 84(A12):7239, 1979.
- 1609 [34] C. A. Green. Giant pulsations in the plasmasphere. *Planetary and Space Science*,
1610 33(10):1155–1168, 1985.
- 1611 [35] J. L. Green and S. Boardsen. Duration and extent of the great auroral storm of
1612 1859. *Advances in Space Research*, 38(2):130–135, 2006.
- 1613 [36] C. Greifinger and P. S. Greifinger. Theory of hydromagnetic propagation in the
1614 ionospheric waveguide. *J. Geophys. Res.*, 73(23):7473–7490, 1968.
- 1615 [37] B. C. Hall. *Lie Groups, Lie Algebras, and Representations*. Graduate Texts in
1616 Mathematics. Springer, New York, second edition, 2015.
- 1617 [38] Y. X. Hao, Q.-G. Zong, Y. F. Wang, X.-Z. Zhou, H. Zhang, S. Y. Fu, Z. Y.
1618 Pu, H. E. Spence, J. B. Blake, J. Bonnell, J. R. Wygant, and C. A. Kletzing.
1619 Interactions of energetic electrons with ULF waves triggered by interplanetary
1620 shock: Van allen probes observations in the magnetotail. *J. Geophys. Res. Space*
1621 *Physics*, 119(10):8262–8273, 2014.
- 1622 [39] L. Harang. *Pulsations in the terrestrial magnetic records at high latitude stations*.
1623 Grondahl, 1942.
- 1624 [40] O. Hillebrand, J. Muench, and R. L. McPherron. Ground-satellite correlative
1625 study of a giant pulsation event. *Journal of Geophysics Zeitschrift Geophysik*,
1626 51:129–140, 1982.

- 1627 [41] W. J. Hughes. The effect of the atmosphere and ionosphere on long period mag-
1628 netospheric micropulsations. *Planet. Space Sci.*, 22:1157–1172, 1974.
- 1629 [42] W. J. Hughes. Magnetospheric ULF waves: A tutorial with a historical perspec-
1630 tive. In M. J. Engebretson, K. Takahashi, and M. Scholer, editors, *Solar Wind*
1631 *Sources of Magnetospheric Ultra-Low-Frequency Waves*, volume 81 of *Geophys.*
1632 *Monogr.*, pages 1–12. American Geophysical Union, Washington, DC, 1994.
- 1633 [43] W. J. Hughes and D. J. Southwood. The screening of micropulsation signals by
1634 the atmosphere and ionosphere. *J. Geophys. Res.*, 81(19):3234–3240, 1976.
- 1635 [44] W. J. Hughes, D. J. Southwood, B. Mauk, R. L. McPherron, and J. N. Barfield.
1636 Alfvén waves generated by an inverted plasma energy distribution. *Nature*,
1637 275(5675):43–45, 1978.
- 1638 [45] J. A. Jacobs, Y. Kato, S. Matsushita, and V. A. Troitskaya. Classification of
1639 geomagnetic micropulsations. *J. Geophys. Res.*, 69(1):180–181, 1964.
- 1640 [46] T. Karlsson and G. T. Marklund. A statistical study of intense low-altitude electric
1641 fields observed by freja. *Geophys. Res. Lett.*, 23(9):1005–1008, 1996.
- 1642 [47] Y. Kato and T. Tsutomu. Hydromagnetic oscillations in a conducting medium
1643 with hall couduct-ivity under the uniform magnetic field. *Science reports of the*
1644 *Tohoku University. Ser. 5, Geophysics*, 7(3):147–164, 1956.
- 1645 [48] M. C. Kelley. *The Earth’s Ionosphere*. Academic Press, San Diego, second edition,
1646 1989.
- 1647 [49] R. L. Kessel. Solar wind excitation of pc5 fluctuations in the magnetosphere and
1648 on the ground. *J. Geophys. Res.*, 113(A4), 2008.
- 1649 [50] D. Y. Klimushkin, P. N. Mager, and K.-H. Glassmeier. Toroidal and poloidal
1650 Alfvén waves with arbitrary azimuthal wavenumbers in a finite pressure plasma
1651 in the earth’s magnetosphere. *Annales Geophysicae*, 22(1):267–287, 2004.
- 1652 [51] S. Kokubun. Observations of Pc pulsations in the magnetosphere: Satellite-ground
1653 correlation. *J. Geomagn. Geoelec*, 32(Supplement2):SII17–SII39, 1980.

- 1654 [52] S. Kokubun, K. N. Erickson, T. A. Fritz, and R. L. McPherron. Local time asym-
1655 metry of Pc 4-5 pulsations and associated particle modulations at synchronous
1656 orbit. *J. Geophys. Res.*, 94(A6):6607–6625, 1989.
- 1657 [53] D.-H. Lee and K. Kim. Compressional MHD waves in the magnetosphere: A new
1658 approach. *J. Geophys. Res.*, 104(A6):12379–12385, 1999.
- 1659 [54] A. S. Leonovich and V. A. Mazur. Structure of magnetosonic eigenoscillations of
1660 an axisymmetric magnetosphere. *J. Geophys. Res.*, 105(A12):27707–27715, 2000.
- 1661 [55] W. Liu, J. B. Cao, X. Li, T. E. Sarris, Q.-G. Zong, M. Hartinger, K. Takahashi,
1662 H. Zhang, Q. Q. Shi, and V. Angelopoulos. Poloidal ULF wave observed in the
1663 plasmasphere boundary layer. *J. Geophys. Res. Space Physics*, 118(7):4298–4307,
1664 2013.
- 1665 [56] W. Liu, T. E. Sarris, X. Li, S. R. Elkington, R. Ergun, V. Angelopoulos, J. Bonnell,
1666 and K. H. Glassmeier. Electric and magnetic field observations of Pc4 and Pc5
1667 pulsations in the inner magnetosphere: A statistical study. *J. Geophys. Res.*,
1668 114(A12), 2009.
- 1669 [57] W. Liu, T. E. Sarris, X. Li, Q.-G. Zong, R. Ergun, V. Angelopoulos, and K. H.
1670 Glassmeier. Spatial structure and temporal evolution of a dayside poloidal ULF
1671 wave event. *Geophys. Res. Lett.*, 38(19), 2011.
- 1672 [58] R. L. Lysak. Magnetosphere-ionosphere coupling by Alfvén waves at midlatitudes.
1673 *J. Geophys. Res.*, 109, 2004.
- 1674 [59] R. L. Lysak and D. hun Lee. Response of the dipole magnetosphere to pressure
1675 pulses. *Geophys. Res. Lett.*, 19(9):937–940, 1992.
- 1676 [60] R. L. Lysak and Y. Song. A three-dimensional model of the propagation of Alfvén
1677 waves through the auroral ionosphere: first results. *Adv. Space Res.*, 28:813–822,
1678 2001.
- 1679 [61] R. L. Lysak, C. L. Waters, and M. D. Sciffer. Modeling of the ionospheric Alfvén
1680 resonator in dipolar geometry. *J. Geophys. Res. Space Physics*, 118, 2013.

- 1681 [62] P. N. Mager and D. Y. Klimushkin. Giant pulsations as modes of a transverse
1682 Alfvénic resonator on the plasmapause. *Earth, Planets and Space*, 65(5):397–409,
1683 2013.
- 1684 [63] I. R. Mann, E. A. Lee, S. G. Claudepierre, J. F. Fennell, A. Degeling, I. J. Rae,
1685 D. N. Baker, G. D. Reeves, H. E. Spence, L. G. Ozeke, R. Rankin, D. K. Milling,
1686 A. Kale, R. H. W. Friedel, and F. Honary. Discovery of the action of a geophysical
1687 synchrotron in the Earth’s Van Allen radiation belts. *Nature Communications*, 4,
1688 2013.
- 1689 [64] I. R. Mann and A. N. Wright. Finite lifetimes of ideal poloidal Alfvén waves. *J.
1690 Geophys. Res.*, 100:23677–23686, 1995.
- 1691 [65] I. R. Mann, A. N. Wright, and A. W. Hood. Multiple-timescales analysis of ideal
1692 poloidal Alfvén waves. *J. Geophys. Res.*, 102(A2):2381–2390, 1997.
- 1693 [66] T. Maynard, N. Smith, S. Gonzalez, et al. Solar storm risk to the North American
1694 electric grid. 2013.
- 1695 [67] K. McGuire, R. Goldston, M. Bell, M. Bitter, K. Bol, K. Brau, D. Buchenauer,
1696 T. Crowley, S. Davis, F. Dylla, H. Eubank, H. Fishman, R. Fonck, B. Grek,
1697 R. Grimm, R. Hawryluk, H. Hsuan, R. Hulse, R. Izzo, R. Kaita, S. Kaye, H. Kugel,
1698 D. Johnson, J. Manickam, D. Manos, D. Mansfield, E. Mazzucato, R. McCann,
1699 D. McCune, D. Monticello, R. Motley, D. Mueller, K. Oasa, M. Okabayashi,
1700 K. Owens, W. Park, M. Reusch, N. Sauthoff, G. Schmidt, S. Sesnic, J. Strachan,
1701 C. Surko, R. Slusher, H. Takahashi, F. Tenney, P. Thomas, H. Towner, J. Valley,
1702 and R. White. Study of high-beta magnetohydrodynamic modes and fast-ion
1703 losses in PDX. *Phys. Rev. Lett.*, 50(12):891–895, 1983.
- 1704 [68] R. L. McPherron. The role of substorms in the generation of magnetic storms.
1705 *Washington DC American Geophysical Union Geophysical Monograph Series*,
1706 98:131–147, 1997.
- 1707 [69] R. L. McPherron, G. K. Parks, D. S. Colburn, and M. D. Montgomery. Satellite
1708 studies of magnetospheric substorms on august 15, 1968: 2. solar wind and outer
1709 magnetosphere. *J. Geophys. Res.*, 78(16):3054–3061, 1973.

- 1710 [70] T. Motoba, K. Takahashi, J. V. Rodriguez, and C. T. Russell. Giant pulsations on
1711 the afternoonside: Geostationary satellite and ground observations. *J. Geophys.*
1712 *Res. Space Physics*, 120:8350–8367, 2015.
- 1713 [71] NASA. Coordinated data analysis (workshop) web.
- 1714 [72] NASA. Near miss: The solar superstorm of july 2012.
- 1715 [73] M. Nicolet. The collision frequency of electrons in the ionosphere. *Journal of*
1716 *Atmospheric and Terrestrial Physics*, 3(4):200–211, 1953.
- 1717 [74] L. G. Ozeke and I. R. Mann. Energization of radiation belt electrons by ring
1718 current ion driven ULF waves. *J. Geophys. Res.*, 113(A2), 2008.
- 1719 [75] E. M. Poulter, W. Allan, E. Nielsen, and K.-H. Glassmeier. Stare radar observa-
1720 tions of a PG pulsation. *J. Geophys. Res.*, 88(A7):5668, 1983.
- 1721 [76] J. A. Proehl, W. Lotko, I. Kouznetsov, and S. D. Geimer. Ultralow-frequency
1722 magnetohydrodynamics in boundary-constrained geomagnetic flux coordinates.
1723 *J. Geophys. Res.*, 107(A9):1225, 2002.
- 1724 [77] H. R. Radoski. A note on oscillating field lines. *J. Geophys. Res.*, 72(1), 1967.
- 1725 [78] H. R. Radoski. A theory of latitude dependent geomagnetic micropulsations: The
1726 asymptotic fields. *J. Geophys. Res.*, 79, 1974.
- 1727 [79] R. Rankin, J. C. Samson, and V. T. Tikhonchuk. Parallel electric fields in dis-
1728 persive shear alfvén waves in the dipolar magnetosphere. *Geophys. Res. Lett.*,
1729 26(24):3601–3604, 1999.
- 1730 [80] B. Rolf. Giant micropulsations at abisko. *J. Geophys. Res.*, 36(1):9, 1931.
- 1731 [81] G. Rostoker, H.-L. Lam, and J. V. Olson. PC 4 giant pulsations in the morning
1732 sector. *J. Geophys. Res.*, 84(A9):5153, 1979.
- 1733 [82] J. C. Samson, L. L. Cogger, and Q. Pao. Observations of field line resonances,
1734 auroral arcs, and auroral vortex structures. *J. Geophys. Res.*, 101(A8):17373–
1735 17383, 1996.

- 1736 [83] H. J. Singer, W. J. Hughes, and C. T. Russell. Standing hydromagnetic waves
1737 observed by ISEE 1 and 2: Radial extent and harmonic. *J. Geophys. Res.*,
1738 87(A5):3519, 1982.
- 1739 [84] D. J. Southwood. Some features of field line resonances in the magnetosphere.
1740 *Planetary and Space Science*, 22(3):483–491, 1974.
- 1741 [85] D. J. Southwood. A general approach to low-frequency instability in the ring
1742 current plasma. *J. Geophys. Res.*, 81(19):3340–3348, 1976.
- 1743 [86] J. Stratton and N. J. Fox. Radiation belt storm probes (RBSP) mission overview.
1744 In *2012 IEEE Aerospace Conference*. Institute of Electrical & Electronics Engi-
1745 neers (IEEE), 2012.
- 1746 [87] E. Sucksdorff. Giant pulsations recorded at sodankyl during 19141938. *Terrestrial*
1747 *Magnetism and Atmospheric Electricity*, 44(2):157–170, 1939.
- 1748 [88] K. Takahashi, J. Bonnell, K.-H. Glassmeier, V. Angelopoulos, H. J. Singer, P. J.
1749 Chi, R. E. Denton, Y. Nishimura, D.-H. Lee, M. Nosé, and W. Liu. Multipoint
1750 observation of fast mode waves trapped in the dayside plasmasphere. *J. Geophys.*
1751 *Res.*, 115(A12), 2010.
- 1752 [89] K. Takahashi, K.-H. Glassmeier, V. Angelopoulos, J. Bonnell, Y. Nishimura, H. J.
1753 Singer, and C. T. Russell. Multisatellite observations of a giant pulsation event.
1754 *J. Geophys. Res.*, 116:A11223, 2011.
- 1755 [90] K. Takahashi, M. D. Hartinger, V. Angelopoulos, K.-H. Glassmeier, and H. J.
1756 Singer. Multispacecraft observations of fundamental poloidal waves without
1757 ground magnetic signatures. *J. Geophys. Res. Space Physics*, 118:4319–4334, 2013.
- 1758 [91] K. Takahashi, R. W. McEntire, A. T. Y. Lui, and T. A. Potemra. Ion flux oscilla-
1759 tions associated with a radially polarized transverse Pc 5 magnetic pulsation. *J.*
1760 *Geophys. Res.*, 95(A4):3717, 1990.
- 1761 [92] K. Takahashi and R. L. McPherron. Standing hydromagnetic oscillations in the
1762 magnetosphere. *Planetary and Space Science*, 32:1343–1359, 1984.

- 1763 [93] K. Takahashi, N. Sato, J. Warnecke, H. Lühr, H. E. Spence, and Y. Tonegawa.
1764 On the standing wave mode of giant pulsations. *J. Geophys. Res. Space Physics*,
1765 97(A7):10717–10732, 1992.
- 1766 [94] B. J. Thompson and R. L. Lysak. Electron acceleration by inertial alfvén waves.
1767 *J. Geophys. Res.*, 101(A3):5359–5369, 1996.
- 1768 [95] V. T. Tikhonchuk and R. Rankin. Electron kinetic effects in standing shear alfvén
1769 waves in the dipolar magnetosphere. *Physics of Plasmas*, 7(6):2630, 2000.
- 1770 [96] B. T. Tsurutani, W. D. Gonzalez, G. S. Lakhina, and S. Alex. The extreme
1771 magnetic storm of 12 september 1859. *Journal of Geophysical Research: Space*
1772 *Physics*, 108(A7), 2003. 1268.
- 1773 [97] A. Y. Ukhorskiy. Impact of toroidal ULF waves on the outer radiation belt elec-
1774 trons. *J. Geophys. Res.*, 110(A10), 2005.
- 1775 [98] J. Veldkamp. A giant geomagnetic pulsation. *Journal of Atmospheric and Ter-
1776 restrial Physics*, 17(4):320–324, 1960.
- 1777 [99] J. A. Wanliss and K. M. Showalter. High-resolution global storm index: Dst versus
1778 sym-h. *Journal of Geophysical Research: Space Physics*, 111(A2):n/a–n/a, 2006.
1779 A02202.
- 1780 [100] C. L. Waters, R. L. Lysak, and M. D. Sciffer. On the coupling of fast and shear
1781 Alfvén wave modes by the ionospheric Hall conductance. *Earth Planets Space*,
1782 65:385–396, 2013.
- 1783 [101] C. L. Waters and M. D. Sciffer. Field line resonant frequencies and ionospheric
1784 conductance: Results from a 2-d MHD model. *J. Geophys. Res.*, 113(A5), 2008.
- 1785 [102] D. M. Wright and T. K. Yeoman. High-latitude HF doppler observations of ULF
1786 waves: 2. waves with small spatial scale sizes. *Ann. Geophys.*, 17(7):868–876,
1787 1999.
- 1788 [103] J. R. Wygant, J. W. Bonnell, K. Goetz, R. E. Ergun, F. S. Mozer, S. D. Bale,

- 1789 M. Ludlam, P. Turin, P. R. Harvey, R. Hochmann, K. Harps, G. Dalton, J. Mc
 1790 Cauley, W. Rachelson, D. Gordon, B. Donakowski, C. Shultz, C. Smith, M. Diaz-
 1791 Aguado, J. Fischer, S. Heavner, P. Berg, D. M. Malsapina, M. K. Bolton, M. Hud-
 1792 son, R. J. Strangeway, D. N. Baker, X. Li, J. Albert, J. C. Foster, C. C. Chaston,
 1793 I. Mann, E. Donovan, C. M. Cully, C. A. Cattell, V. Krasnoselskikh, K. Kersten,
 1794 A. Brenneman, and J. B. Tao. The electric field and waves instruments on the
 1795 radiation belt storm probes mission. *Space Science Reviews*, 179(1):183–220, 2013.
- 1796 [104] J. R. Wygant, A. Keiling, C. A. Cattell, R. L. Lysak, M. Temerin, F. S. Mozer,
 1797 C. A. Kletzing, J. D. Scudder, V. Streltsov, W. Lotko, and C. T. Russell. Evidence
 1798 for kinetic alfvn waves and parallel electron energization at 46 re altitudes in the
 1799 plasma sheet boundary layer. *Journal of Geophysical Research: Space Physics*,
 1800 107(A8):SMP 24–1–SMP 24–15, 2002.
- 1801 [105] K. Yee. Numerical solution of initial boundary value problems involving maxwell's
 1802 equations in isotropic media. *IEEE Trans. Antennas Propagat.*, 14(3), 1966.
- 1803 [106] T. K. Yeoman and D. M. Wright. ULF waves with drift resonance and drift-bounce
 1804 resonance energy sources as observed in artificially-induced HF radar backscatter.
 1805 *Ann. Geophys.*, 19(2):159–170, 2001.
- 1806 [107] Q.-G. Zong, X.-Z. Zhou, X. Li, P. Song, S. Y. Fu, D. N. Baker, Z. Y. Pu, T. A.
 1807 Fritz, P. Daly, A. Balogh, and H. Réme. Ultralow frequency modulation of ener-
 1808 getic particles in the dayside magnetosphere. *Geophys. Res. Lett.*, 34(12), 2007.
- 1809 [108] Q.-G. Zong, X.-Z. Zhou, Y. F. Wang, X. Li, P. Song, D. N. Baker, T. A. Fritz,
 1810 P. W. Daly, M. Dunlop, and A. Pedersen. Energetic electron response to ULF
 1811 waves induced by interplanetary shocks in the outer radiation belt. *J. Geophys.
 1812 Res.*, 114(A10), 2009.